SOLAR PHOTOSPHERIC AND CORONAL ABUNDANCES FROM SOLAR ENERGETIC PARTICLE MEASUREMENTS

Thesis by

H. Herbert Breneman

In Partial Fulfillment of the Requirements

for the Degree of

Doctor of Philosophy

California Institute of Technology

Pasadena, California

1985

(Submitted May 24, 1985)

Acknowledgements

The Voyager mission, of which this study is a small part, is the product of many years of hard work by hundreds of people, and to them it owes its phenomenal success. The Voyager Cosmic Ray Subsystem (CRS) investigation is the result of a collaboration of research groups at Caltech, Goddard Space Flight Center, the University of Arizona, and the University of New Hampshire, and it was the work of people at all of these institutions that made available the abundance of high-quality data used in this study. Of particular note is the work of Dr. Rochus Vogt in his role as CRS principal investigator.

This research would not have been possible without the guidance and insight of my research advisor, Dr. Edward Stone. Dr. Stone was also largely responsible for the scientific success of the Voyager mission as a whole and the CRS in particular, thanks to his role as Voyager project scientist and CRS co-investigator.

Other members of the Caltech Voyager team, whose helpful comments and suggestions are appreciated, are Dr. Alan Cummings and Dr. Stephen Christon. It is largely to Dr. Cummings that I owe my familiarity with the CRS and many of the data-analysis programs. Dr. Cummings also provided training in laboratory inspection, testing and calibration of cosmic ray detectors earlier in my graduate career. Dr. Richard Mewaldt has provided important guidance and suggestions, and supervised much of my early years as a graduate student.

Thanks are also due to Dr. Rick Cook, whose research on solar energetic particles formed the foundation upon which this work is based. Dr. Cook developed many of the analytical methods and computer programs for energy and charge calibration of the CRS telescopes which have been adapted for use in this study.

Many thanks also to the SRL staff for computer programming and operations, and especially to Nancy Collins for considerable assistance in the use of the computer.

Finally, a sincere thanks to my parents, for their encouragement, their patience and their sacrifices over the years.

This work has been supported in part by the National Aeronautics and Space Administration under contract NAS7-918 and grant NGR 05-002-160. Tuition scholarships from the California Institute of Technology are gratefully acknowledged.

Abstract

Observations of solar energetic particles (SEPs) from 22 solar flares in the 1977-1982 time period are reported. The observations were made by the Cosmic Ray Subsystem on board the Voyager 1 and 2 spacecraft. SEP abundances have been obtained for all elements with $3 \leq Z \leq 30$ except Li, Be, B, F, Sc, V, Co and Cu, for which upper limits have been obtained. Statistically meaningful abundances of several rare elements (e.g., P, Cl, K, Ti, Mn) have been determined for the first time, and the average abundances of the more abundant elements have been determined with improved precision, typically a factor of three better than the best previous determinations.

Previously reported results concerning the dependence of the fractionation of SEPs relative to photosphere on first ionization potential (FIP) have been confirmed and amplified upon with the new data. The monotonic Z-dependence of the variation between flares noted by earlier studies was found to be interpretable as a fractionation, produced by acceleration of the particles from the corona and their propagation through interplanetary space, which is ordered by the ionic charge-to-mass ratio Q/M of the species making up the SEPs. It was found that Q/M is the primary organizing parameter of acceleration and propagation effects in SEPs, as evidenced by the dependence on Q/M of time, spatial and energy dependence within flares and of the abundance variability from flare to flare.

An unfractionated coronal composition was derived by applying a simple Q/M fractionation correction to the observed average SEP composition, to simultaneously correct for all Q/M-correlated acceleration/propagation fractionation of SEPs. The resulting coronal composition agrees well with current XUV/X-ray spectroscopic measurements of coronal composition but is of much higher precision and is available for a much larger set of elements. Compared to spectroscopic photospheric abundances, the SEP-derived corona appears

depleted in C and somewhat enriched in Cr (and possibly Ca and Ti).

An unfractionated photospheric composition was derived by applying a simple FIP fractionation correction to the derived coronal composition, to correct for the FIP-associated fractionation of the corona during its formation from photospheric material. The resulting composition agrees well with the photospheric abundance tabulation of Grevesse (1984) except for an at least ~50% lower abundance of C and a significantly greater abundance of Cr and possibly Ti. The results support the Grevesse photospheric Fe abundance, about 50% higher than meteoritic and earlier solar values. The SEP-derived photospheric composition is not generally of higher precision than the available spectroscopic data, but it relies on fewer physical parameters and is available for some elements (C, N, Ne, Ar) which cannot be measured spectroscopically in the photosphere.

Table of Contents

Chapter 1

Introduction

Observations of solar energetic particles (SEPs) emitted from the sun during solar flare events are a potentially important source of information on the elemental composition of the solar atmosphere. Solar energetic particles represent a sample of solar matter whose composition is relevant to such diverse astrophysical issues as solar structure and dynamic processes, interplanetary propagation of charged particles, and stellar nucleosynthesis.

Solar composition information is obtained through a variety of techniques. These include visible and infrared spectroscopy of the photosphere, extreme ultraviolet and X-ray spectroscopy of the corona, and the more direct methods of solar wind and energetic particle measurements. In addition, solar composition is clearly tied to the issue of the composition of the solar system and the universe in general. The chemical analysis of meteorites, particularly the geochemically primitive carbonaceous chondrite classes, provides information on the chemical composition of the early solar nebula. Galactic cosmic ray measurements provide data on elemental abundances elsewhere in the galaxy.

Each of these methods has difficulties associated with it. For example, spectroscopic measurements must rely on extensive modeling of the solar atmosphere, involving many parameters not all of which are well known: temperature, density and dynamic conditions in the solar atmosphere, spectral line formation mechanisms, damping constants, atomic transition probabilities, and so on. Although meteoritic composition measurements are straightforward and capable of high precision, there are compositional differences between classes of meteorites due to enrichment/depletion processes that have altered their composition. Although the solar wind and SEPs provide a directly measured sample of solar material, the significance of the measured composition has been questioned because of its variability and the potential influence of poorly-understood acceleration and propagation effects.

Where the composition measurements differ, it is not yet clear which represent the true solar composition and what physical effects alter the others. For most elements, meteoritic and spectroscopic abundances agree within their measurement uncertainties, and the agreement appears to be improving as more accurate measurements are obtained (Grevesse 1984). Hovestadt (1974) found that the differences between SEP elemental composition and solar spectroscopic composition could be ordered by first ionization potential (FIP), the elements with high FIP being relatively depleted in SEPs. This pattern has since been confirmed by several other investigations (Webber 1975; Cook et al. 1979, 1984; McGuire et al. 1979; Meyer 1981, 1985), although all of these studies are based on only the ~12 most abundant heavy ($Z \geq 3$) elements, the only ones for which particle counting statistics and charge resolution have permitted meaningful SEP abundances to be obtained. In particular, Cook et al. (1979, 1980, 1984) found that elements with FIP > 11 eV are uniformly depleted in SEPs by about a factor of five relative to the photosphere, while elements with FIP < 8 eV are essentially equal in the photosphere and SEPs. A theoretical model of a dynamic ionization process in the solar atmosphere has been proposed to explain the FIP ordering (Geiss and Bochsler 1984). It is desirable to test, and more accurately describe, the FIP ordering by use of a larger set of SEP data that provides new abundances for many of the less abundant elements and higher-precision abundances for the more abundant elements.

Most previous SEP composition studies (e.g., Cook et al. 1979, 1980, 1984; McGuire et al. 1979; Mason et al. 1980) have noted the variability in composition from flare to flare, and that SEP composition could be described by a variation that is roughly monotonic in Z, but variable in magnitude from flare to flare, applied to an underlying characteristic composition. However, these studies generally lacked a sufficient number of flares to adequately characterize this variability. One exception to this was the recent work of Meyer (1981, 1985) which acquired a large SEP data base by collecting together observations made by several different investigative groups. In this work an unfractionated solar composition was derived by interpolating the Z-dependent fractionation within

the continuum of observed SEP compositions in such a way as to produce a composition as close as possible to the observed spectroscopic composition. However, this procedure required the equivalent treatment of diverse data sets involving different instrumentation, energy ranges, sampling time periods and analytical techniques, and is particularly sensitive to the abundance standard (in this case a combination of meteoritic and spectroscopic measurements) taken to represent the true solar composition.

Meyer (1985) also noted that the Z-dependence of this variability may reflect a difference in efficiency of acceleration and/or propagation of species with different ionic charge-to-mass (Q/M) ratios. Although ionization equilibrium calculations (Jordan 1969; Jacobs et al. 1977, 1980; Shull and van Steenberg 1982) have provided theoretical determinations of the ionic charge states present at coronal temperatures for various elements, only a limited amount of data has been available on the measured charge states of SEPs (e.g., Gloeckler et al. 1981). With the recent measurement of SEP charge states for many elements (Luhn et al. 1984), it is now possible to study in detail the dependence of acceleration and propagation effects on Q/M. This in turn presents the possibility of determining unfractionated coronal abundances by deriving a Q/M-dependent correction to the observed SEP composition.

The presence of propagation effects in SEPs has been reported in the past in the form of abundance variations with time, space and energy within single flare events. The availability of high-quality data from a large number of flare events, observed by more than one spacecraft and in various regions of the heliosphere, makes possible a more detailed treatment of possible propagation effects. Again the expected association with ionic charge-to-mass ratio may be investigated in detail.

In the present work SEP composition measurements for elements in the $3 \leq Z \leq 30$ charge range are obtained for 22 solar flare events in the 1977-1982 time period. The data were collected with solid-state charged particle detectors on board the Voyager 1 and 2 spacecraft in interplanetary space. The excellent charge resolution and collecting power and low background of this

instrumentation has yielded the largest, highest-quality SEP data set currently available. Some of the instrumentation, analytical techniques and raw data are common to the earlier study of Cook (1981), the primary advancements being in the volume of data, both in number of flares and number of particles per flare, and in refined analysis procedures.

In this study we seek to maximize statistical accuracy by studying all flares meeting a flux threshold criterion, and using energy ranges and time periods as large as possible within this constraint. This admits the possibility of acceleration/propagation effects in the form of abundances dependent on time or energy for some flares. However, we will investigate the magnitude of the propagation effects and their possible dependence on Q/M. If the acceleration and propagation fractionation affecting individual flares is ordered by Q/M, this would allow any residual acceleration/propagation fractionation present in the average SEP composition to be corrected for, yielding an unfractionated coronal composition. Motivated by the theoretical model for the FIP-associated fractionation of the corona from the photosphere, the derived coronal composition can be further corrected for FIP to yield a derived photospheric composition. The SEP measured composition as well as the SEP-derived coronal and photospheric compositions will be compared to various abundance standards: photospheric spectroscopy, coronal spectroscopy, C1 and C2 type carbonaceous chondrites, and the solar wind.

The major results of the study are the following:

(1) SEP abundances of several rare elements (e.g., P, Cl, K, Ti, Mn) have been determined for the first time, and the average abundances of the more abundant elements with $3 \leq Z \leq 30$ have been determined with improved precision, typically a factor of three better than the best previous determinations.

(2) Previously reported results concerning the FIP-dependent fractionation of SEPs relative to photosphere have been confirmed and amplified upon with the new data. The monotonic Z-dependence of the variation between flares observed in the past was demonstrated to be actually a monotonic Q/M-

dependence. It was found that the Q/M ratio is the primary organizing parameter of acceleration and propagation effects in SEPs, as evidenced by the dependence on Q/M of temporal, spatial and energy dependence within flares and the abundance variability from flare to flare.

(3) An unfractionated coronal composition was determined by deriving a single-parameter Q/M fractionation correction to the observed SEP composition, to simultaneously correct for all Q/M-correlated acceleration/propagation fractionation of SEPs. The resulting coronal composition agrees well with current XUV/X-ray spectroscopic measurements of coronal composition but is of much higher precision and is available for a much larger set of elements. Compared to spectroscopic photospheric abundances, the SEP-derived corona is depleted in the high-FIP elements N, O, Ne, Cl, and Ar by about a factor of four and is somewhat enriched in Cr (and possibly Ca and Ti). C is depleted by a factor of six and P and S by a factor of 1.5 - 2.

(4) An unfractionated photospheric composition was derived by applying a simple FIP fractionation correction to the derived coronal composition, to correct for the FIP-associated fractionation of the corona during its formation from photospheric material. The resulting composition agrees well with the photospheric abundance tabulation of Grevesse (1984) except for an at least ~50% lower abundance of C and a significant excess of Cr and possibly Ti. The results support the Grevesse photospheric Fe abundance, about 50% higher than meteoritic and earlier solar values. The SEP-derived photospheric composition is not generally of higher precision than the available spectroscopic data, but its determination involves fewer free parameters and it can be carried out for many elements (e.g., C, N, O, Ne, Ar) which are difficult or impossible to observe spectroscopically in the photosphere.

Chapter 2

The Experiment

2.1 The Voyager Spacecraft and its Mission

The observations to be described here were made using data from the Cosmic Ray Subsystem (CRS) experiment on board the Voyager 1 and 2 spacecraft. The spacecraft were launched on September 5 and August 20, 1977, respectively. Their mission was to perform multidisciplinary studies of Jupiter and Saturn, their satellites and magnetospheres, the rings of Saturn, and the interplanetary medium from the orbit of Earth to beyond the orbit of Saturn. Voyagers 1 and 2 encountered Jupiter on March 5 and July 9, 1979, respectively, with Saturn encounters following on November 12, 1980 and August 25, 1981. In addition, Voyager 2 is continuing toward an encounter with Uranus in 1986 and with Neptune in 1989, while Voyager 1 is climbing up out of the ecliptic plane, reaching a heliographic latitude of about 17° as of January 1983 (Fig. 2.1).

2.2 Cosmic Ray Subsystem (CRS)

The Cosmic Ray Subsystem (CRS) experiment carried by each Voyager consists of four Low Energy Telescopes (LETs), two High Energy Telescopes (HETs), The Electron Telescope (TET) and associated electronics. With these instruments it is possible to measure the energy spectrum of electrons over the 3 - 110 MeV energy range, and the energy spectra and nuclear charge of atomic nuclei from hydrogen through zinc over the 3 - 500 MeV/nucleon energy range. The TET telescope is not involved in the present study. The exclusive use of solid-state detectors in the CRS telescopes is designed to achieve the objectives of reliability over a long mission life, high resolution determinations of energy and charge, and high-count-rate capability during large solar flares and passage through the magnetospheres of the outer planets. The Voyager CRS experiment is a collaborative effort involving scientists and engineers at the

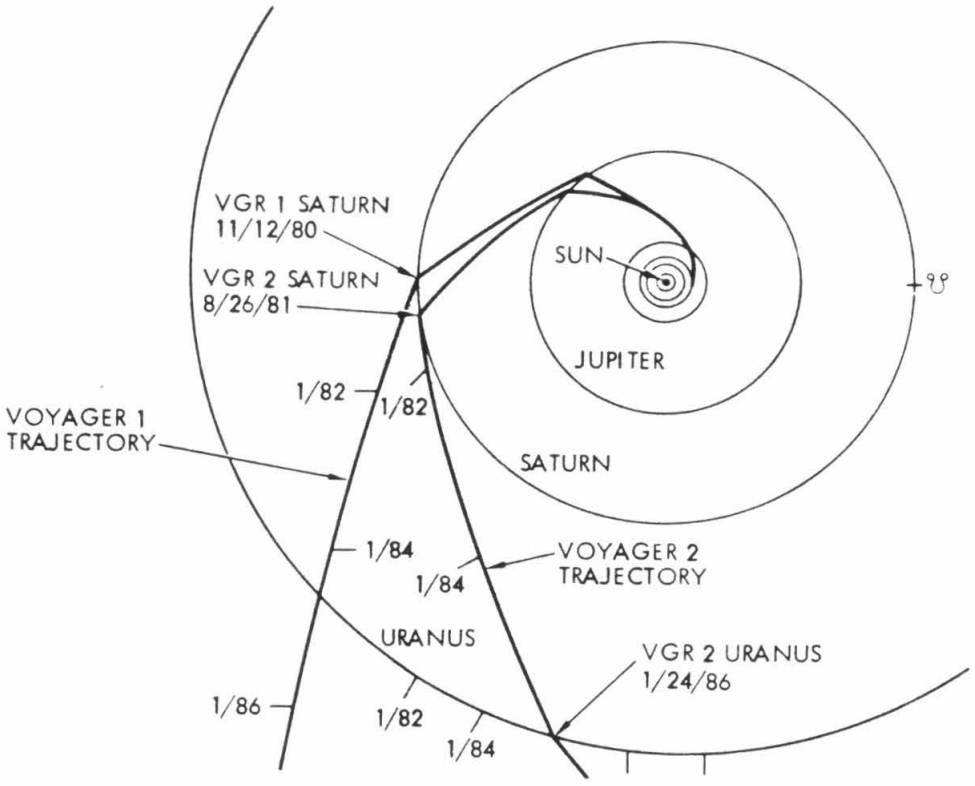

Fig 2.1 Ecliptic projection of the Voyager spacecraft trajectories from Earth to beyond the orbit of Saturn.

California Institute of Technology, the Goddard Space Flight Center, the University of Arizona, and the University of New Hampshire. A general description of the CRS investigation may be found in Stone et al. (1977).

2.3 Low Energy Telescope (LET)

Each Voyager spacecraft carries four nominally identical LET telescopes, denoted A, B, C, and D. The four telescopes have a combined geometry factor of about 1.7 cm^2sr and are oriented in orthogonal viewing directions to provide three-dimensional information on charged particle anisotropies. The telescopes use the dE/dx - E method (to be described in Section 2.6) to measure the kinetic energy and nuclear charge Z of individual nuclei in the range $1 \leq Z \leq 30$. The energy range covered by the LETs varies from about 3 - 8 MeV/nucleon for protons and alpha particles to about 3.5 - 17 MeV/nucleon for oxygen nuclei and 5 - 30 MeV/nucleon for Fe.

Each LET consists of four totally depleted silicon surface barrier detectors, designated L1 through L4. L1 and L2 are nominally identical 35μm-thick detectors whose active area is defined by the position of vapor-deposited aluminum and gold contacts of about 2 cm diameter on opposite faces of the silicon wafer. Detectors L3 and L4 are 450μm thick and have an active area about 2.4 cm in diameter. The front of each LET is covered by a 3μm-thick aluminum foil "window" for protection from sunlight and associated thermal effects. (Fig. 2.2a).

Under normal circumstances a coincidence of discriminator signals from L1 and L2 is required for pulse height analysis, and detector L4 is kept in anticoincidence. Thus the particle events of interest are those passing through L1 and stopping in either L2 or L3. These are denoted as "two-parameter" and "three-parameter" events respectively, referring to the number of nonzero pulse heights available for energy and charge calculations.

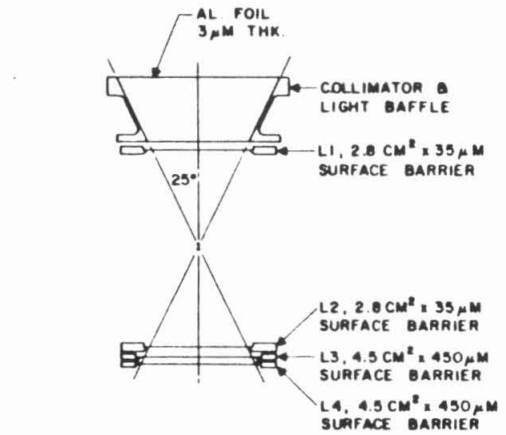

LOW ENERGY TELESCOPE (LET)

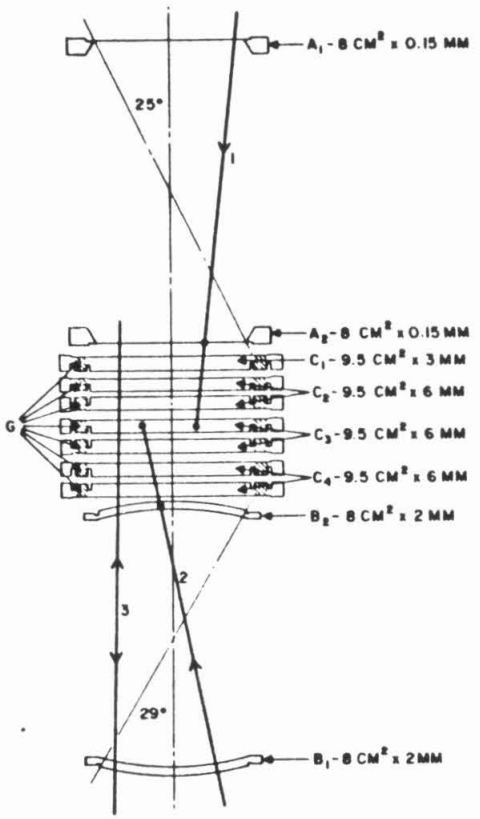

HIGH ENERGY TELESCOPE (HET)

Fig. 2.2. Schematic cross-sections of LET and HET, the two charged particle telescope designs involved in this study. Together with TET (not shown) and associated electronics, they comprise the Voyager Cosmic Ray Subsystem (CRS); each Voyager carries four LETs, two HETs and one TET.

2.4 High Energy Telescope (HET)

Each Voyager carries two nominally identical HET telescopes, denoted HET-1 and HET-2. They are double-ended telescopes oriented perpendicularly in space. The "A"-end entrance aperture is defined by two 150μm-thick silicon surface barrier detectors, A1 and A2, and the "B"-end aperture is defined by two 2mm-thick curved Li-drifted detectors, B1 and B2. Energetic particles entering either end of the telescope stop in a central stack of seven 3mm-thick double-grooved Li-drifted detectors. These are electronically connected as four separate central areas, denoted C1 through C4, and four annular guard regions used for anticoincidence. Penetrating events, which pass through the entire detector stack, can also be observed (Fig. 2.2b). Both ends of HET are covered by a window of aluminized Mylar, ¼-mil thick at the A-end, 1 mil thick at the B-end. In addition, the entire telescope is surrounded by a Mylar/Kapton thermal blanket with a combined thickness of 2.5 mils at both apertures. The geometry factor of the A-end of one HET is about 1.1 cm^2sr.

The incident energy of oxygen nuclei entering the B-end of HET ranges from about 45 MeV/nucleon for particles stopping in B2, to about 160 MeV/nucleon for particles stopping in the C detector stack just before C1. For iron, the corresponding energies are 75 and 320 MeV/nucleon, respectively. The energy spectra of solar energetic particles, which generally fall steeply at high energies, result in very few SEPs being observable with the B-end of HET. Those that are seen make a negligible contribution to the event statistics of the overall SEP data set and are significantly contaminated by the galactic cosmic ray background flux which is becoming important at these energies. Hence HET B-end data were not included in this study. For the same reasons, only HET A-end particles stopping in detectors A2 or C1 were included, since A-end particles stopping deeper in the C stack have energies comparable to B-end events. Thus the only HET data included in this study are particles entering A1 and stopping in A2 or C1. The energy interval for this data set is 10 - 50 MeV/nucleon for oxygen, and 20 - 100 MeV/nucleon for iron. It can be seen

that these energy intervals overlap those of LET, so there is uninterrupted SEP energy coverage of oxygen from 3.5 to 50 MeV/nucleon, and of iron from 5 to 100 MeV/nucleon. In parallel with the LET nomenclature, HET particles stopping in A2 are referred as "two-parameter" events, and those stopping in C1 as "three-parameter" events.

2.5 CRS Electronic Data System

When a charged particle passes through one of the CRS telescopes, signals from the detectors are fed through charge-sensitive preamplifiers and shaping amplifiers to the analog signal processor. The preamplifier gain can be switched by a factor of about five on command. This is necessary for the HET telescopes where the dynamic range of interest is too large for the PHA system. The high-gain mode can analyze charges up to Mg and is used mainly for elemental and isotopic studies of H and He. The low-gain mode extends up to Z = 30 and is used for heavy element studies; only low-gain data are used throughout this study.

The analog signal processor consists of threshold discriminators and coincidence/anticoincidence circuits for each telescope and three sets of 4096-channel pulse height analyzer systems shared between several telescopes. The discriminators and coincidence/anticoincidence circuits are used to decide for which events pulse height analysis will be carried out. Two LETs and one HET share a common subsystem, referred to as a HET/LET Block. Thus LETs A and B and HET 1 constitute Block I, and LETs C and D and HET 2 form an identical Block II.

Prior to pulse height analysis, individual detector signals are fed into precision linear summing amplifiers to produce certain specific linear combinations. These "slant" terms are used to separate high-Z ($Z \geq 3$) particles from low-Z ($Z < 3$) events in the different telescopes.

The signals to be pulse-height-analyzed are passed through additional summing amplifiers to the 4096-channel ADCs. The summations of various detectors on different telescopes are arranged so that common circuits may be used to analyze different types of events in different telescopes. This results in no ambiguity since the detector signals combined are mutually exclusive for normal events. The actual type of event is specified by the discriminators referred to above. A readout polling system in each block scans the PHA registers for the presence of data, in order to optimize use of available telemetry. The manner of polling ensures that rare events get equal priority with other classes of events when high counting rates, as in large solar flares, cause the PHA event readout rate to be telemetry-limited.

In addition to PHA event data, 30 rate counters in the CRS system generate a variety of single-detector and coincidence counting rates. Among other things, these are used to obtain absolute flux measurements by providing normalization for the PHA event sample.

Table 2.1 lists the coincidence requirements, detectors analyzed and approximate oxygen and iron energy intervals for the different classes of LET and HET events included in this study. More details on the CRS electronic data system may be found in Garrard (1976) and Stilwell et al. (1979).

2.6 dE/dx - E Method for Calculating Z

The nuclear charge of individual charged particles are measured using the dE/dx - E method. Particles that may not have been fully stripped while in free space are completely ionized by passing through the telescope's window, so the actual charge of the ion is the nuclear charge. The incident nucleus with charge Z, mass M, kinetic energy E and range R passes through a thin front detector of thickness L, losing energy ΔE through ionization; it then stops in a second detector, losing its remaining energy $E' = E - \Delta E$. Since the rate of energy loss, dE/dx, depends on Z, the proportion of E deposited in the first

Table 2.1. Coincidence requirements, detectors analyzed, and approximate oxygen and iron energy ranges for the classes of LET and HET events contributing to this study. "SL" denotes "slant" requirement that selects particles with $Z \geq 3$. "G" denotes triggering of annular guard regions of HET "C" detectors.

Telescope	Coincidence Requirements	Detectors Analyzed	Oxygen Energy Range (MeV/nuc)	Iron Energy Range (MeV/nuc)
LET	$L1*L2*\overline{L3}*\overline{L4}*SL$	L1, L2	3.7 - 5.5	5.0 - 8.0
LET	$L1*L2*L3*\overline{L4}*SL$	L1, L2, L3	5.5 - 17.	8.0 - 30.
HET	$A1*A2*\overline{C1}*\overline{C4}*\bar{G}$	A1, A2	11 - 15.	20. - 25.
HET	$A1*A2*C1*\overline{C4}*\bar{G}$	A1, A2, C1	15. - 54.	25. - 100.

detector as ΔE will be dependent on the nuclear species. If both ΔE and E' are known, as well as an adequate range-energy relation R(E,Z,M), one can solve for Z if reasonable assumptions are made about M. For example, if the range-energy relation is given by $R(E,Z,M) = \frac{kM}{Z^2}\left(\frac{E}{M}\right)^{\alpha}$ (a fair approximation at high energies with $\alpha \sim 1.77$), then one has the equations

$$R = \frac{kM}{Z^2}\left[\frac{(\Delta E + E')}{M}\right]^{\alpha} \tag{2.1}$$

$$R - L = \frac{kM}{Z^2}\left(\frac{E'}{M}\right)^{\alpha} \tag{2.2}$$

where R - L is the residual range in the second detector.

If one makes the approximation M = 2Z, these equations may be solved for Z.

$$Z = \text{constant} \times \left[(E'+\Delta E)^{\alpha} - (E')^{\alpha}\right]^{\frac{1}{\alpha+1}} \tag{2.3}$$

With nuclei for which M ≠ 2Z, this algorithm produces small but predictable shifts in the calculated charge; the shift in Z is about 1/7 of a charge unit per atomic mass unit deviation from 2Z.

In practice R(E,Z,M) is not known analytically, but only as a tabulated function, and the solution for Z must be obtained iteratively. This process will be explained in detail in Section 3.1.

If the particle passes through two detectors and stops in a third (i.e., it is a "three-parameter" event), then the two ΔE measurements available can be used to generate two independent charge estimates; in one case using the first detector as ΔE and the sum of the second and third as E', in the other case using the second detector as ΔE and the third as E'. This additional information can be used to significantly reduce spurious effects in the data, an important consideration for the rarer elements.

The identification of elements using ΔE and E' can be displayed in a scatterplot of ΔE vs. E' (Fig. 2.3); two such plots can be produced for three-parameter events. The "tracks" of the relatively abundant elements are apparent. The finite width of the tracks is due mainly to fluctuations in the ionization energy loss as a function of incident energy, and to variability in the pathlength L traversed by a given particle in the ΔE-detector. Both incident angle differences and detector thickness nonuniformities contribute to the latter variability.

2.7 Calibrations

2.7.1 Detector Thicknesses and Active Areas

The thicknesses and active areas of the LET detectors were measured in the laboratory prior to incorporation in the CRS instrument. The active area measurements were combined with L1-L2 separation distances measured during assembly of LET to obtain the geometry factor for each telescope. These measurements and calculations are described in detail by Gehrels and Cummings (1980).

For the HET detectors, no thickness measurements were performed after delivery by the manufacturer. The thicknesses of A1 and A2 used in the data analysis are arithmetic averages of five measurements made by the manufacturer, ORTEC, at five different locations on each detector's surface. To convert these to mean pathlengths through the detector, they were multiplied by a $\langle \sec\Theta \rangle$ factor to account for the expected distribution of incidence angles Θ. The value used for HET was $\sec(13°) \simeq 1.026$. Thicknesses of the lithium-drifted detectors were also supplied by their manufacturer, Kevex, but these values are unimportant for this study except to define the upper limit of the energy range covered, when particles traverse all of detectors A1, A2 and C1. An unsuccessful attempt was made to improve on the manufacturer's thicknesses for the HET ΔE-detectors by fitting oxygen flight data (see Appendix A).

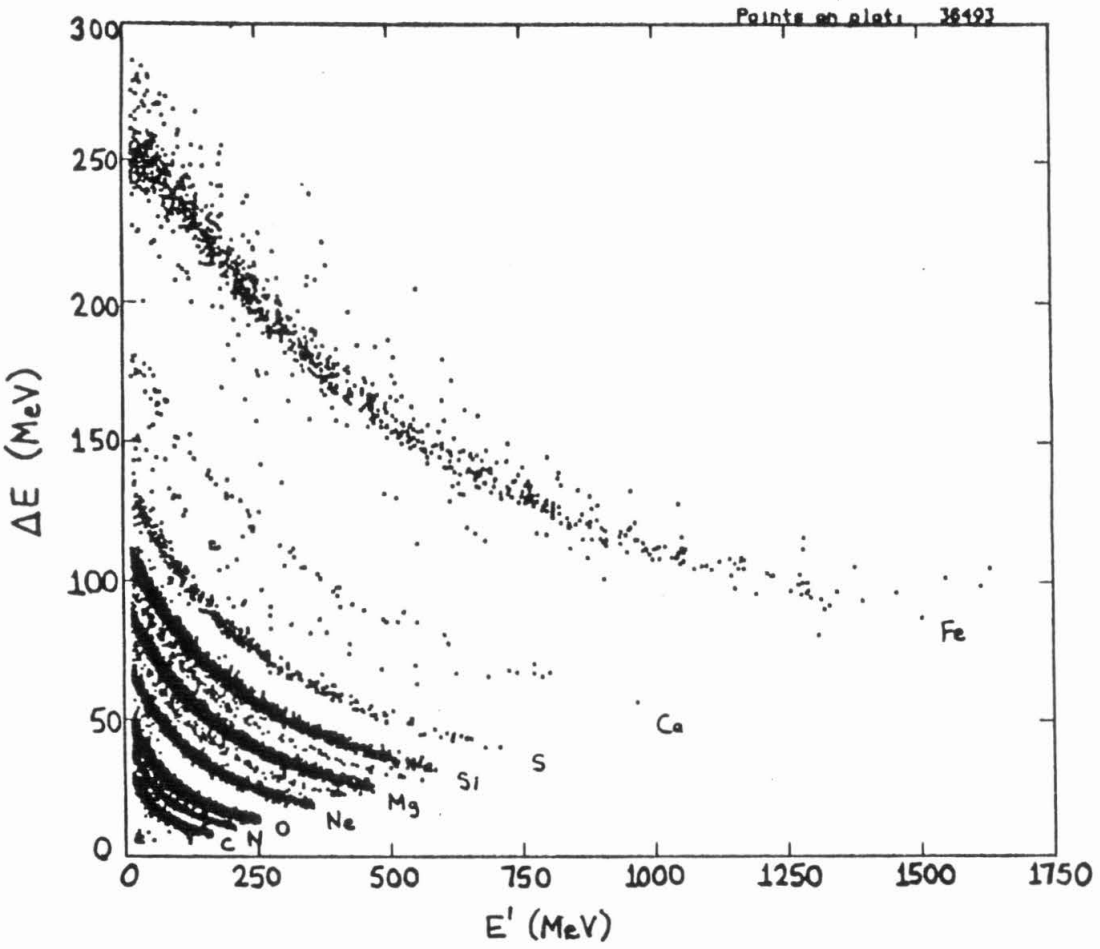

Fig. 2.3. Scatterplot of E' (energy deposited in the stopping detector) vs. ΔE (energy deposited in passing through an earlier detector) for a sample of solar energetic particle data from LET. The dependence of dE/dx on Z allows one to distinguish nuclei of different elements. Note the well-defined "tracks" of the abundant elements C, N, O, Ne, Mg, Si, S and Fe, and the less-populated tracks of the rarer elements Na, Al, Ar and Ca.

Active areas of the HET "A" detectors were also not measured directly, and the active area is less well-defined since the vapor-deposited metal electrodes extend to the edge of the detectors. The active areas, and hence the geometry factors, were inferred by requiring flux measurements from flight data to agree between LET and HET in their region of energy overlap. It was found that achieving this agreement required a 6% reduction in detector effective area relative to the geometrical area supplied by the manufacturer. This can be explained in terms of "edge effects," i.e., reduced efficiency of the detector for particles passing near the edge of the silicon wafer. The same telescope-averaged values were used for all of the HETs; there is evidence from quiet-time flight data that the individual HET geometry factors differ from each other by ~10% (Cummings 1981).

The adopted mean pathlengths of all LET and HET ΔE and E' detectors involved in this study are listed in Table 2.2. The adopted geometry factors are listed in Table 2.3.

2.7.2 Window Thicknesses

The thickness of the aluminum window at the entrance of each LET was not measured in the laboratory; the manufacturer's specified thickness of 3μm was used to correct incident particle energies for the unmeasured energy loss in the window. This is a small correction since the window thickness is small compared to the ~35μm thickness of the L1 detectors.

The combination of aluminized Mylar window and Mylar/Kapton thermal blanket covering the A-end aperture of HET is equivalent in stopping power to about 50μm of Si, based on the thickness figures supplied by the manufacturers. This was the figure used in the data analysis to correct the particle incident energies.

Table 2.2. Adopted mean pathlengths in the Voyager LET and HET detectors. The values for LET were measured in the laboratory (Gehrels and Cummings 1980); those for HET were calculated from manufacturer-supplied detector thicknesses (Cummings 1981). The uncertainties quoted for LET are the r.m.s. deviation of the pathlength distribution. The uncertainties for the HET detectors represent the nonuniformity of thickness of the detector and are calculated as the standard deviation of the five thickness measurements performed by the manufacturer at different positions on the detector face. As with the LETs, there is also a ~2% variation in pathlength due to incident angle variation. Based on comparison of the SRL laboratory measurements and the manufacturer's measurements for the LET 450-μm detector thicknesses, there is evidence that the manufacturer's values may be high by ~8%, and this may apply to the values supplied for the HET detectors as well.

		Detector mean pathlength, μm		
VGR	LET	L1	L2	L3
1	A	37.91 ± 0.66	35.46 ± 0.82	409.3 ± 13.2
1	B	30.91 ± 0.64	38.51 ± 0.99	398.3 ± 11.5
1	C	37.07 ± 0.98	33.07 ± 0.63	411.9 ± 21.0
1	D	35.45 ± 0.72	34.66 ± 0.80	414.8 ± 15.1
2	A	34.35 ± 1.03	36.23 ± 0.72	461.2 ± 7.2
2	B	38.55 ± 0.81	30.67 ± 0.81	428.0 ± 18.9
2	C	35.33 ± 0.97	34.04 ± 0.77	475.2 ± 11.4
2	D	34.76 ± 0.65	36.21 ± 0.92	408.5 ± 18.6

		Detector mean pathlength, μm		
VGR	HET	A1	A2	C1
1	1	150.3 ± 0.8	149.3 ± 1.0	3214.
1	2	150.7 ± 1.4	149.7 ± 0.5	3040.
2	1	146.2 ± 0.9	142.3 ± 0.9	3035.
2	2	151.5 ± 1.3	150.2 ± 0.7	3168.

Table 2.3. Adopted geometry factors of the Voyager LET and HET telescopes. Values for the LETs were calculated from laboratory-measured detector spacings and active areas (Gehrels and Cummings 1980) and have an uncertainty of ± 0.0012 cm^2sr.

telescope	geometry factor (cm^2sr)
Voyager 1 LET A	0.4366
Voyager 1 LET B	0.4364
Voyager 1 LET C	0.4338
Voyager 1 LET D	0.4312
Voyager 2 LET A	0.4344
Voyager 2 LET B	0.4341
Voyager 2 LET C	0.4295
Voyager 2 LET D	0.4357
all HET 2-parameter	1.096
all HET 3-parameter	1.167

2.7.3 Detector Deadlayer Thicknesses

The thickness of the deadlayer for silicon surface-barrier detectors can be taken as the thickness of the vapor-deposited aluminum and gold electrodes. For the LET detectors, the ORTEC-supplied thicknesses for these layers were all within the range of 40.0 ± 0.6 $\mu g/cm^2$. This is negligible compared to the total thickness of the detectors in question (about 0.5% for the 35μm LET detectors), so its effect could be ignored in subsequent particle energy calculations. Similar statements may be made regarding the HET A1 and A2 surface-barrier detectors. Although the lithium-drifted "C" detectors in HET have substantial deadlayers in the range of 60 - 100 μm on their grooved sides, this has no effect on the present work since only "A"-end particles travelling as far as C1 are considered, and this detector is oriented with the ungrooved side facing the "A" end of the telescope. The "C" detectors also have a ~40 $\mu g/cm^2$ layer of gold on the ungrooved side, but again this is negligible compared to the detector thickness and was ignored in the particle energy calculations.

2.7.4 Pre-Flight Energy Calibration

The preamp-postamp-PHA electronics of the LETs and HETs were calibrated in the laboratory; these measurements, described in detail by Povlis (1980), are summarized briefly here. A charge pulse from a precision pulser was fed into the preamp input and the resulting pulse height was read out, for ~4-12 different channels spanning the PHA dynamic range, and at two different temperatures, 0° and 20° C. This information on the charge-PHA dependence can be related to the energy deposited in the detector by an ionizing particle; for a silicon detector, 3.62 eV of energy is required per electron-hole pair formed. Applying the calibration to flight data requires interpolation between and perhaps (for temperature) extrapolation beyond the calibrated points; this can be done linearly with little error since the calibration measurements showed that the dependence of pulse height on input charge was linear to within 2% of full scale at one temperature, and varied by no more than 2% between the two

temperatures. An additional small correction to the calibration was applied later using flight data; this is described in Appendix A.

Chapter 3

Data Analysis

3.1 Charge Calibration

After the gain correction factors obtained in Table A.1 (Appendix A) were applied to the detector energy losses, the nuclear charge Z could be calculated from the known mean pathlengths in the detectors, the range-energy relation R(E,Z,M), and an assumed value of M, as described in Section 2.6. Since the range-energy relation is not given by an analytic function but by a tabulated function, the calculation of Z must be carried out iteratively. Moreover, different tabulated functions are available and they only approximate the actual range-energy relation. So it is necessary, in order to get accurate charge assignments, to apply a correction to R(E,Z,M); the correction term contains free parameters whose values are obtained by fitting the data for the more abundant elements where the correct charge assignment is obvious. This is analogous to the procedure used on the LET data by Cook (1981) but with some modifications.

The form of the range-energy relation used is that given by Heckman et al. (1960):

$$R(E,M,Z) = \frac{M}{Z^2} R_p\left(\frac{E}{M}\right) + MZ^{\frac{2}{3}} C\left(\frac{137\beta}{Z}\right) \qquad (3.1)$$

where the function C, the "range correction term," has the parametric form

$$C(x) = A_3 A_2 \left[\exp\left(-\frac{x}{A_3} - \frac{x^2}{A_6}\right) - 1\right] + A_1 A_4 - A_1 A_6 \ln\left[1 + \exp\left(\frac{A_4 - x}{A_5}\right)\right] \qquad (3.2)$$

This is a semi-empirical result derived from measurements of heavy ion ranges in nuclear emulsion. The first term is the proton range-energy relation R_p of Janni (1966) scaled to particles of arbitrary charge and mass. The second

term attempts to correct for the charge-pickup effect which is becoming significant at the low end of the LET energy range for particles of high charge ($Z \sim 26$).

The values of the A_i were obtained by fitting the data for each of the elements oxygen, neon, magnesium, silicon and iron. For the HETs, this was done separately for each telescope and separately for 2- and 3-parameter events. Since the HET energy calibration contains random errors due to relatively large uncertainties in the detector thicknesses, the "range correction function" was treated as an overall calibration correction term with limited physical significance, and whose parameters therefore need not be constant as a function of Z or E. For the LETs, the precise pre-launch detector thickness measurements resulted in a lower random error in the calibration, so one set of range correction parameters could serve well for all LET telescopes and for 2- and 3-parameter events. However, since Cook (1981) found that it was necessary to compromise the quality of the fit somewhat in order to use the same set of parameters for Ne, Mg, Si and Fe, it was decided to fit the elements O, Ne, Mg, Si and Fe separately as was done with HET. In addition, a separate fit was done for 2-parameter and 3-parameter Fe, on account of the relatively large charge-pickup effect for this element at the low LET energies. The events used for the fit were from flare period #7, grouped in E' bins of between 10 and 100 events each, depending on the available statistics. In some cases the earlier flare periods, particularly flare period #1, were included to improve the statistics on Fe.

The end result of this procedure was 46 sets of 6 correction parameters, 40 sets for HET and 6 sets for LET; these are listed in Appendix B, in Tables B.1 and B.2 respectively. The correction to be used for a particle with given Z and E was obtained by linearly interpolating between the values of $C(x)$ evaluated at the same energy E for the adjacent fitted elements. No particular significance is attached to the trends with Z, or lack of such trends, in the values of the parameters A_i themselves, because the six parameters provide too many

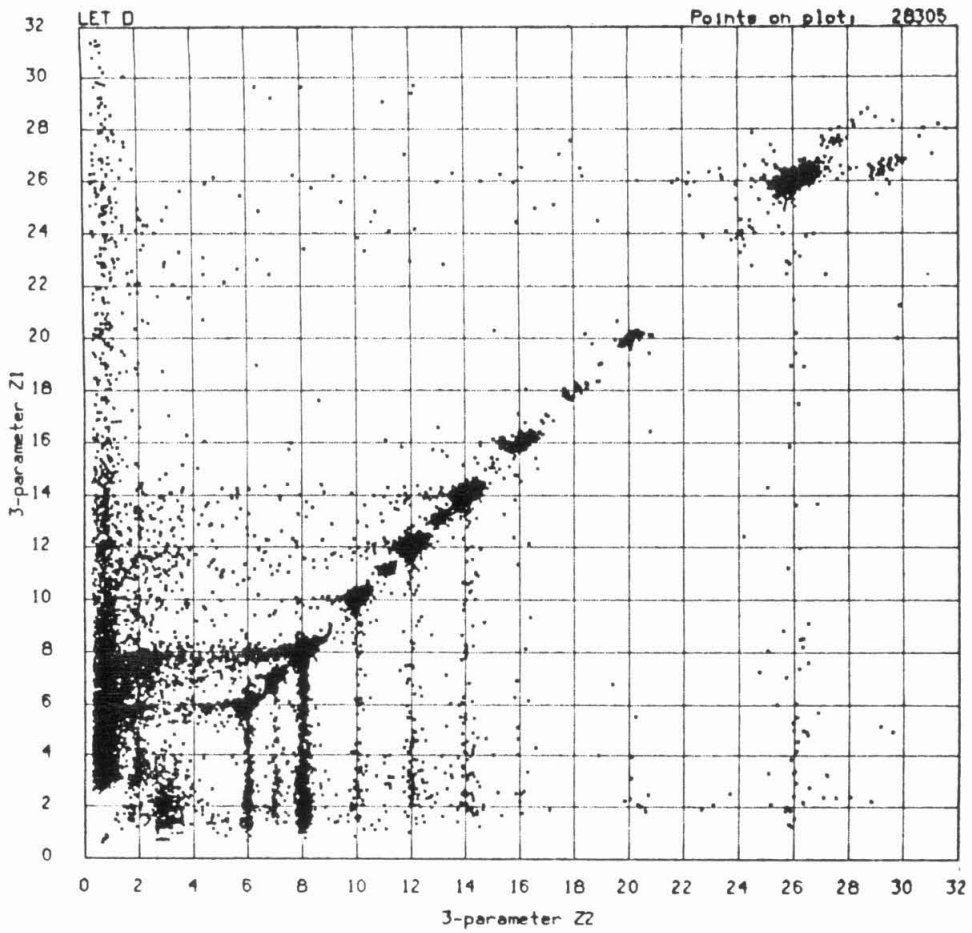

Fig. 3.1. Scatterplot of Z_1 vs. Z_2 for three parameter data from Voyager 1 LET D for flare period 7. The two independent measurements of Z are used to reduce background by selecting out a band along the diagonal where the two Z determinations agree. The off-diagonal points are caused by the various background mechanisms described in Section 3.2 of the text.

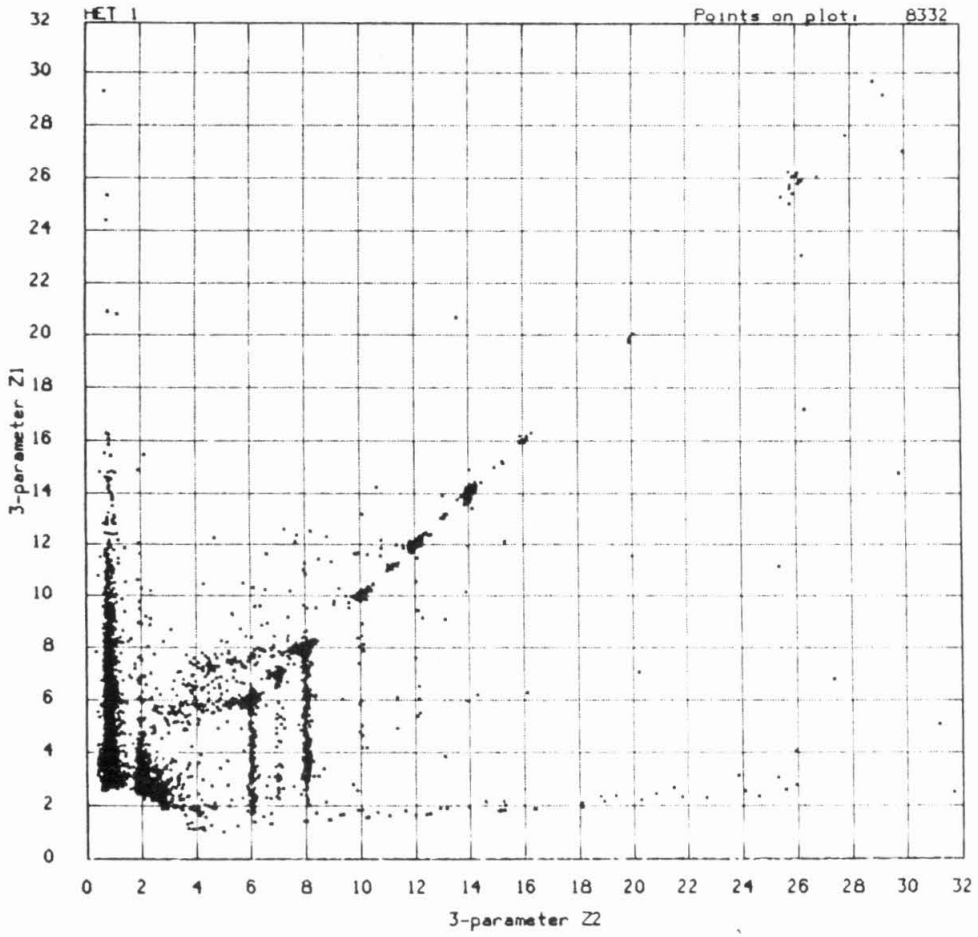

Fig. 3.2. Scatterplot of Z_1 vs. Z_2 for three-parameter data from Voyager 2 HET 1 for flare period 7. The background mechanisms responsible for the off-diagonal points are described in the text.

degrees of freedom, i.e., the parameter-space contains large regions that yield quantitatively similar functions $C(\boldsymbol{x})$. The iterative fitting process often changed two or more parameters by large amounts in a correlated fashion without significantly affecting the quality of the fit.

As noted above the iterative process for calculating Z requires an assumed value for M. The value of M assumed during a given iteration is related to the value of Z obtained on the previous iteration by

$$M(Z) = \begin{cases} 2Z, & Z \leq 20 \\ 40 + 4.772(Z-20), & 20 \leq Z < 21 \\ 2.132Z, & Z \geq 21 \end{cases} \qquad (3.3)$$

This is a good approximation for the even-Z elements in the range $6 \leq Z \leq 20$ and for iron, but in every case the displacement in Z resulting from the approximation is small and predictable (see Eq. 3.10); it is explicitly taken into account in determining the rare element abundances (Section 3.6).

3.2 Charge Consistency for Three-Parameter Events

As described in Section 2.6, two semi-independent charge determinations can be made for three-parameter events, in one case by using the energy deposited in the first detector as ΔE and the sum of the second two as E', and in the other case by using the energy deposited in the second detector as ΔE and the third as E'. These two determinations of Z will be denoted Z_1 and Z_2 respectively. A crossplot of Z_1 and Z_2 (shown in Fig. 3.1 for one LET and in Fig. 3.2 for one HET) arrays the various elements along the 45° diagonal, and also reveals a number of background sources present in the data which give an incorrect charge assignment for some particles.

For example, the vertical streaks extending downward from the diagonal in Figs. 3.1 and 3.2 are caused by "edge effects" in the L1 detector, i.e., the reduced efficiency of charge collection for a particle passing near the edge of the detector's active area. The PHA signal from this detector is abnormally low

for such a particle, while the PHAs from L2 and L3 are normal, hence the calculated Z_1 is low while Z_2, which does not depend on the L1 ΔE, is correct. An analogous edge effect in the L2 detector accounts for the roughly horizontal streaks to the left of the diagonal; the streaks are diffuse and slightly curved because both the Z_1 and the Z_2 calculations involve the L2 ΔE. The vertical band along the left edge can be explained in terms of the accidental coincidence of a low-energy heavy ion stopping in L1 with a proton passing through L1 and L2 and stopping in L3. The L2 and L3 signals, and hence Z_2, are appropriate to a Z = 1 particle, but the excessively high L1 energy loss results in an anomalously high Z_1 value. Such effects, as well as electronic "pileup" involving protons and alpha particles, nuclear interactions of these particles in the detectors or surrounding matter, and the anomalous instrumental effects described in Appendix G, account for most of the observed background.

By requiring the two Z-determinations to agree with each other, one selects out the band of data along the diagonal and greatly reduces the background that would be present in either Z-determination by itself. This can be illustrated further by defining two new charge parameters,

$$\langle Z \rangle = \tfrac{1}{2}(Z_1+Z_2) \tag{3.4}$$

$$\Delta Z = Z_1-Z_2 \tag{3.5}$$

the mean and difference of the two charge determinations. The charge consistency requirement imposed on the three-parameter LET data may be expressed as

$$|\Delta Z| < \frac{\langle Z \rangle^2}{800} + 0.1876 \tag{3.6}$$

and for HET it takes the form

$$|\Delta Z| < \frac{3\langle Z \rangle + 96}{640} \tag{3.7}$$

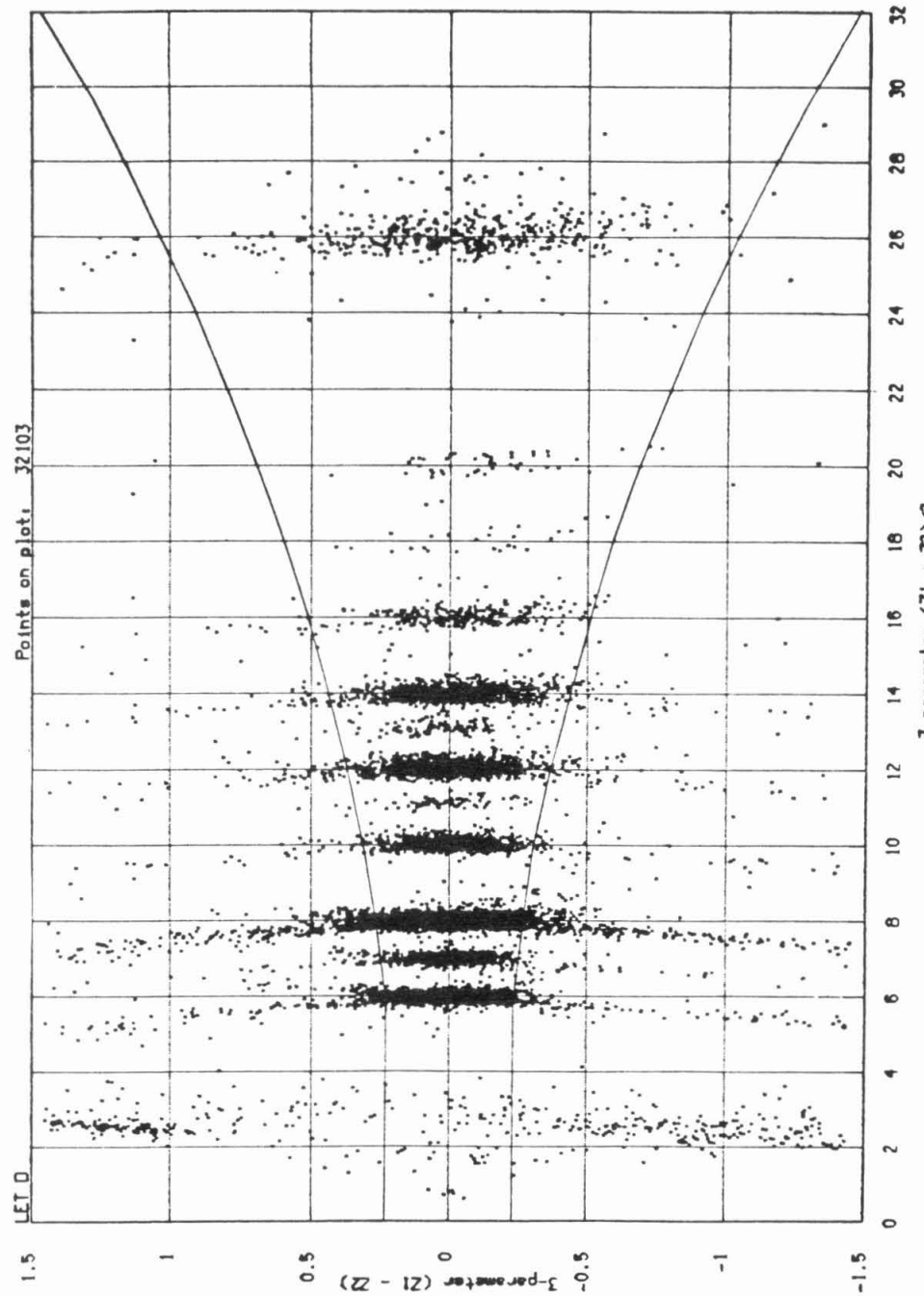

Fig. 3.3. Scatterplot of <Z> vs. ΔZ for three-parameter data from Voyager 1 LET D for flare period 7. Also shown is the charge-consistency requirement imposed on all LET data to remove background events. This requirement retains 95% of the good LET data for each element.

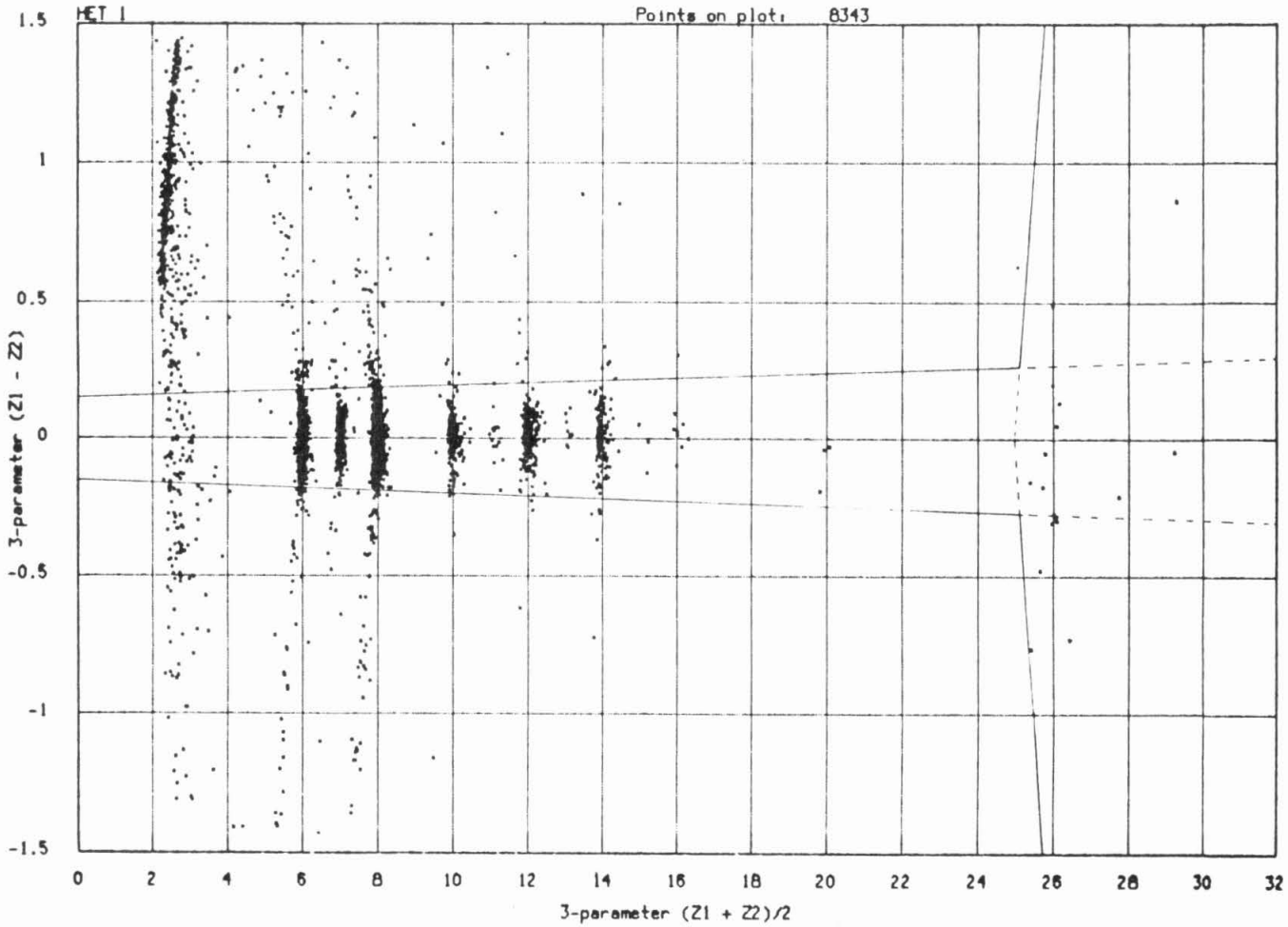

Fig. 3.4. Scatterplot of <Z> vs. ΔZ for three-parameter data from Voyager 2 HET 1 for flare period 7. Also shown is the charge-consistency requirement imposed on all HET data for background removal. This requirement retains 95% of the HET data for each element; it is stricter than the LET requirement on account of the inherently better charge resolution of the HET telescope.

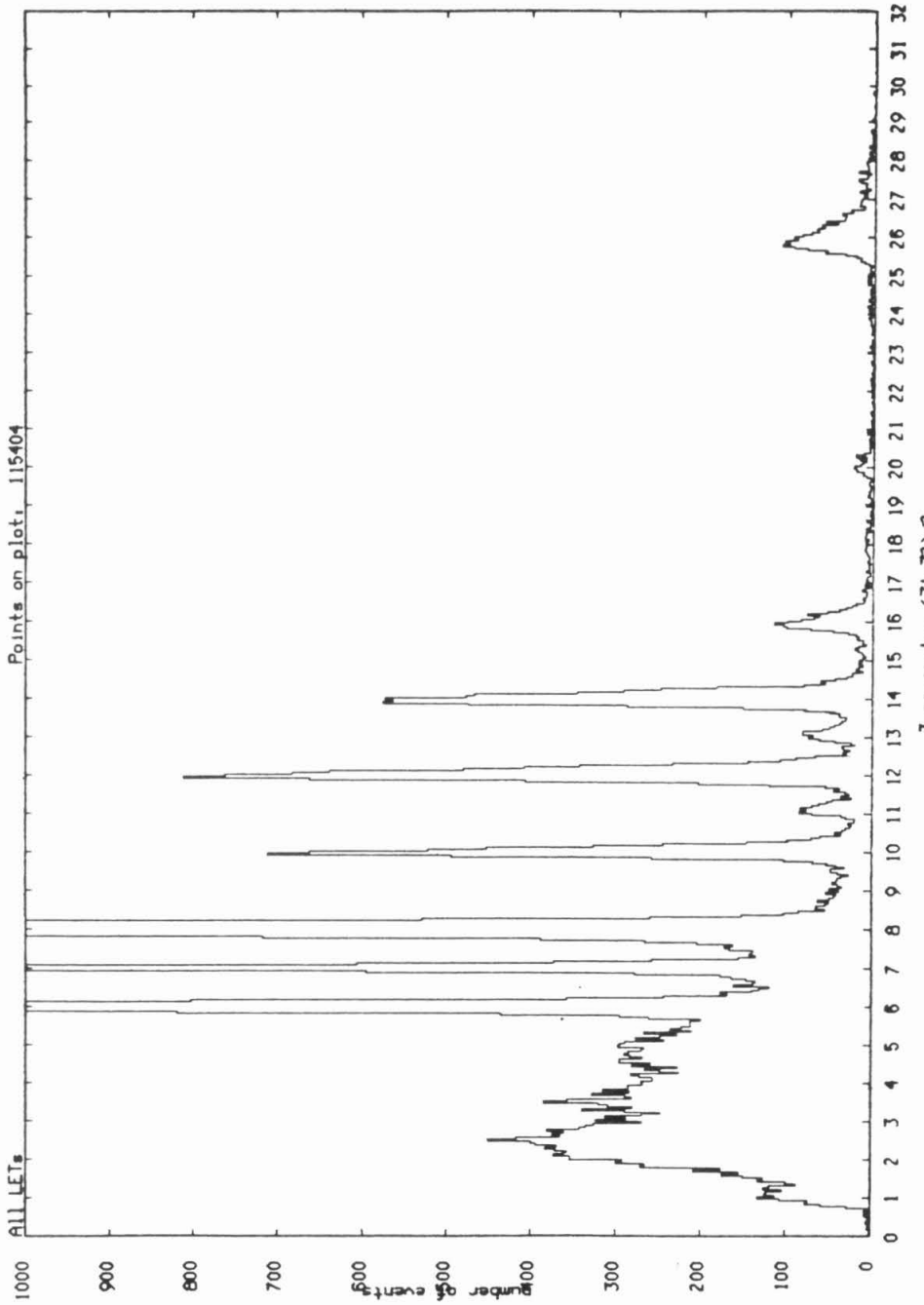

Fig. 3.5. Histogram of <Z> for three-parameter data from all Voyager 1 LETs before imposition of the charge consistency requirement. This figure is to be compared with Fig. 3.6. Note the high level of background in the data, especially at low charges.

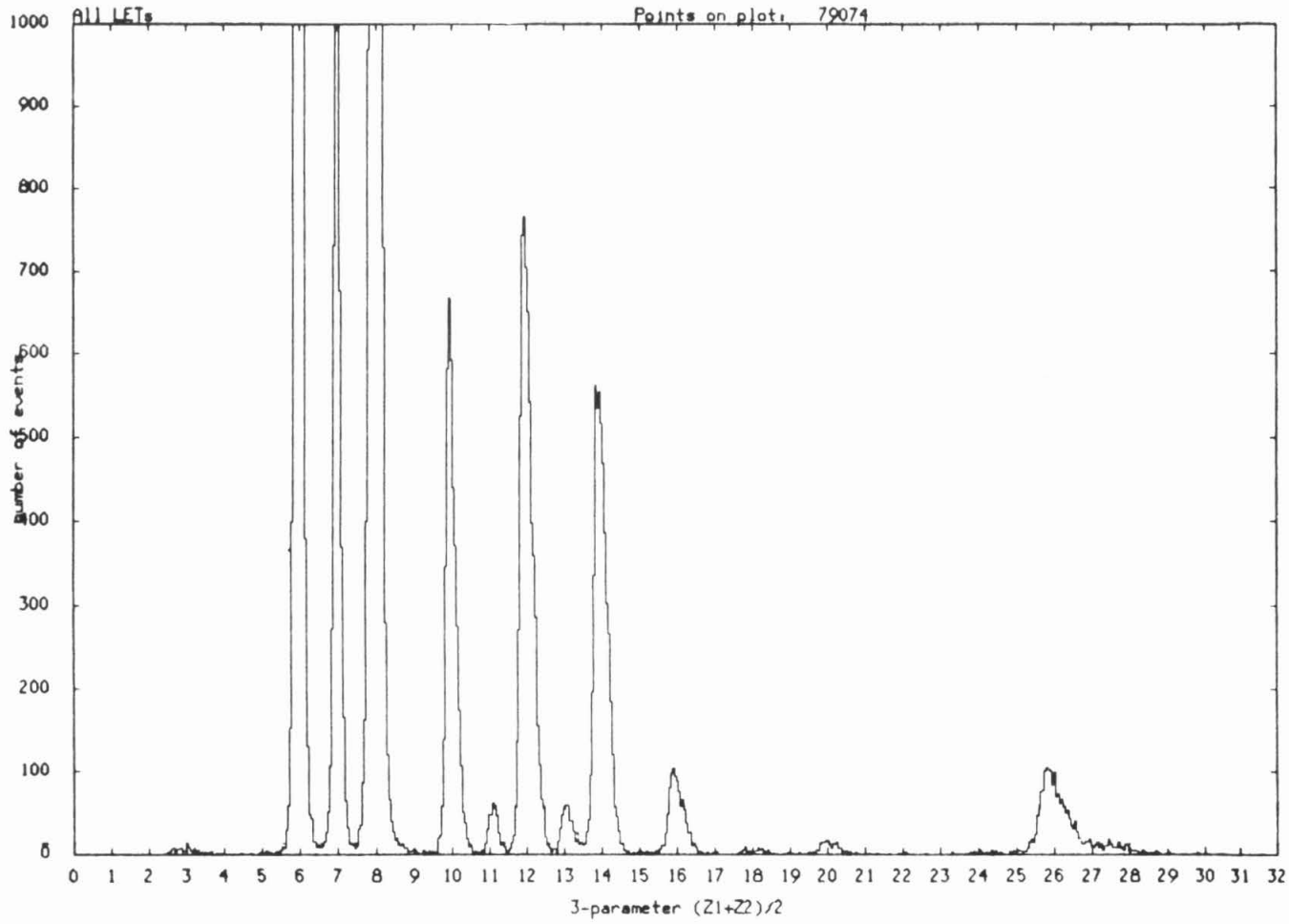

Fig. 3.6. Histogram of <Z> for three-parameter data from all Voyager 1 LETs after imposition of the charge consistency requirement. Note the effective removal of most of the background present in Fig. 3.5, while losing very little of the good data.

These expressions were arrived at by generating ΔZ histograms for each of the abundant elements C, N, O, Ne, Mg, Si, S and Fe, determining the 2σ (95%) width of each peak, and fitting a simple functional form to a plot of this width vs. Z. All of the data from all LET telescopes were combined to obtain the LET ΔZ widths, and similarly for HET. The HET charge consistency requirement is stricter than that for LET on account of the inherently better charge resolution of HET; although in both cases only ~5% of the data is rejected by this requirement, the background is dramatically reduced. These requirements are displayed on representative ΔZ vs. <Z> plots of Voyager 1 LET D and Voyager 2 HET 1 data (Figs. 3.3, 3.4). These charge consistency requirements were relaxed significantly in the region of iron to accommodate clusters of events with anomalously high ΔE. This instrumental effect, known as the "pulse height multiplication effect," is one of several anomalies in the instrument performance that had an impact on the data analysis; all of these problems are discussed in Appendix G.

The dramatic reduction in background level achieved in this way is illustrated in charge histograms of three-parameter data from all of the LETs (Fig. 3.5 and 3.6). Fig. 3.5 shows <Z> without charge consistency imposed, and Fig. 3.6 <Z> after charge consistency has been imposed. The improvement in data quality for the HET telescopes is comparable. The background level in the two-parameter data is comparable to what is seen in the three-parameter data without the charge-consistency requirement. From histograms such as Fig. 3.6, the charge boundaries corresponding to the very-abundant and moderately-abundant elements were defined. These boundaries, which were used to classify nuclei of the abundant elements, are listed in Appendix C; the same set of boundaries were used for all telescopes. The locations of the boundaries are determined by the shapes of the element peaks, their relative heights, and their positions on the charge scale as determined by the charge calibration algorithm, including the offset resulting from the disagreement between the true mass and the assumed dependence of M on Z. The rare elements do not form clear

histogram peaks due to their poor statistics; for these elements a different method (Section 3.6) was used to arrive at the best possible estimate for the number of nuclei observed of each element.

3.3 Energy Interval Selection

The approximate ranges of incident energy covered by LET and HET for all elements with $3 \leq Z \leq 30$ are listed in Appendix D. The energy intervals chosen for use in the analysis for a given element were strongly dependent on the relative abundance of the element. In each case a compromise is required between retaining as much of the data set as is necessary for adequate statistical accuracy, while focusing on that part of the data set where the charge resolution is adequately high and the background level adequately low. In general, these considerations force much tighter restrictions on the rarer elements than on the abundant ones.

The eight most abundant heavy elements (C, N, O, Ne, Mg, Si, S and Fe) are all well-resolved in both the two- and three-parameter data of both LET and HET; background effects are negligible. To obtain abundances relative to Si of the seven other elements in this group, it was desirable to identify a common energy interval covered by the LET/HET for all of these elements. Since the energy range covered by LET/HET shifts toward higher energy as Z increases, fixing the largest possible common energy interval for all eight elements requires discarding some low-energy data for the lighter elements and some high-energy data for the heavier elements. Since the differential energy spectra of flares are steeply decreasing functions of energy, many more data are discarded for the light elements than for the heavy ones, but in no case are the statistics of the data appreciably affected. The common energy interval chosen for these elements was 5.0 - 45.3 MeV/nucleon.

The elements of intermediate abundance (Na, Al, Ar, Ca, Cr) are still clearly resolved in the three-parameter data of both LET and HET, but are poorly

resolved in the two-parameter data of both telescopes on account of higher background contamination. For this reason, only three-parameter data were included in the analysis. The statistics of the resulting data set are much poorer, due both to the comparative rarity of the elements and to the restriction to three-parameter data. For this reason a larger fraction of the available data was retained in the analysis by choosing for each element the largest possible common energy interval with Si, rather than a single common interval for all of the elements. This means that the abundances of these elements are over energy intervals that differ both from each other and from that used with the most abundant elements. However, it is noted in Section 4.1.2 that only for a few flares does the power-law exponent γ of the differential energy spectrum vary significantly with Z, indicating that elemental abundances in most flares are not seriously affected by the choice of energy interval. In addition, the energy dependences seen in individual flares average out to essentially no net energy-dependence to the average SEP abundance. Although the energy ranges for these elements extend up to ~70 MeV/nucleon, the level of contamination by galactic cosmic rays in the data sample used was estimated at ~1% by assuming a GCR flux that is constant in time and counting the number of particles seen during quiet-time periods.

For all the remaining elements, the two-parameter data cannot be used at all; background contamination completely masks the presence of the very rare elements. The three-parameter data from the HETs, while just as background-free as the three-parameter LET data and slightly better in charge resolution, was not used either. Since the energy spectrum of solar particles falls steeply with energy, the energy range of HET corresponding to three-parameter events does not add appreciably to the statistics of the three-parameter LET data. In addition, the background flux of galactic cosmic ray particles is rising in this energy range and becoming comparable to the solar particle flux for the rare elements, which are proportionally more abundant in galactic cosmic rays on account of their production by fragmentation of abundant species while en

route to the solar system. Hence what few rare element three-parameter events are seen by the HETs are significantly contaminated by particles of non-solar origin. Thus only three-parameter LET events were used in the rare element study.

The poor statistics of this already limited data set make it impractical to discard any of the three-parameter LET data, so the energy interval selected for each such element is the full energy range covered by the LET for three-parameter data. Si events were also counted over their full energy range, and a spectral correction was applied to obtain the rare element abundance relative to Si, as described in Section 3.6. The uncertainty inherent in the spectral correction process is small compared to the statistical uncertainty due to the small number of particles.

The energy intervals used in the analysis for each element are listed in Table 3.1.

3.4 Time Period Selection

The time span of the Voyager CRS data set covered by this study begins with the launch of the spacecraft in August and September of 1977 and ends in January of 1983. It excludes four periods of a few weeks' duration each, centered around the Jupiter and Saturn encounters (March 1979 and November 1980 for Voyager 1, July 1979 and August 1981 for Voyager 2). From the remaining time periods, all significant enhancements of heavy ions above the background galactic cosmic-ray flux level were catalogued. Although rate plots were consulted, many small events which were apparent in rate plots of protons contained no appreciable fluxes of heavy ions. The result of the inventory was a catalog of 25 time periods of enhanced heavy charged particle intensity, numbered from 1 to 25 (Appendix E). Most of these were seen by both Voyagers, but a few (e.g., period 14) were not, either because of their proximity to a planetary encounter of one of the spacecraft, or because of the small size of the event

Table 3.1. Incident energy ranges used for each element in the abundance calculation. The energy range shown for Si is applicable for the abundances of the other very abundant elements (C, N, O, Ne, Mg, S, Fe); for the elements of intermediate abundance (Na, Al, Ar, Ca, Cr) the energy interval for Si is the same as that shown for the other element. For the remaining elements, the entire three-parameter LET energy interval for Si was used (7.0 - 23.3 MeV/nucleon) and a spectral correction was performed to correct this to the energy interval used for each particular element.

Z	incident energy (MeV/nucleon)
3	3.2 - 9.2
4	3.8 - 11.1
5	4.4 - 12.9
6	5.0 - 45.3
7	5.0 - 45.3
8	5.0 - 45.3
9	5.8 - 18.0
10	5.0 - 45.3
11	6.9 - 62.1
12	5.0 - 45.3
13	6.9 - 68.4
14	5.0 - 45.3
15	7.0 - 23.7
16	5.0 - 45.3
17	7.3 - 25.1
18	7.7 - 72.8
19	7.7 - 26.7
20	8.0 - 72.8
21	7.7 - 27.4
22	7.8 - 27.7
23	7.8 - 28.0
24	8.1 - 29.0
25	8.1 - 29.3
26	5.0 - 45.3
27	8.3 - 30.4
28	8.7 - 31.7
29	8.5 - 31.3
30	8.6 - 31.9

and the radial and/or azimuthal separation between the spacecraft. Several flares, although present in the data of both spacecraft, are much more intense in one than the other, due to better connection with the source region and/or radial gradient effects. A few of the initially designated periods (2, 11, 15, and 23) were found to include too few PHA events to yield useful abundance figures for even the most abundant elements, and were not considered further.

To reduce the potential for contamination of the smaller flares by particles of non-solar origin, an additional restriction was imposed. All time periods during which the flux of heavy ($Z > 3$) ions was less than a factor of five above the quiet-time level were excluded. The quiet-time rate for two LETs at each spacecraft decreased gradually from about 5×10^{-2} sec^{-1} at the beginning of the mission to about 2.5×10^{-2} at the end of the time span covered by this study. Hence the threshold rate level used here ranged from ~2.5 to ~1.2×10^{-1} sec^{-1}. This eliminated a few of the smallest flares completely and shortened the usable duration of most of the others, but did not appreciably affect the total number of particles in the data set since most of the particles came from high-flux periods. The end result of this survey (Table 3.2) was a list of 22 distinct SEP events which were observed by at least one of the spacecraft, and which provide meaningful statistics on the abundances of at least the seven most abundant heavy elements (C, N, O, Ne, Mg, Si and Fe).

The original time period 1 actually consisted of five closely spaced or partially overlapping flare events, designated 1a through 1e; similarly, flare period 7 consisted of three such closely-spaced flares. Seven of the earliest large flares (1d, 1e, 3, 5, 7a, 7b, 7c) were previously studied using Voyager CRS data, but only the LET telescopes were used (Cook 1981). This study extends the coverage of these flares to include the higher-energy HET data, and also adds several more flares of comparable size and many others up to two orders of magnitude smaller. It can be seen that three closely spaced large flares (7a,b,c) together comprise about half of all the observed solar particles, and that the six largest flares include 90% of the observed SEPs.

Table 3.2. Final set of all SEP event time periods meeting flux threshold restriction (LET heavy ion count rate greater than 5 times the quiet time level).

flare event	V1 time period	V2 time period	peak counting rate[1] V1	V2
1a	1977: 253.7-256.1	1977: 254.0-255.2	0.34	0.29
1b	1977: 256.1-259.6	1977: 256.9-259.4	1.60	0.95
1c	1977: 260.0-262.0	1977: 260.1-261.2	0.62	0.35
1d	1977: 262.6-265.6	1977: 262.6-265.7	14.5	6.3
1e	1977: 267.0-270.7	1977: 267.2-270.7	6.5	10.0
3	1977: 326.9-332.0	1977: 327.1-331.6	4.3	8.2
4	1978: 005.5-006.7	1978: 005.7-007.1	1.2	5.5
5	1978: 045.5-052.1	1978: 045.4-051.9	7.5	9.1
6	1978: 068.5-072.0	1978: 068.9-072.0	0.44	0.53
7a	1978: 111.1-119.0	1978: 110.7-118.8	8.1	7.7
7b	1978: 119.0-121.4	1978: 118.8-121.2	39.	41.
7c	1978: 121.4-130.7	1978: 121.2-130.1	16.	12.5
8	1978: 177.7-181.6	1978: 177.5-180.8	1.2	2.5
9	1978: 197.1-199.3	1978: 195.2-198.4	0.54	0.87
10	1978: 278.1-280.5	1978: 276.7-281.2	0.56	0.44
13	1979: 164.5-167.0	1979: 161.0-166.1	0.55	1.15
16	1979: 237.6-246.1	1979: 235.2-249.5	0.40	0.45
17	1979: 261.7-274.7	1979: 257.9-273.5	5.0	4.6
20	1981: 132.0-144.5	1981: 130.7-141.1	0.36	0.68
22	----------	1981: 301.3-303.8	----	0.18
24	1982: 183.6-187.6	1982: 169.1-174.0	0.44	0.58
25	1983: 000.5-001.9	1982: 355.9-358.3	0.26	0.66

[1] Slant rate (particles/sec) for 2 LETs.

For the seven most abundant heavy elements (C, N, O, Ne, Mg, Si and Fe), event statistics are good enough that relative abundances can be obtained for each of the 22 individual flare periods, as well as for the total flare data set. This allows the determination of both particle-averaged and flare-averaged abundances, which may then be compared. Any systematic differences are important for interpreting the abundances of the very rare elements; the rarity of these elements precludes any type of flare-by-flare abundance calculation, and one is forced to obtain only a single particle-average abundance by summing the data from all flares.

The abundances from individual flares also permit calculation of the magnitude of the flare-to-flare variation in the abundance. This contributes significantly to the uncertainty for the rare elements, and for these it must be estimated based on the variation seen with the common elements.

For several elements of intermediate abundance (Na, Al, Ar, Ca and Cr), statistically meaningful abundances can be obtained for typically only the 10 largest individual flares observed. This permits studies for these elements similar to those just described for the most abundant elements. Ni, although of comparable abundance to these elements, must be treated with the rare elements on account of its poor separation from Fe even in the three-parameter data.

Additional studies possible with the more abundant elements include: comparison of energy spectra shape between different flares; comparison of the shapes of energy spectra for different elements, to obtain information on possible energy-dependence of abundance ratios; studies of the time-dependence of abundance ratios during individual flares; study of possible propagation effects by looking for trends in abundance ratios with flare size and/or distance from the sun at which the flare was seen, or by comparing abundance ratios seen at each of the two spacecraft for the same flare event.

3.5 Abundances of the Abundant Elements

The relative abundances of the more abundant elements were arrived at by counting the number of particles observed in the desired time and energy intervals, subject to the constraints on <Z> and ΔZ described in Section 3.2. This amounts to counting the events inside a trapezoidal "box" in the Z_1 - Z_2 plane. When both LET and HET data were used, they were given unequal weights in the sum, to account for their differing geometry factors and livetimes. This is necessary when calculating the relative abundance of two elements in a common energy interval since the proportion of that energy interval represented by LET or HET depends on Z. The HET/LET livetime ratio is different for each solar flare period used and is dependent on the details of the CRS operation during the time period. The HET/LET geometry factor ratio is derived from the geometry factors in Table 2.2, with appropriate modifications for the time periods when individual telescopes were not functioning. It was also necessary to weight HET 2- and 3-parameter data differently (on account of geometry factor differences) and also occasionally LET 2- and 3-parameter data had to be weighted differently when one of these classes of data could not be used from one or more telescopes. Outside of these considerations, no other weighting was made with respect to Voyager 1 vs. Voyager 2; this means that the contributions of the two spacecraft to the average may be unequal (and variable with time), but no Z-dependent bias is introduced. Equalizing the contribution of the two spacecraft is neither physically reasonable nor practical, since unequal quantity of data collection for the two spacecraft in a given time period can have many causes, both physical and instrumental. The usefulness of the HET data lies mainly in extending the range of incident energy coverage, not in making a major contribution to the statistics of the combined LET/HET data set. The weighting factors for the various data subsets are listed in Appendix F for each of the time periods used in this study. The weighting factor for each data subset is the ratio of the geometry factor-livetime product for 3-parameter LET data from that telescope to the product for the given data set

from the same telescope. Raw event numbers are multiplied by these factors before summing all of the data for a given time period.

3.6 Rare Element Abundances; Maximum Likelihood Method

Even with the restriction to three-parameter LET data, for the rare elements poor statistics, inadequate resolution and background effects make it difficult or impossible to obtain accurate abundances by simply counting events in a particular region of the Z_1 - Z_2 plane. To get the best possible estimate of the true abundances of such elements, a two-dimensional version of the *maximum likelihood method* was used. This technique will now be briefly described.

In applying the maximum likelihood method, one assumes a model distribution to represent the parent population; this model contains one or more free parameters a_i to be optimized. This model probability distribution $p(x;a_i)$ allows one to determine, for each actual data point x_j, the probability $p(x_j;a_i)$ of its having arisen from the assumed parent distribution, given the values of the parameters a_i. The product of such probabilities for all the data points is the probability for the entire data set to have arisen from the assumed model. This probability, referred to as the *likelihood function*

$$L(a_i)=\prod_j p(x_j;a_i) \tag{3.8}$$

is maximized as a function of the a_i to obtain the best fit to the data. Confidence intervals are obtained by calculating the ratio of the likelihood function integrated over particular parameter ranges to the integral over all possible parameter values.

Instead of Z_1 and Z_2, the events were characterized by the other two charge parameters, <Z> and ΔZ, defined by Eqs. (3.4) and (3.5). This transformation essentially amounts to a 45° rotation of the Z_1 - Z_2 plane and arrays the elements horizontally along the <Z> axis.

For elements with Z > 14 the model distribution consists of the sum of three two-dimensional distributions in the <Z>-ΔZ plane, each representing one of the elements being fit; in general these consist of the rare element being studied and two neighboring elements on the charge scale, which are usually of much higher abundance. In general, the neighboring elements used are those expected to be the major contaminants for the element in question; in most cases they are the two immediately adjacent elements. For a few even-Z elements (e.g., Cr, Ni) the nearest-neighboring even-Z elements are used instead, since they are a more significant contaminant, owing to their higher abundance, than are the nearer but much rarer odd-Z immediate neighbors. (For Zn there is no upper neighbor; the LET is not capable of observing elements above Z = 30 over the full energy range, and the elemental abundances drop to undetectable levels beyond Z = 30 in any case. For Zn the two nearest elements below Zn were used as the neighbors). For the remaining cases (Z = 3, 4, 5, 9), where the primary difficulty is with background rather than with contamination by neighboring elements, the model consists of a single peak plus a "flat" background distribution. The parameters to be varied in maximizing the likelihood are the fractions of the total integrated model distribution contributed by each component distribution. All but one of these parameters is free (over the range 0 to 1), since by definition they are constrained so that their sum is unity. After maximizing the likelihood, these parameters give the fractions of the total data sample consisting of each element (or background). The component distributions are normalized to unit integral, so this is true of the composite distribution as well.

To carry out the maximum likelihood calculation for the rare elements, it was first necessary to obtain the best possible model for the expected two-dimensional distribution of events in the region of each rare element. This includes the shape, widths and positions of the peaks corresponding to each element being fit, as well as their neighbors. Since direct examination of the rare element peaks was not possible, the approach used was to characterize the

distributions for the most abundant elements (C, N, O, Ne, Na, Mg, Al, Si, S, Ca and Fe) and linearly interpolate or extrapolate as necessary to obtain estimates for the rarer elements.

The parameters used to characterize the distributions were the median values and widths, in the <Z> and ΔZ coordinates, of the two-dimensional event distribution, together with a "reference distribution" to describe the overall shape of the peak irrespective of its width and position on the charge scale. The reference distribution was derived from the actual distribution of the data for a very abundant element; in most cases oxygen was used as the reference element, although in the higher charge range ($Z > 14$) iron was also used since the iron peak has a qualitatively different shape from the abundant elements lower on the charge scale. The data points for these elements (119,000 events for O, 6700 for Fe) were converted into a two-dimensional 24 x 24 histogram and "smoothed" by cubic interpolation; perspective views of the resulting reference distributions are shown in Figs. 3.7 and 3.8. To produce model distributions for other elements, the reference distribution is scaled by an appropriate scale factor (independently in the two dimensions) and shifted to the appropriate place on the <Z>-ΔZ plane by applying two offset parameters. The scale factors and offset parameters appropriate to the rare elements were obtained by linear interpolation between or extrapolation beyond the values measured for the more abundant elements. The latter values were obtained by carrying out maximum-likelihood fits of the various abundant elements to the reference, with the relative <Z> and ΔZ scale factors and relative offsets as the free parameters in the fit. Because the large number of events (10^3–10^5) in the data set for each abundant element, it was impractical to do these fits on an event-by-event basis, so the data for each element were converted into a two-dimensional 24 x 24 histogram as was done for the reference element itself, and the histogram was fit to the reference distribution.

The <Z> and ΔZ scale factors are shown plotted vs. Z along with their uncertainties in Figs. 3.9 and 3.10 for the oxygen and iron references

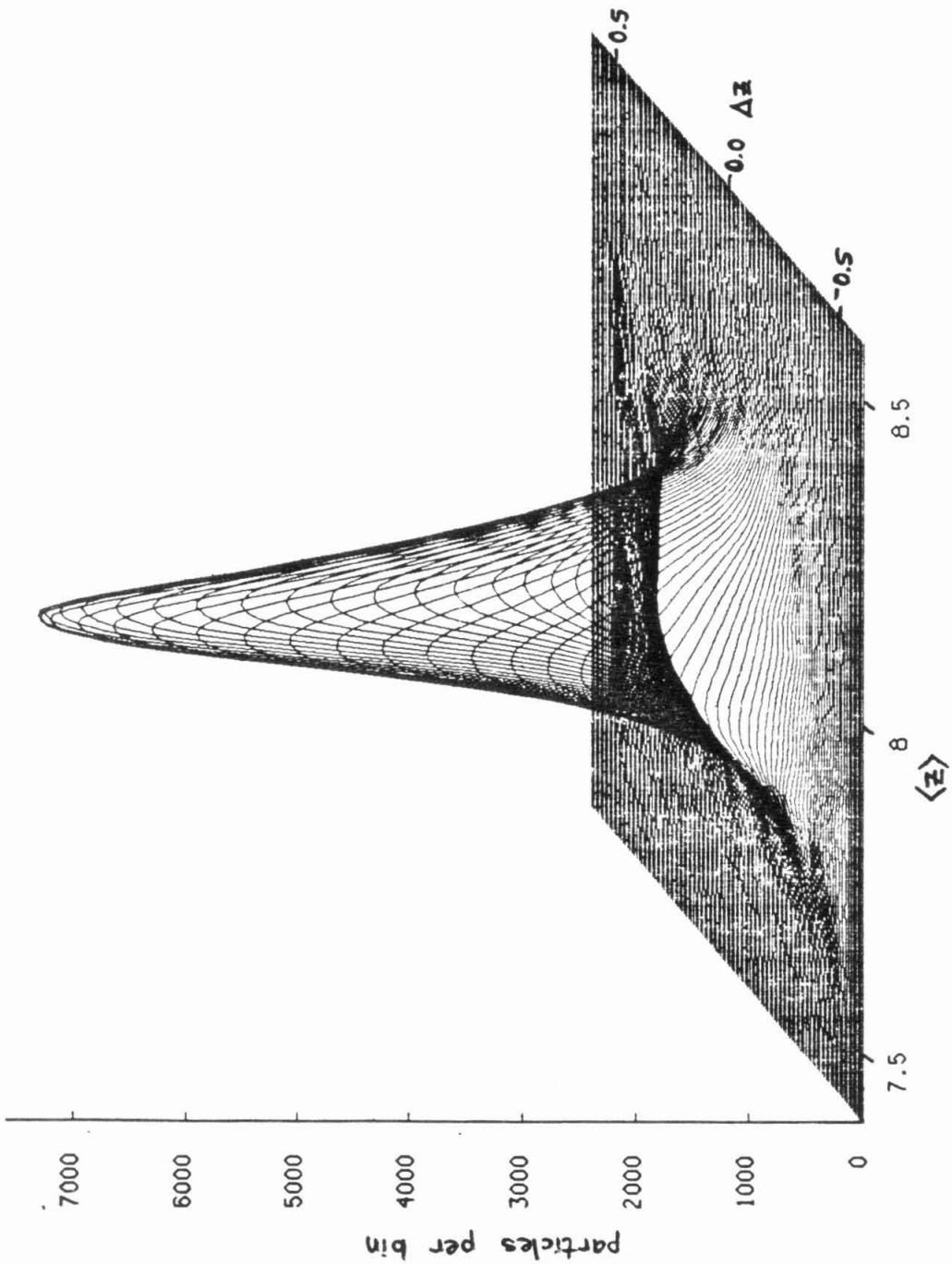

Fig 3.7. Two-dimensional distribution of three-parameter LET oxygen events in <Z>-ΔZ space. This distribution was used as a "reference distribution" in carrying out maximum-likelihood fits for the rare elements, i.e., other element peaks were modeled by applying appropriate scale factors to this distribution. The distribution was generated by smoothing a two-dimensional histogram of 119,000 oxygen events seen by all Voyager LETs during all flare periods combined.

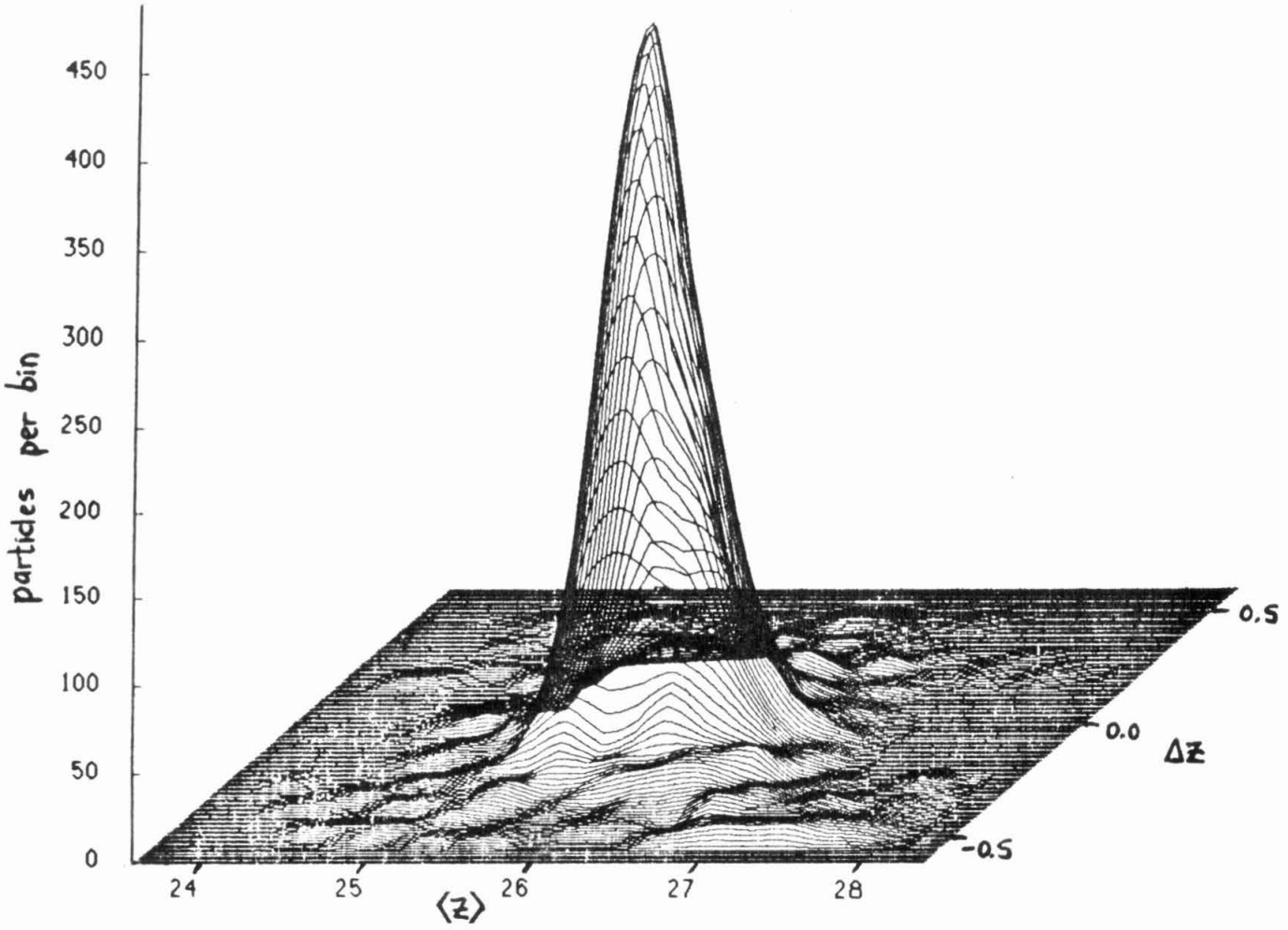

Fig. 3.8. Two-dimensional distribution of three-parameter LET iron events in <Z>-ΔZ space. This distribution was used as a "reference distribution" in carrying out maximum-likelihood fits for the rare elements, i.e., other element peaks were modeled by applying appropriate scale factors to this distribution. The distribution was generated by smoothing a two-dimensional histogram of 6700 iron events seen by all Voyager LETs during all flare periods combined. The bumpiness seen in the tail of the distribution is the result of the small numbers of particles in individual bins.

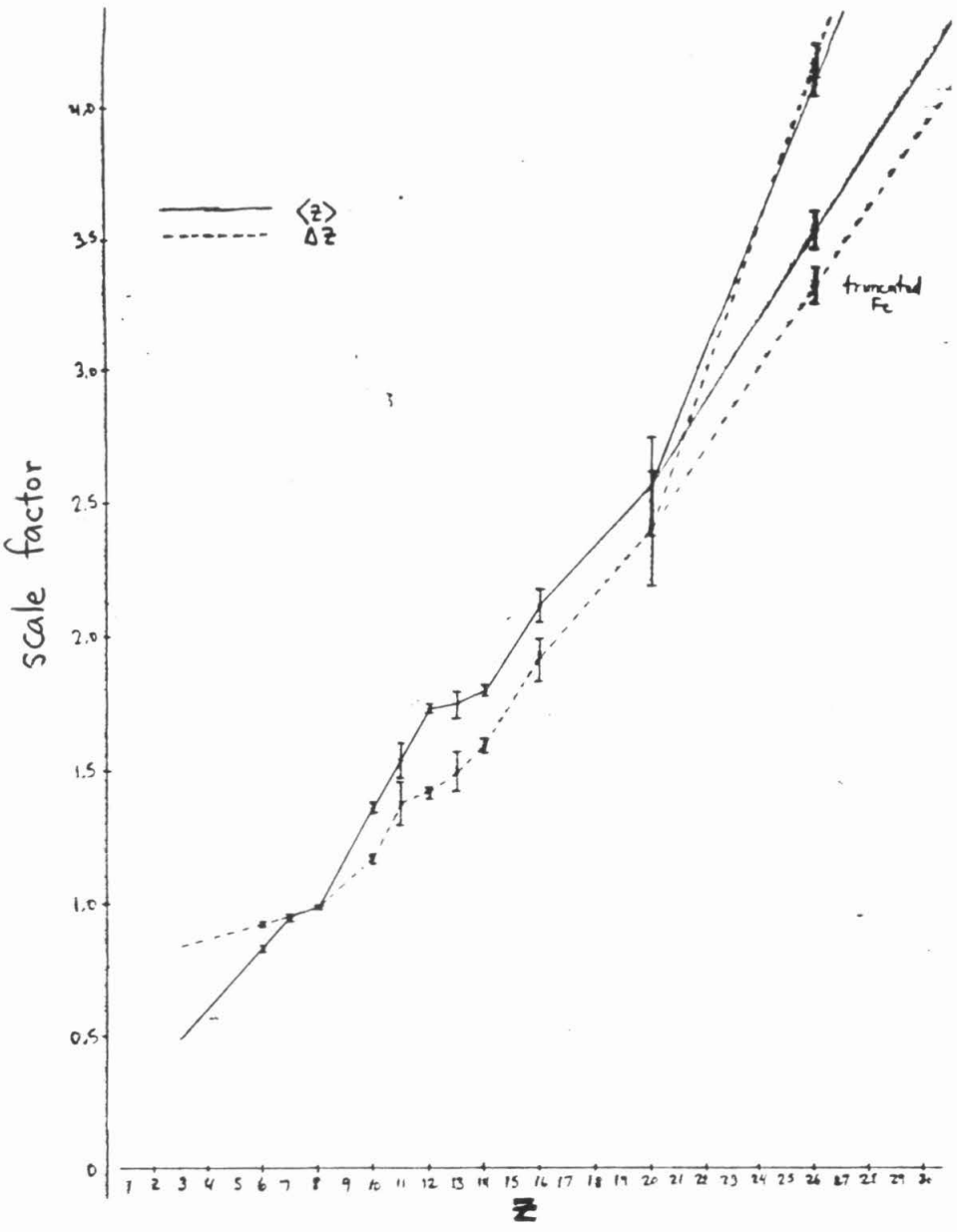

Fig. 3.9. <Z> and ΔZ scale factors applied to the oxygen reference in the maximum likelihood calculations. For the elements C, N, O, Ne, Na, Mg, Al, Si, S, Ca and Fe, the scale factors were obtained by doing maximum likelihood fits between the two-dimensional distribution for the element and the two-dimensional oxygen reference distribution; the error bars are based on the contour of constant likelihood that contains 68.3% of the likelihood, on the assumption that the likelihood function is Gaussian. For all other elements, the scale factors were obtained by interpolation or extrapolation. For Fe, the lower points are the scale factors for the "truncated" Fe distribution used for Mn and Co, while the upper points are the scale factors for the full Fe distribution used in all other cases. Theoretically, one expects the width to be proportional to Z to first order, since $dE/dx \propto Z^2$; the deviations are accounted for by the uncertainty of the fit, instrumental effects, the charge calculation algorithm and the presence of multiple isotopes for some elements.

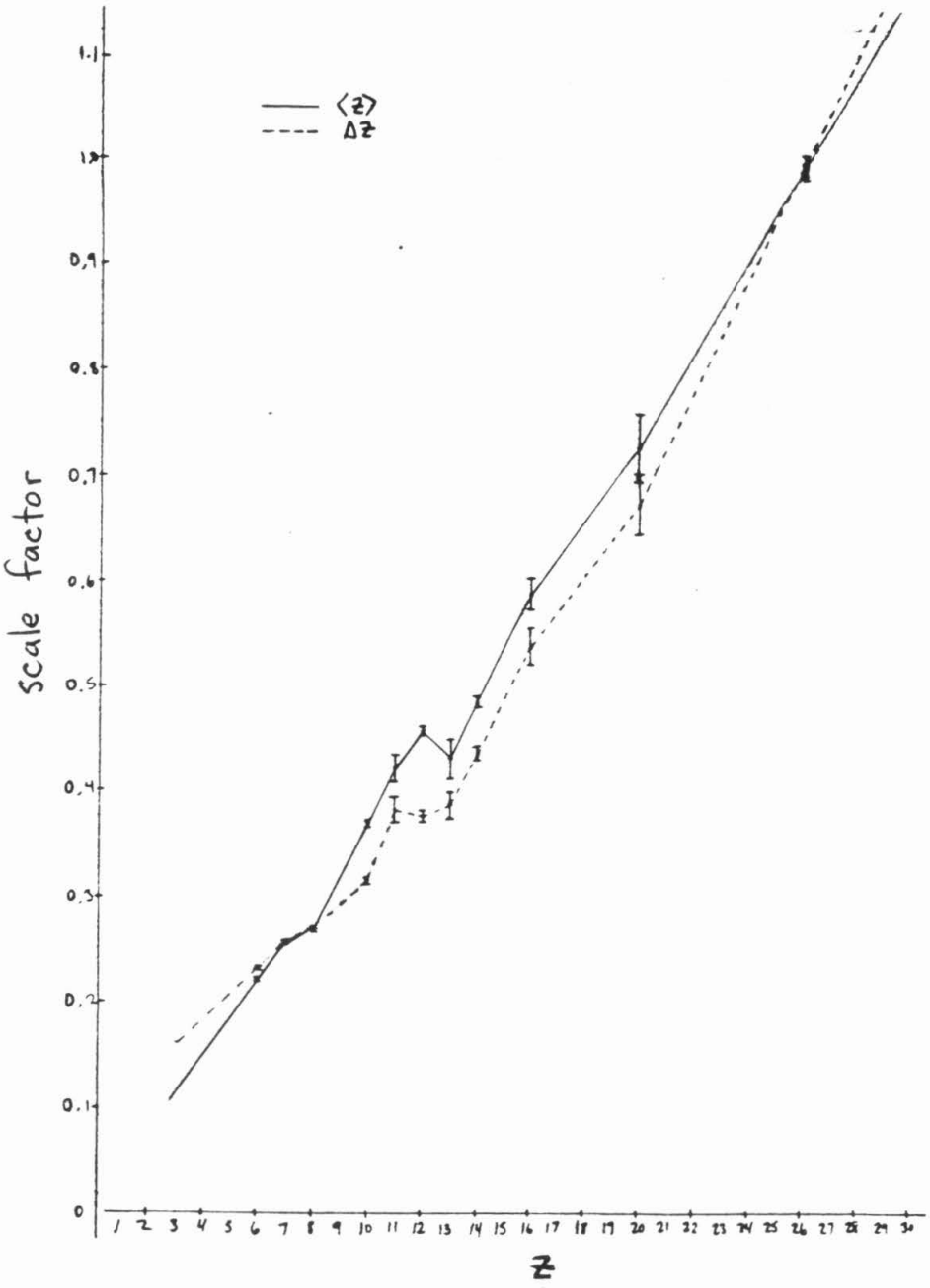

Fig. 3.10. <Z> and ΔZ scale factors applied to the iron reference in the maximum likelihood calculations. For the elements C, N, O, Ne, Na, Mg, Al, Si, S, Ca and Fe, the scale factors were obtained by doing maximum likelihood fits between the two-dimensional distribution for the element and the two-dimensional iron reference distribution; the error bars are based on the contour of constant likelihood that contains 68.3% of the likelihood, on the assumption that the likelihood function is Gaussian. For all other elements, the scale factors were obtained by interpolation or extrapolation.

respectively. One expects these curves to be smooth and linear with Z to first order; since $dE/dx \propto Z^2$, the deviations in Z resulting from fluctuations in ΔE should be proportional to Z. The discrepancies can be accounted for by a combination of statistical uncertainty, instrumental problems such as the pulse height multiplication effect, systematic effects resulting from the charge calculation algorithm, and the presence of multiple isotopes for some elements.

The measured or interpolated peak widths for the various elements were used to scale the reference distribution to the width appropriate to the particular elements being fitted. The position of each scaled copy of the reference distribution was set using the measured or interpolated peak medians. There was an additional correction to the peak position along the <Z> axis to account for the dominant isotope mass of the element being unequal to the value M(Z) assumed by the charge calculation routine. By using the power-law approximation for the range energy relation,

$$R = \frac{k M}{Z^2}\left(\frac{E}{M}\right)^{\alpha} \tag{3.9}$$

the correction Δ is found to be

$$\Delta = Z_c - Z_0 = Z_0\left[\left(1 + \frac{\Delta M}{f Z_0}\right)^{\frac{\alpha-1}{\alpha+1}} - 1\right] \tag{3.10}$$

where Z_0 is the true, integer value of Z, Z_c the value generated by the charge calculation algorithm, f the proportionality between charge and mass assumed by the algorithm ($M = f Z$, see Eq. 3.3); ΔM the difference between the true mass M and $f Z$; and α the exponent in the range-energy relation. Because the range-energy relation is not a strict power-law, the charge shift for a given element is significantly energy-dependent. To estimate the mean shift for each element, a composite energy spectrum for Si was generated by combining the data from all flares. This yielded a mean energy for Si in the energy range used for this element. With the assumption that the composite energy spectra of

Table 3.3. <Z> and ΔZ scale factors and offsets used with the oxygen reference distribution in maximum-likelihood abundance calculations for the rare elements in the charge range $3 \leq Z \leq 30$. These parameters are used to scale the width of the reference distribution in the two dimensions and to position it in the proper place on the <Z>-ΔZ plane for the element being modeled. Values for C, N, O, Ne, Na, Mg, Al, Si, S, Ca and Fe are determined by maximum-likelihood fits of these elements to oxygen; all others are obtained by interpolation or extrapolation. The value obtained for oxygen itself (0.9906) is indicative of a systematic error of ~1% produced by the maximum-likelihood algorithm in fitting a two-dimensional histogram to a smooth distribution.

Z	<Z> scale	ΔZ scale	<Z> offset	ΔZ offset
3	0.4797	0.8469	+0.0744	+0.0065
4	0.5963	0.8721	+0.0876	+0.0052
5	0.7129	0.8973	+0.0727	+0.0039
6	0.8295 ± 0.0028	0.9225 ± 0.0025	-0.0081 ± 0.0006	+0.0026 ± 0.0007
7	0.9461 ± 0.0069	0.9477 ± 0.0080	-0.0016 ± 0.0008	+0.0013 ± 0.0009
8	0.9906 ± 0.0006	0.9883 ± 0.0026	-0.0007 ± 0.0005	-0.0003 ± 0.0006
9	1.1743	1.0768	+0.0998	+0.0054
10	1.3580 ± 0.0179	1.1652 ± 0.0186	+0.0211 ± 0.0022	+0.0111 ± 0.0025
11	1.5343 ± 0.0645	1.3743 ± 0.0808	+0.1390 ± 0.0058	+0.0182 ± 0.0091
12	1.7232 ± 0.0196	1.4091 ± 0.0191	+0.0349 ± 0.0024	+0.0176 ± 0.0027
13	1.7397 ± 0.0520	1.4891 ± 0.0719	+0.1055 ± 0.0080	+0.0301 ± 0.0094
14	1.7901 ± 0.0179	1.5864 ± 0.0250	+0.0093 ± 0.0016	+0.0161 ± 0.0030
15	1.9478	1.7468	+0.0893	+0.0090
16	2.1056 ± 0.0604	1.9072 ± 0.0828	+0.0102 ± 0.0062	+0.0019 ± 0.0094
17	2.2174	2.0287	+0.1346	-0.0084
18	2.3291	2.1502	+0.0427	-0.0187
19	2.4408	2.2716	+0.1157	-0.0290
20	2.5526 ± 0.1815	2.3931 ± 0.2094	+0.0381 ± 0.0158	-0.0393 ± 0.0231
21	2.8084	2.6896	+0.0409	-0.0310
22	3.0642	2.9862	+0.0919	-0.0226
23	3.3200	3.2828	+0.1486	-0.0143
24	3.5759	3.5793	+0.0692	-0.0060
25	3.8317	3.8758	+0.1167	+0.0024
26	4.0875 ± 0.0472	4.1724 ± 0.0691	+0.0296 ± 0.0093	+0.0107 ± 0.0118
27	4.3433	4.4690	+0.0857	+0.0190
28	4.5991	4.7655	-0.0744	+0.0274
29	4.8550	5.0620	+0.0945	+0.0357
30	5.1108	5.3586	+0.0701	+0.0440

Table 3.4. <Z> and ΔZ scale factors and offsets used with the iron reference distribution in maximum-likelihood abundance calculations for the rare elements in the charge range $3 \leq Z \leq 30$. These parameters are used to scale the width of the reference distribution in the two dimensions and to position it in the proper place on the <Z>-ΔZ plane for the element being modeled. Values for C, N, O, Ne, Na, Mg, Al, Si, S, Ca and Fe are determined by maximum-likelihood fits of these elements to iron; all others are obtained by interpolation or extrapolation. The value obtained for iron itself (0.9906) suggests a systematic error of ~1% produced by the maximum-likelihood algorithm in fitting a two-dimensional histogram to a smooth distribution.

Z	<Z> scale	ΔZ scale	<Z> offset	ΔZ offset
3	0.1125	0.1599	+0.0771	+0.0085
4	0.1488	0.1843	+0.0893	+0.0047
5	0.1851	0.2087	+0.0734	+0.0009
6	0.2214 ± 0.0004	0.2331 ± 0.0008	-0.0085 ± 0.0005	-0.0029 ± 0.0005
7	0.2577 ± 0.0015	0.2575 ± 0.0016	-0.0030 ± 0.0011	-0.0067 ± 0.0010
8	0.2690 ± 0.0006	0.2699 ± 0.0005	+0.0003 ± 0.0004	-0.0086 ± 0.0005
9	0.3188	0.2920	+0.0985	-0.0038
10	0.3686 ± 0.0036	0.3140 ± 0.0026	+0.0174 ± 0.0018	+0.0010 ± 0.0020
11	0.4211 ± 0.0124	0.3816 ± 0.0117	+0.1310 ± 0.0129	+0.0090 ± 0.0072
12	0.4565 ± 0.0043	0.3749 ± 0.0049	+0.0266 ± 0.0022	+0.0039 ± 0.0023
13	0.4300 ± 0.0190	0.3865 ± 0.0127	+0.0986 ± 0.0075	+0.0170 ± 0.0098
14	0.4845 ± 0.0054	0.4345 ± 0.0051	+0.0007 ± 0.0027	+0.0039 ± 0.0039
15	0.5358	0.4854	+0.0864	-0.0058
16	0.5870 ± 0.0137	0.5363 ± 0.0177	+0.0129 ± 0.0072	-0.0154 ± 0.0097
17	0.6215	0.5700	+0.1355	-0.0294
18	0.6560	0.6036	+0.0417	-0.0434
19	0.6904	0.6373	+0.1127	-0.0574
20	0.7249 ± 0.0320	0.6710 ± 0.0288	+0.0333 ± 0.0159	-0.0714 ± 0.0190
21	0.7692	0.7246	+0.0317	-0.0594
22	0.8135	0.7782	+0.0783	-0.0474
23	0.8578	0.8318	+0.1307	-0.0354
24	0.9020	0.8855	+0.0470	-0.0233
25	0.9463	0.9391	+0.0900	-0.0113
26	0.9906 ± 0.0115	0.9927 ± 0.0093	-0.0014 ± 0.0063	+0.0007 ± 0.0071
27	1.0349	1.0463	+0.0503	+0.0127
28	1.0792	1.0999	-0.1142	+0.0247
29	1.1234	1.1536	+0.0503	+0.0368
30	1.1677	1.2072	+0.0216	+0.0488

other elements would be similar in shape, a mean energy for each element could be calculated. Using the range-energy tables of Northcliffe and Schilling (1970) for nuclei stopping in aluminum as an approximation to silicon, the power-law exponent at the mean energy could be evaluated. Its value ranged from about 1.6 at Li to 1.3 at Zn. With α determined, the average <Z> shift could be calculated using Eq. 3.10. The "true" mass M was taken to be the average of the nuclear masses of the naturally occurring isotopes, weighted according to their solar-system abundances as given by Cameron (1982). No other corrections were made for the presence of multiple isotopes of elements, e.g., no elements were modeled with multiple overlapping distributions corresponding to various isotopes. Table 3.3 lists the scaling and offset parameters used for all elements in the maximum-likelihood calculations, relative to the oxygen reference distribution; Table 3.4 is the corresponding parameters for the iron reference distribution. Table 3.5 includes the mean incident energies and range-energy exponents used in the calculation of the <Z> offset for each element.

On account of their location deep in the tail of the iron distribution, the elements Mn and Co required a modified procedure. The iron reference distribution used for other elements at the high end of the charge scale could not be used here, since this distribution by necessity contains the data to be fit. On the other hand, the oxygen distribution gives a poor fit to the actual distribution for elements in the vicinity of iron; this was the reason for adopting the iron reference for these cases in the first place. Specifically, the iron distribution has more pronounced tails than the oxygen, so a fit to oxygen of the entire iron distribution yields a poor fit and a scale factor that is inappropriately large for the central portion of the iron distribution. This effect is not very important in cases where the element peaks are reasonably well-resolved, as evidenced by the usually good agreement between abundances derived for a given element using the two different reference distributions, but it is very important for unresolved cases like Mn and Co. The resolution of this dilemma was to use

Table 3.5. Several parameters calculated from the minimum and maximum incident energies of 3-parameter LET events (Appendix D). These include the mean energy <E> (weighted according to the Si differential energy spectrum); the power-law exponent $\alpha_{<E>}$ of the range-energy relation at the mean energy (obtained by interpolation in the tables of Northcliffe and Schilling (1970)); and the spectral correction factor C (obtained by analytic integration of Eq. 3.14 between the energy limits).

Z	<E>	$\alpha_{<E>}$	C
3	4.34	1.615	0.420
4	5.17	1.596	0.473
5	5.98	1.587	0.543
6	6.81	1.579	0.623
7	7.36	1.569	0.686
8	7.79	1.552	0.734
9	7.94	1.515	0.751
10	8.50	1.501	0.827
11	8.53	1.482	0.822
12	9.08	1.477	0.908
13	9.23	1.462	0.929
14	9.65	1.455	1.000
15	9.67	1.438	0.998
16	10.22	1.434	1.103
17	10.10	1.416	1.073
18	10.65	1.413	1.186
19	10.66	1.399	1.185
20	11.08	1.394	1.274
21	10.69	1.373	1.182
22	10.82	1.363	1.211
23	10.83	1.352	1.211
24	11.25	1.349	1.304
25	11.26	1.338	1.302
26	11.67	1.337	1.403
27	11.55	1.324	1.366
28	12.10	1.326	1.508
29	11.83	1.312	1.435
30	11.98	1.306	1.471

the oxygen reference, not scaled according to the full iron distribution, but scaled according to only the central part of the iron distribution, without the tails. This core is the only part that contributes to the set of events which are fit for the elements Mn and Co, on account of their comparatively poor statistics, so this gives reasonable values for Mn/Fe and Co/Fe.

The set of events to be fit in each case were taken to be those within an ellipse centered at the <Z> and ΔZ medians for the rare element. The ellipse has minor and major axes in roughly the same proportion as the <Z> width to ΔZ width for the rare element, and is of such size as to contain, for practical reasons, no more than about 1000 events, but no larger than necessary to include ~95% of the actual rare element events. Only for the elements Mn and Co, on account of their large overlap with the peak of very-abundant Fe, was the 95% level not achievable due to the 1000-event restriction; in these cases about 75% of the rare element was included. For all elements above fluorine, the ellipses contain a significant part of the tails of the distributions of the neighboring elements. Fig. 3.11 shows a scatterplot of events in the <Z>-ΔZ plane in the neighborhood of a rare element, with typical event inclusion ellipses indicated.

For each element, approximately ten different runs were made, varying the size and shape of the inclusion ellipse in increments of 7 or 14% from the averages stated above, thereby changing by about a factor of two the number of events participating in the fit. This was to test the sensitivity of the method to the choice of events being fit. Also, a systematic trend in the best estimate of the rare element abundance with size of the fitting sample would be symptomatic of a poor model. In practice, the spread of values obtained from these multiple runs was well within the uncertainty in the value of any one run, and therefore does not represent a significant systematic error.

Once the best estimate of the number of rare element events within the ellipse has been determined, it is corrected to account for the expected

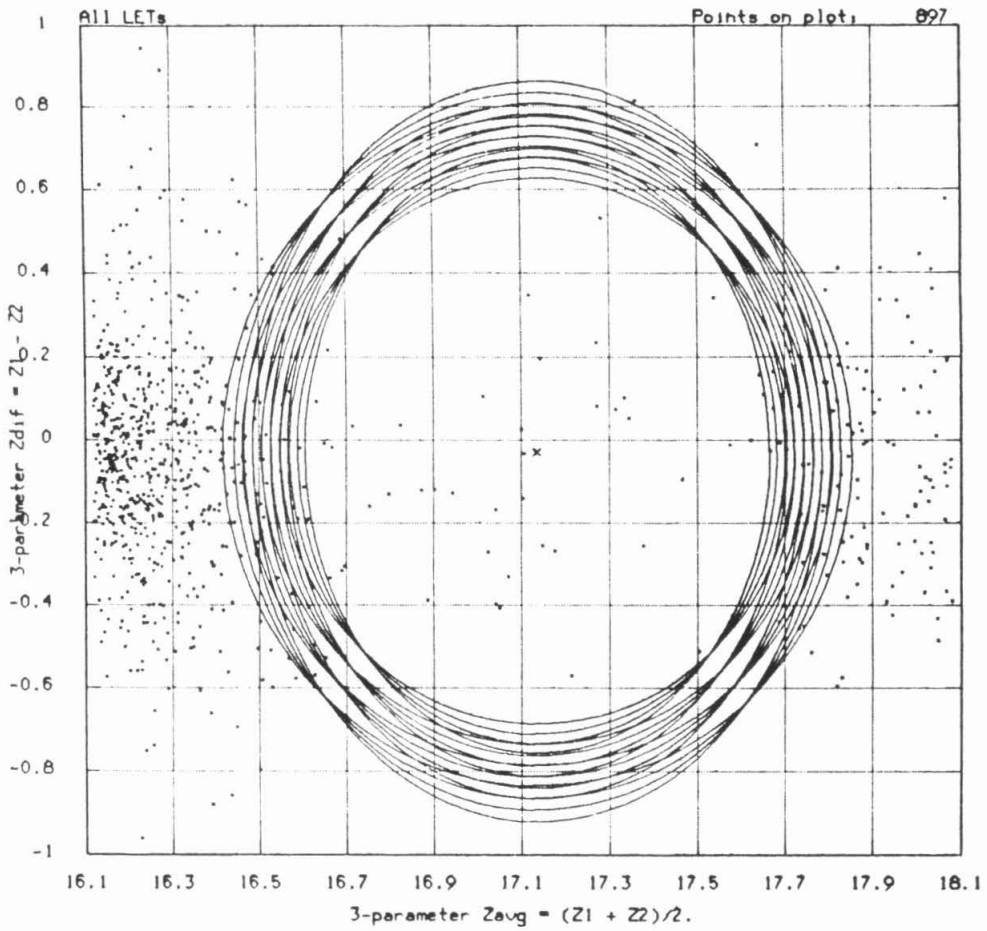

Fig. 3.11. Scatterplot of <Z> vs. ΔZ in the region of chlorine, showing the location of the Cl peak and its overlap with the peaks of its more abundant neighbors S and Ar. Also shown are typical ellipses for defining the set of events to be fit, and the predicted center of the Cl peak. The plot includes all Voyager LET 3-parameter data in this region of the charge scale.

fraction of the total rare element distribution that is not contained within the ellipse used. This is found by dividing the numerically-integrated distribution within the ellipse by the integral over all <Z>-ΔZ space. As indicated above, this number is typically 0.95 except for Mn and Co, for which it is about 0.75.

As mentioned above, the ideal method of error estimation when using the maximum likelihood method is to integrate the likelihood function over appropriate parameter ranges to obtain confidence intervals. However, this proved to be impractical due to the excessive amount of computer time required to evaluate the likelihood function at the high number of points necessary in order to get an accurate numerical integral, particularly for the cases involving two free parameters and hence a two-dimensional integral. The alternative method used, for these cases, was to define the two-dimensional 1σ error box as that contour of constant likelihood which contains 68.3% of the likelihood, with the assumption that the likelihood function can be approximated as a two-dimensional Gaussian function, i.e.,

$$f(x,y) = \frac{1}{2\pi\sigma^2} e^{-(x^2+y^2)/2\sigma^2} \tag{3.11}$$

Expressed in polar coordinates the required condition is

$$\int_0^{r_0} e^{-r^2/2\sigma^2} r\,dr = 0.683 \tag{3.12}$$

for which the solution is

$$r_0 = 1.515\sigma, \qquad r_0^2/2\sigma^2 = 1.148 \tag{3.13}$$

Hence the required contour is that for which ln(L) is 1.148 less than the maximum value. For the cases with only one free parameter, a one-dimensional Gaussian function was assumed as the shape for L, fixing the upper and lower 1σ limits at the points where ln(L) is 0.5 less than its peak value. Although this method is not equivalent to the integration method, it gave reasonably close

error estimates in test cases involving clearly resolved peaks (samples of the CNO data) for which the errors were also calculated by applying Poisson statistics to the known number of events in each peak (since the peaks were clearly resolved, the only uncertainty in the abundance of each element is the statistical uncertainty in the number of events in that peak).

When runs fitting a given element using the two different reference distributions were compared, it was found that the estimated rare element abundance was usually somewhat higher (typically by about 20%) for the iron reference than for the oxygen reference, but this is within other sources of error in the abundance determination, and the difference tends to be larger for the rarer elements. The goodness of fit, as measured by the magnitude of the maximum likelihood per event, was higher with the oxygen reference for all elements except those close to iron on the charge scale; this criterion was used to decide which of the two cases to accept as the best abundance measurement for a given element. Since the oxygen and iron reference distributions, which represented nearly the greatest difference in peak shape observable in the LET data, did not produce substantial differences in the maximum-likelihood solution, one could conclude that the method is relatively insensitive to the details of the peak shape and that the assumption of this model, that all element peaks have the same shape as the reference distribution apart from scale factors, is acceptable. Likewise, the model also assumes that the scaling and offset parameters vary in a predictable way as a function of Z, although instrumental effects and the nature of the charge calculation algorithm introduce small systematic effects. But multiple fits of the same element using slightly different scale factors and offsets show that the method is also not very sensitive to reasonably small variations in these parameters (i.e., on the order of the uncertainty in their determination).

As was noted in Section 3.3, to get the highest statistical accuracy for the rare elements, essentially all three-parameter events seen by the LETs during the flare periods were included. Since this means a different energy interval for

Table 3.6. Results of typical maximum likelihood runs for each of the rare and/or poorly resolved elements. The best-fit event counts for the rare element are combined with the spectral correction factor C (Table 3.5), the integral correction factor I, and the total number of LET 3-parameter Si (13733) to yield the abundance relative to Si. "BG" denotes an assumed uniform background distribution. The uncertainties are derived from that contour of constant likelihood which contains 68.3% of the likelihood. For elements where both the oxygen and iron reference distributions were used, sample runs for both are included for comparison purposes, although only one was used in the final abundance determination. In all cases the run shown is the one that fell closest to the average of the ~10 runs done for each element and reference distribution; it is this run that was used for the final abundance determination.

Z	other elements in fit	ref. distr.	total events fit	best-fit event totals Z	other elements		I	Z/Si (Si = 1000)
3	BG	O	121	32.0	89.0	----	1.028	< 1.25
4	BG	O	8	1.9	6.1	----	1.005	< 0.16
5	BG	O	22	4.3	17.7	----	1.028	< 0.32
9	BG	O	33	5.1	27.9	----	1.045	$0.27^{+0.27}_{-0.24}$
15	14,16	O	94	60.5	10.0	23.5	1.045	$4.58^{+0.59}_{-0.65}$
		Fe	101	70.2	11.1	19.7	1.092	$5.56^{+0.59}_{-0.66}$
17	16,18	O	43	23.2	12.4	7.4	1.058	$1.92^{+0.50}_{-0.52}$
		Fe	58	26.9	19.0	12.1	1.095	$2.31^{+0.57}_{-0.56}$
18	17,19	O	222	217.9	1.0	3.1	1.045	$19.7^{+1.4}_{-1.3}$
19	18,20	O	115	31.2	13.3	70.5	1.045	$2.82^{+0.73}_{-0.72}$
		Fe	133	31.7	15.4	85.9	1.082	$2.97^{+0.76}_{-0.74}$
21	20,22	O	92	2.2	84.6	5.2	1.035	< 0.57
		Fe	70	3.3	62.4	4.3	1.088	$0.31^{+0.33}_{-0.24}$
22	20,24	O	44	37.4	2.9	3.7	1.009	$3.31^{+0.63}_{-0.54}$
		Fe	49	40.7	3.8	4.5	1.022	$3.67^{+0.66}_{-0.57}$
23	22,24	O	88	3.5	9.1	75.4	1.045	$0.32^{+0.44}_{-0.29}$
		Fe	75	4.3	7.9	62.8	1.075	$0.41^{+0.48}_{-0.37}$
24	25,26	O	216	136.5	39.3	40.2	1.029	$13.3^{+1.1}_{-1.2}$
		Fe	241	139.6	4.9	96.5	1.035	$13.8^{+1.2}_{-1.2}$
25	24,26	O[1]	854	42.	2.	810.	1.168	$4.8^{+1.9}_{-1.3}$
27	26,28	O[1]	650	74.	472.	104.	1.200	< 11.9
28	26,27	O	653	293.	292.	67.	1.045	33.7 ± 2.9
		Fe	456	273.	116.	67.	1.073	32.2 ± 2.3
29	28,30	O	146	2.5	137.5	6.0	1.057	$0.29^{+0.79}_{-0.29}$
		Fe	179	3.5	169.5	6.0	1.056	$0.38^{+0.56}_{-0.38}$
30	28,29	O	15	8.8	3.8	2.4	1.056	$1.00^{+0.37}_{-0.40}$
		Fe	27	9.2	15.1	2.7	1.055	$1.04^{+0.47}_{-0.42}$

[1] Oxygen reference scaled to core region only of iron-region elements, rather than to full iron distribution.

each element, a spectral correction is necessary in order to normalize the abundances to silicon. This was done by generating a composite differential energy spectrum for Si, combining the data for all the flares. This spectrum was fit to the functional form

$$\frac{dJ}{dE} = j_0 E e^{-k\sqrt{E}} \tag{3.14}$$

with j_0 and k as free parameters. This functional form, a simplified version of a form used by Gloeckler et al. (1981), fits the data very well over the entire energy range, which is not possible using a power-law form. A best-fit value of k = 2.31 ± 0.01 was obtained for both spacecraft. (This value is in reasonable agreement with Gloeckler et al., who obtained values of k between 1.7 and 9.4 for ten individual flares with an average value of 3.2; their flare sample consists mainly of events smaller than those considered here. Also, their fits include an additional rigidity-dependent parameter which has been set equal to a constant here.) Eq. 3.14 was analytically integrated over the different energy intervals of silicon and the rare elements to produce the required spectral correction factors. Although the three-parameter LET coverage of elements above Si extends to higher energies than Si, this does not require extrapolation of the Si spectrum beyond the data, because the Si spectrum includes higher-energy data from HET. Although inclusion of two-parameter LET data for Si similarly eliminates the need for extrapolation of the spectrum at the low-energy end for B and F, some extrapolation is still necessary for Li and Be. The spectral correction factors used are listed in Table 3.5.

With this procedure the assumption is being made that the composite energy spectrum for the rare elements would be reasonably similar in shape to that of Si. This assumption is justifiable on the grounds that when similar spectra for the other seven abundant elements (C, N, O, Ne, Mg, S and Fe) were generated and fit with the same functional form, the best-fit values of k were within 0.2 of the value for Si, and four of the seven were within 0.1. It can be

shown that a change in k of 0.2 corresponds to a change of 6% or less in the spectral correction factor for all elements except Li, for which the change is 20%. (The value of j_0 is irrelevant since it cancels out of the spectral correction factor.) For all elements these worst-case shifts are small compared to the other sources of uncertainty in the abundance determination.

The results of typical maximum likelihood runs for each element are listed in Table 3.6. Except for one of the two examples included for some elements, which corresponds to the alternate reference distribution and which is shown for comparison purposes only, these cases are those used for the final abundance determinations for the rare elements; for each element it is that case that yields an abundance closest to the average of the ~9 cases run for each element and reference distribution.

Chapter 4

Observational Results

4.1 Introduction

4.1.1 Overview and Observational Strategy

We shall assume a model for SEP production in which coronal material is accelerated by shock waves which originate at the flare site and propagate through the corona. The particles are assumed *not* to be accelerated from the photosphere, although this is the site of the flare itself; the corona is assumed to have been formed from the photosphere by a separate process not associated with the flare (see, e.g., Geiss and Bochsler 1984). The accelerated particles are subsequently propagated through interplanetary space and form the SEPs we observe. There is substantial evidence supporting this model in observations of time-variation of SEP abundances during individual flares (Mason et al. 1984). In addition, SEP ionic charge state measurements (Gloeckler et al. 1981, Luhn et al. 1984) reveal ionization states characteristic of coronal, not photospheric, temperatures, and the SEP elemental composition (e.g., Cook et al. 1984) is consistent with spectroscopic coronal measurements and has distinct differences from the spectroscopic composition of the photosphere.

Since our objective is to use the SEP observations to obtain the best possible estimate of the true solar composition, it is necessary to consider the factors that may account for fractionation of the SEP abundances as compared to those of the solar photosphere. Based on the above model, we may express the observed flux of a given element at a given energy as

$$j(Z,\beta) = f_c(I_Z)\, f_a(\beta,(Q/M)_Z)\, f_p(\beta,(Q/M)_Z,r,\vartheta,\varphi,t)\, A_{ph}(Z) \qquad (4.1)$$

where $A_{ph}(Z)$ is the true photospheric abundance of element Z, f_c is the fractionation of the photospheric material during formation of the corona, f_a is the

fractionation of coronal material during acceleration to SEP energies and injection into the interplanetary medium, and f_p is the fractionation of SEPs during interplanetary propagation. Each of these fractionation factors will be discussed in detail below. The true abundance of a given element relative to silicon can then be expressed as

$$\frac{A_{ph}(Z)}{A_{ph}(Si)} = \frac{f_c(I_{Si})}{f_c(I_Z)} \frac{f_a(\beta,(Q/M)_{Si})}{f_a(\beta,(Q/M)_Z)} \frac{f_p(\beta,(Q/M)_{Si},\gamma,r,\vartheta,\varphi,t)}{f_p(\beta,(Q/M)_Z,\gamma,r,\vartheta,\varphi,t)} \frac{j(Z)}{j(Si)} \qquad (4.2)$$

Using the experimental SEP data one seeks to deduce or infer the dependence of the fractionation factors on the various parameters, to demonstrate through observational and/or theoretical arguments that particular dependencies are not important, and to select the data in such a way as to minimize or eliminate certain dependencies, so as to allow one to apply the appropriate corrections to the observed abundances and arrive at true solar abundances. Previous research, for example, has minimized the dependence on the particle velocity β by choosing common intervals of energy per nucleon, an approach generally retained here as well.

It had been previously noted (Cook et al. 1979, 1984) that the fractionation of SEPs could be separated into two components. One component, a combination of f_a and f_p, was variable in magnitude from flare to flare but in a given flare could be described as a roughly monotonic function of Z. The other component, f_c, was an overall fractionation with respect to the photosphere and had a step-function dependence on first ionization potential (FIP). Specifically, elements with high FIP (> 10 eV) were found to be depleted in SEPs by a factor of ~4, while for low-FIP elements the two abundance determinations are approximately equal. An ordering of SEP abundances relative to the photosphere by FIP has been noted by others as well (Hovestadt 1974; Webber 1975; McGuire et al. 1979; Meyer 1981, 1985), all based on data for only the most abundant elements. A similar ordering is also seen in the composition of galactic cosmic rays relative to solar system composition (Casse et al. 1978). In the case of

SEPs, this pattern suggests a characteristic temperature $\sim 10^4$ °K, for which kT is comparable to a few eV. Such a temperature is typical of the photosphere, not of the corona. A component of a possible coronal formation model that explains the FIP ordering is the dynamical model of Geiss and Bochsler (1984) for ionization of heavy elements in a gas at a constant temperature of 10^4 °K and electron density of $10^{10} cm^{-3}$. In this model, based on a numerical calculation including the effects of collisional excitation, photoionization and recombination, the low-FIP species Mg and Si ionize very quickly (~1 sec) while the high-FIP elements C, N, O, Ne and Ar require ~100 sec for all atoms to ionize. In the presence of a coronal formation process with a time scale ~10 sec, and a mechanism for separation of ions from neutral atoms, a fractionation of the high-FIP species should occur, as is observed. Equilibrium ionization models (e.g., Vernazza et al. 1981) do retain a FIP ordering but are not applicable to the fractionation of the corona since all species will become ionized given sufficient time. On more general grounds, a sharp discontinuity in fractionation may be expected in the neighborhood of 10 eV, as is observed. The predominance of hydrogen in the sun implies a sharp dropoff in the number of photons available for ionization above the hydrogen Lyman α energy of 10.2 eV; hence species with FIP greater than this limit will be more difficult to ionize. The same effect may apply to the interstellar medium, although evidence for a step in the FIP effect for galactic cosmic rays near 10 eV is inconclusive. In view of the above observational and theoretical considerations, we shall take the fractionation f_c of the photospheric material during coronal formation to be the same for all flares and dependent on the first ionization potential I_Z of the element in question.

The fractionation f_a of coronal material during acceleration to SEP energies and injection into the interplanetary medium has a magnitude which varies from flare to flare and also depends on the velocity β and on Q/M, where Q is the *ionic* charge of the species in question and M its mass. The absence of perfect ordering by FIP in average SEP abundances relative to the photosphere

may be explained by differences between elements in the efficiency of acceleration of the coronal particles to SEP energies. This suggestion is based on physical models of electromagnetic acceleration, in which the magnetic rigidity (momentum per unit charge)

$$R = \frac{Mv}{Q} = \frac{M\beta c}{Q} \tag{4.3}$$

plays an important role. For example, a diffusion mean free path λ that increases with increasing rigidity will result in higher-rigidity species tending to be scattered further from the coronal shock wave, making fewer repeated encounters with the shock and therefore being less efficiently accelerated. This would result in a tendency in most flares for observed differential energy spectra of solar particles to be steeper for higher Z, consistent with the present observations. Similarly, for particles of comparable energy per nucleon, those with a lower charge-to-mass ratio should be depleted with respect to those with a higher ratio. Variability in the rigidity-dependent acceleration from flare to flare would also provide at least a partial interpretation for the approximately monotonic Z-dependence of the flare-to-flare variability, as was noted by Meyer (1985), since Q/M for SEPs varies roughly monotonically with Z. Thus it is natural to consider whether the differences in the SEP composition between individual flares can be correlated with Q/M of the coronal particles. These differences could then be attributed to either (1) the presence of different ionic charge states, and hence different rigidities, caused by differing coronal temperatures, (2) differences between flares in the rigidity-dependence of the acceleration process, or (3) a combination of both effects. If individual flare composition differences are ordered by Q/M, then this would also be true for the *range* of SEP composition variability, as well as for the difference between the *average* SEP composition and the true coronal composition. Since we have already noted that the mean SEP composition is very close to photospheric for low-FIP elements, we anticipate that this residual average fractionation will be small compared to that seen in many individual flares. Early attempts have

been made to correlate the range of SEP composition variability with calculated or measured SEP charge-to-mass ratios (Meyer 1985). Such work has relied on the availability of theoretical ionization equilibrium calculations of the ionic charge states present at coronal temperatures for various elements (Jordan 1969; Jacobs et al. 1977, 1980), and on early measurements of actual SEP charge states (Gloeckler et al. 1981).

The fractionation f_p of SEPs during interplanetary propagation also varies from flare to flare, being dependent on time and on the spatial coordinates (heliocentric radius r, latitude ϑ, and longitude φ) of the flare site relative to the observing site as well as on β and Q/M (and the spectral index γ if adiabatic deceleration is important). The Q/M-dependence could contribute, along with f_a, to any observed ordering of SEP composition by Q/M. To treat the dependence of f_p on time, previous studies (e.g., Cook et al. 1979, 1980, 1984) often restricted themselves to the decay phase of the flare, where the measured abundance ratios are constant in time, i.e., $\frac{f_p(Z)}{f_p(Si)}$ is constant, and this ratio was implicitly or explicitly assumed to be unity during the decay phase. The approach used here is somewhat different. Although f_p is not known, statistical uncertainty is minimized by using data from the entire flare event. If this results in a Z-dependence to f_p integrated over time, this will be apparent as a function of r, ϑ, φ and Q/M. In general the dependence on r, ϑ and φ (and time as well) will vary with Q/M, and it is only this variability which is important; to the extent that r, ϑ, φ and t dependence are independent of Q/M and β, they have no effect on the abundance ratio of two elements. Therefore we will consider only the variability of the spatial dependence with Q/M. The time-dependence is known to be Q/M-dependent based on earlier work (von Rosenvinge and Reames 1979, Mason et al. 1983). Thus one expects to be able to reduce f_p to primarily a Q/M fractionation. The dependence of f_p on time and on the spatial coordinates will be discussed in more detail in Section 4.1.2.

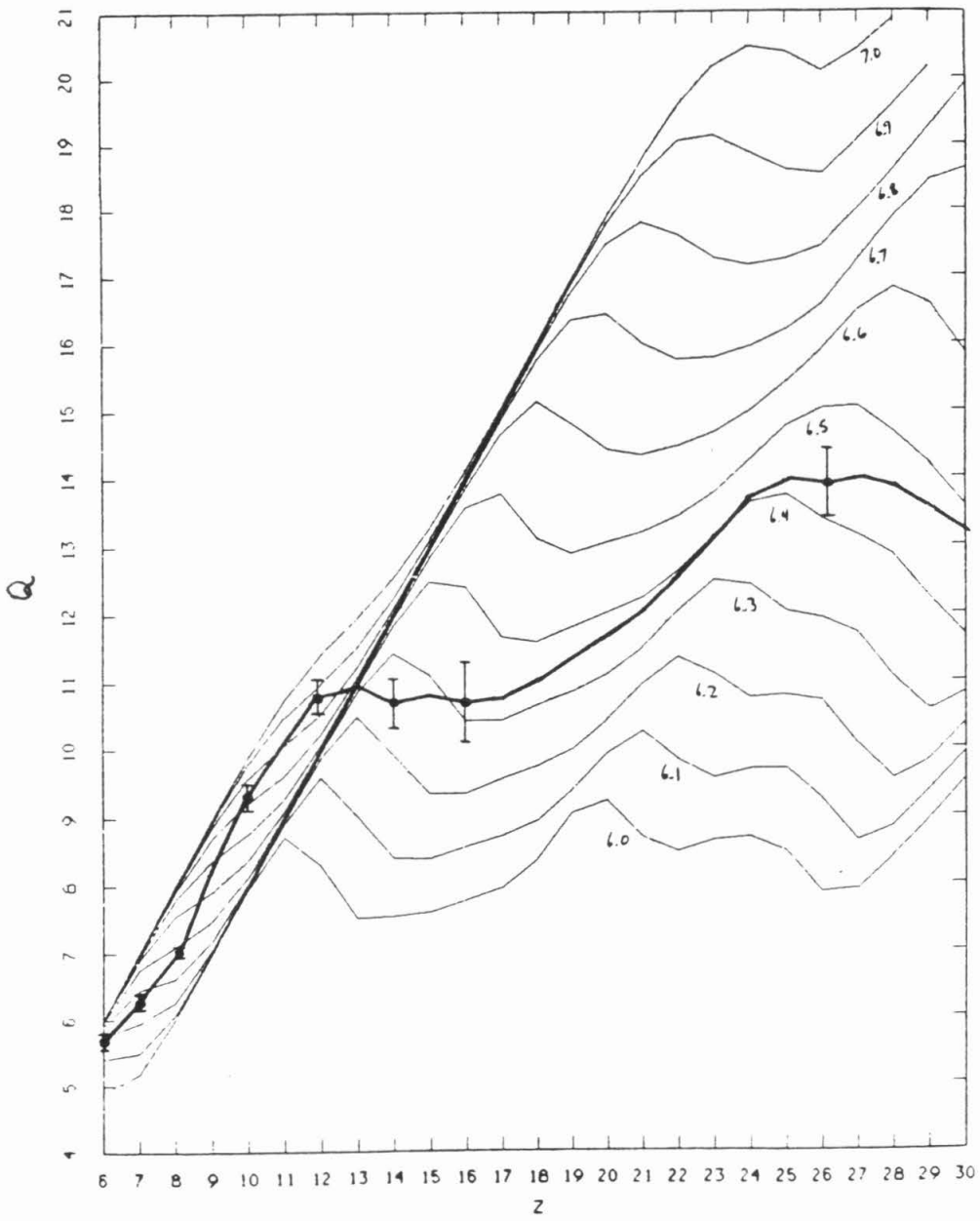

Fig. 4.1. Ionic charge state Q vs. Z for elements in the charge range $3 \leq Z \leq 30$. Points with error bars are measured values for SEPs (Gloeckler et al. 1981, Luhn et al. 1984). Other elements (dark curve) were interpolated using the ionization equilibrium calculations of Shull and van Steenberg (1982) (see text for details). The lighter curves are the Shull and van Steenberg calculated mean Q at several specific temperatures in the coronal temperature range. The curves are labeled with $\log_{10}(T\ ^{\circ}K)$.

If the Q/M-dependence of f_p and f_a differs only in magnitude and sign from flare to flare, one may average the raw SEP abundances from the individual flares, and perform a single Q/M correction to the averages to simultaneously account for the net effect of both acceleration and propagation fractionation. The result is a SEP-derived estimate of the true coronal composition. Finally, a FIP-dependent correction may be applied to remove the coronal fractionation f_c, resulting in a SEP-derived estimate of the true composition of the solar photosphere.

The values of mean Q to be used in all that follows were derived from recent SEP ionic charge state measurements for C, O and Fe (Gloeckler et al. 1981) and for N, Ne, Mg, Si and S (Luhn et al. 1984). These values (Fig. 4.1) are averages from three flares; the mean Q typically differs by no more than about 5 - 10% between the flares, and the quoted uncertainties on the mean Q are in the 1 - 6% range. The observations are not consistent with a single coronal temperature based on the theoretical ionization equilibrium calculations of Shull and van Steenberg (1982), implying weaknesses in the assumed coronal model, most likely in the assumptions of charge equilibrium or the Maxwellian electron distribution. Earlier ionization equilibrium calculations (Jordan 1969, Jacobs et al. 1977, 1980) yield a dependence of mean Q on temperature not appreciably different in the relevant temperature range. The temperatures implied by the Shull and van Steenberg calculations corresponding to the measured values of Q were interpolated or extrapolated to elements not measured, yielding interpolated values of Q for these elements[1]. This produces a dependence of Q on Z which qualitatively follows the theoretical curves for particular temperatures, although the pronounced plateaus associated with closed shells of electrons are much less significant in the observed data than in the theoretical calculation. The adopted Q/M values and first ionization potentials for the elements with $3 \leq Z \leq 30$ are given in Table 4.1.

[1] Corrections to several apparent typographical errors in the rate coefficient tables, as well as the errata published in *Ap. J. Suppl.* **49**, 351, 1982 June, were applied to the Shull and van Steenberg calculations.

Table 4.1. Adopted values of SEP charge-to-mass ratio (Q/M) and first ionization potential (FIP) for all elements with $3 \leq Z \leq 30$. Values of Q (Fig. 4.1) for C, N, O, Ne, Mg, Si, S and Fe were obtained from recent SEP ionic charge state measurements (Gloeckler et al. 1981, Luhn et al. 1984); all other elements were interpolated or extrapolated using the ionization equilibrium calculations of Shull and van Steenberg (1982) (see text for details). Quoted error bars on the measured Q values range from ~1 to ~6%. Values for M are averages of isotopic masses weighted for each element by their relative abundances in the Cameron (1982) isotopic abundance tabulation. FIP values are from CRC Handbook of Chemistry and Physics, 60th ed. (1979-80), p. E-68.

Z	Q/M	FIP (eV)
3	0.435	5.392
4	0.447	9.322
5	0.466	8.298
6	0.478	11.260
7	0.450	14.534
8	0.441	13.618
9	0.432	17.422
10	0.464	21.564
11	0.440	5.139
12	0.448	7.646
13	0.410	5.986
14	0.384	8.151
15	0.351	10.486
16	0.336	10.360
17	0.306	12.967
18	0.305	15.759
19	0.292	4.341
20	0.293	6.113
21	0.270	6.54
22	0.264	6.82
23	0.259	6.74
24	0.265	6.766
25	0.256	7.435
26	0.251	7.870
27	0.239	7.86
28	0.237	7.635
29	0.215	7.726
30	0.203	9.394

4.1.2 The Role of Propagation Effects

As described in the preceding section, it is necessary to determine the importance of fractionation due to propagation effects, with particular attention to their possible dependence on Q/M. With the Voyager data this issue can be addressed in several ways:

(1) Examination of the time-dependence of abundance ratios within individual flares.

(2) Looking for trends in the measured average abundance ratios from individual flares with radial distance of the spacecraft from the sun at the time of the flare event.

(3) Comparing abundance ratios for a given flare derived from Voyager 1 data alone with those derived from Voyager 2 data alone, looking for trends associated with the changing spatial separation of the two spacecraft.

(4) Looking for differences in the shape of the differential energy spectrum of different elements, which would be indicative of a dependence of the abundance ratio on energy per nucleon (or equivalently velocity).

Previous research (e.g., Cook et al. 1984), based on these types of investigations applied to a smaller sample of flare events, led to the conclusion that such effects were not a major contributor to the observed flare-to-flare variability. It is desirable to confirm this conclusion with a flare sample that is larger and more varied (both in flare intensity and circumstances of observation), and to determine the influence of these effects on the average measured SEP elemental abundances. In addition, the recent availability of direct measurements of SEP ionic charge states (Gloeckler et al. 1981, Luhn et al. 1984) make possible quantitative evaluations of models involving rigidity-dependent effects to explain the observed spatial, temporal and spectral differences.

Time dependence of abundance ratios has been observed previously. Cook et al. (1984) found that the Fe/O ratio changed by up to a factor of 3 - 5 during a single flare event, while the ratios of C, Ne, Mg and Si to oxygen did not vary more than ~30%. von Rosenvinge and Reames (1979) and Mason et al. (1983) found a similar degree of variation in the Fe/O ratio. The present work confirms these results. For each of the 22 flare events, the abundances of C, N, Ne, Mg, Si, and Fe with respect to O were determined as a function of time during each flare event by binning the events in order of time of observation. Due to limited statistics the procedure was unproductive for the smaller flares, failing to show any statistically significant trends in the abundance ratios with time. Fig. 4.2 shows an example for several large flares. Plotted are the PHA counts ratio (equal within a few percent to the actual abundance ratio) for Fe/O as a function of time for flare period 7; the ratio varied by about a factor of 4 during this time period. A factor of 2 variation was seen in Si/O and a factor of 1.5 in C/O, while N/O, Ne/O and Mg/O showed little or no statistically significant variation. Other flares showed smaller variations, and only one, flare 5, showed larger statistically significant variations (about a factor of 3 for C/O). In all cases where significant temporal variation was seen, most of the variation took place during a relatively brief time period at the onset of the flare. As Mason et al. (1983) have noted, this behavior can be explained if the species that is enhanced during the onset period has a larger diffusion coefficient κ for interplanetary propagation, allowing it to reach the observation site faster, and theoretical propagation models suggest that the mean free path λ has the form $\lambda \propto R^{\alpha}$, where R is the rigidity. The diffusion coefficient can be expressed as $\kappa = \lambda v/3$ and the flare rise time $\tau \propto 1/\lambda v$. Thus one would expect to see time-dependence to the Fe/O ratio, since Fe and O have significantly different Q/M, but little change in ratios such as N/O, Ne/O or Mg/O, since these have comparable Q/M. This is in agreement with the observations noted above. The model also agrees with the observation of velocity dispersion in such flares (e.g., Cook 1981), since it allows the higher-energy particles to arrive ahead of the lower-

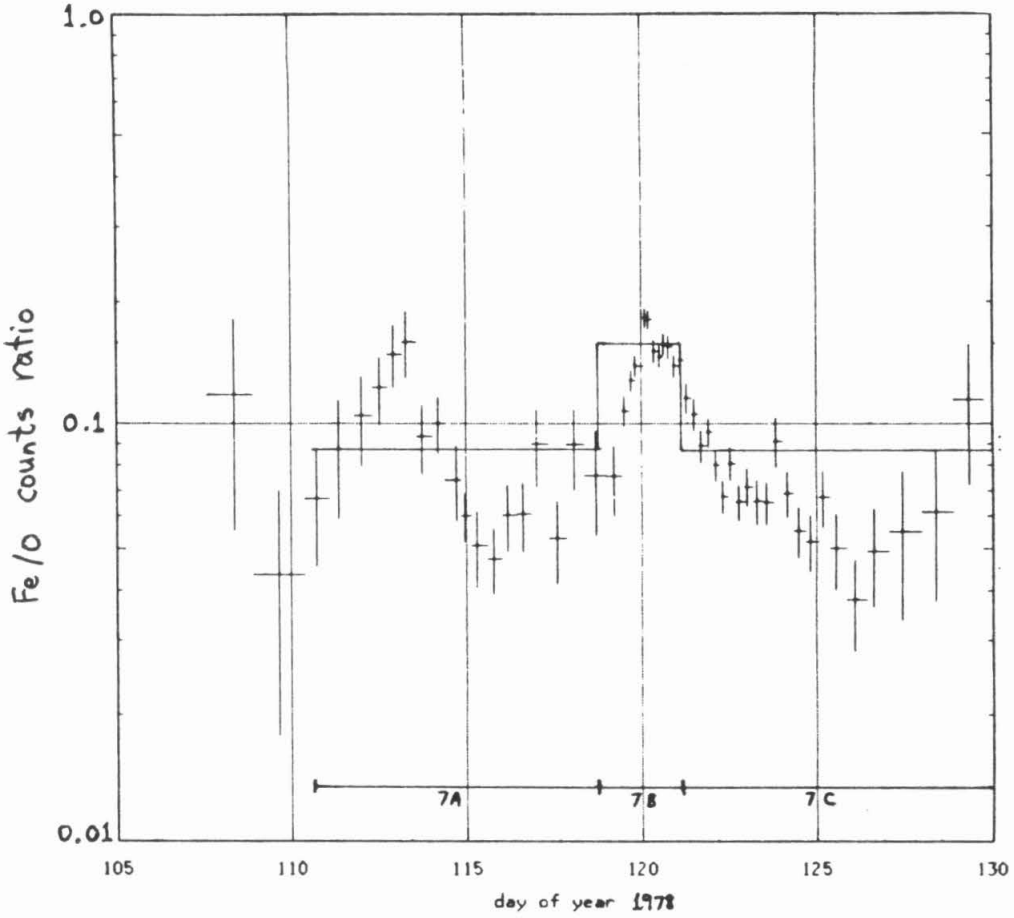

Fig. 4.2. Fe/O particle count ratio as a function of time during flare period #7. Horizontal line across each of the individual flares indicates the average abundance for the flare obtained by the procedure of Chapter 3.

energy particles of a given species, producing a steepening of the differential energy spectrum with time.

It may also be noted that the observed time-variations are not sufficiently large, or sustained over a sufficiently long time period, to make time-averaged abundances grossly dependent on the precise choice of time interval. This is in agreement with the results of Cook et al. (1984) who found that abundance determinations (except for Fe) were relatively insensitive to the choice of time period, i.e., whether the onset phase of the flare is included. Thus we are justified in improving the statistical precision of the results as much as possible by including for each flare the entire time period meeting the flux threshold criterion. The observed degree of time variation is, however, certainly capable of contributing significantly to the typical ~20% differences observed between the present results for individual flares and the SEP composition from the same flares determined by Cook et al. (1980, 1984) using different (and generally more restrictive) selections of the time period. In particular, Cook et al. excluded the onset period of the flare wherever possible, and this is when the bulk of the variation takes place. It may be argued that the inclusion of the onset period is appropriate since the composition of the original population of particles will be most accurately reflected by the total sample that eventually arrives at the observing site, despite the presence of differing velocities of propagation. In any case, the fact that the time-dependence is a function of Q/M means that it will be accounted for when a general Q/M correction is applied to the SEP average abundances to obtain unfractionated coronal abundances (Section 4.5).

Since the abundance ratios averaged over entire individual flares of elements widely separated on the charge scale can vary by an order of magnitude or more between flares, it is clear that time-dependence of abundance ratios during individual flares, cannot be a major contributing factor to the flare-to-flare variation.

The radial distance of the spacecraft from the sun increases monotonically (and approximately linearly) from 1 AU at the start of the mission to about 15 AU for Voyager 1 and 11 AU for Voyager 2 at the time of the last flare event included in this study. When the abundances relative to Si for individual flares are ordered chronologically, no pattern is apparent for any of the ratios. This suggests that large-scale propagation effects do not seriously alter the observed composition of the flare particles.

A further measure of the magnitude of propagation effects, but on a somewhat smaller distance scale, is provided by comparison of abundance ratios obtained from Voyager 1 data with the same ratios for the same flare obtained from Voyager 2 data. The radial separation of the spacecraft during the mission ranged from a small fraction of an AU to about 4 AU; azimuthal separation did not exceed 12°. The ratios of C, N, O, Ne, Mg, S and Fe relative to Si were calculated for each flare by the same procedure described in Section 3.5, but treating Voyager 1 and 2 data separately. The ratio of the Voyager 1 abundance to the Voyager 2 abundance was calculated. It was found that the smaller flares showed no statistically significant difference between the spacecraft for any of the abundance ratios, and that while the larger flares do show some statistically significant differences, these are almost always no larger than 10 - 20%, far too small to be a major factor in the order-of-magnitude differences between flares.

These observations are reflected in Table 4.2, in which the V1/V2 ratios for all of the individual flares are averaged, using the same averaging technique to be used on the abundance ratios themselves (Section 4.3.1). The flare-averaged V1/V2 ratios are consistent with unity, with a typical uncertainty of 4% and a typical population variance of 10%. The observations also confirm that one is justified in summing the data from the two spacecraft in obtaining the abundances in a given flare event.

In an alternative approach to the same issue, one may eliminate the role of

Table 4.2. Averaged ratios of elemental abundances obtained by Voyager 1 to those obtained by Voyager 2. The data from the different flares are averaged using the combined statistical and population variance weighting technique described in Section 4.3.1. Values in parenthesis are factors of uncertainty.

elemental ratio	V1/V2 ratio	population width factor
C/Si	1.006 (1.044)	1.118
N/Si	1.033 (1.042)	1.098
O/Si	1.034 (1.030)	1.068
Ne/Si	0.964 (1.052)	1.138
Mg/Si	0.985 (1.032)	1.067
S/Si	1.006 (1.047)	1.078
Fe/Si	0.979 (1.038)	1.083

the normalizing element Si by directly taking the ratio of the number of counts of a given element seen by the two spacecraft, scaled by the appropriate product of livetime and geometry factor. The resulting ratios for different elements may all be systematically different from unity in a given flare event if the intensity at the two spacecraft differed on account of radial gradient effects or of being unequally well-connected with the flare site. But by carrying out a least-squares fit to a straight line of the V1/V2 ratios for the different elements, one finds that there is generally no statistically significant trend in the ratio with Z, or any significant deviations from the mean ratio greater than the 10 - 20% noted above. In Appendix H, the best-fit slopes and offsets for each of the flares are shown along with the radial, latitudinal and longitudinal separation of the spacecraft at the time of the flare. Fig. 4.3 shows the V1/V2 counts ratio (uncorrected for livetime and geometry factor, which are the same for all elements in a given flare) for several flare events, plotted vs. Q/M; the slight variation seen can be ordered by Q/M and therefore can be corrected for in the manner described above, although the correction in this case is small compared to the other Q/M-dependent effects.

We next consider the dependence of abundance ratios on incident energy per nucleon, which may reflect Q/M-dependence in both propagation and acceleration effects. Differential energy spectra were generated for each of the eight abundant elements for each flare event by dividing the LET and HET energy ranges into between 6 and 16 energy bins each. The data from the two spacecraft were treated separately. The resulting spectra were fit to a power-law functional form

$$\frac{dJ}{dE} = k E^{-\gamma} \tag{4.4}$$

with k and γ as free parameters. (A few flares were poorly fit by this functional form and were much better fit by a function such as Eq. 3.14; in these cases the slope was separately determined at energies of 5, 10 and 20 MeV/nucleon,

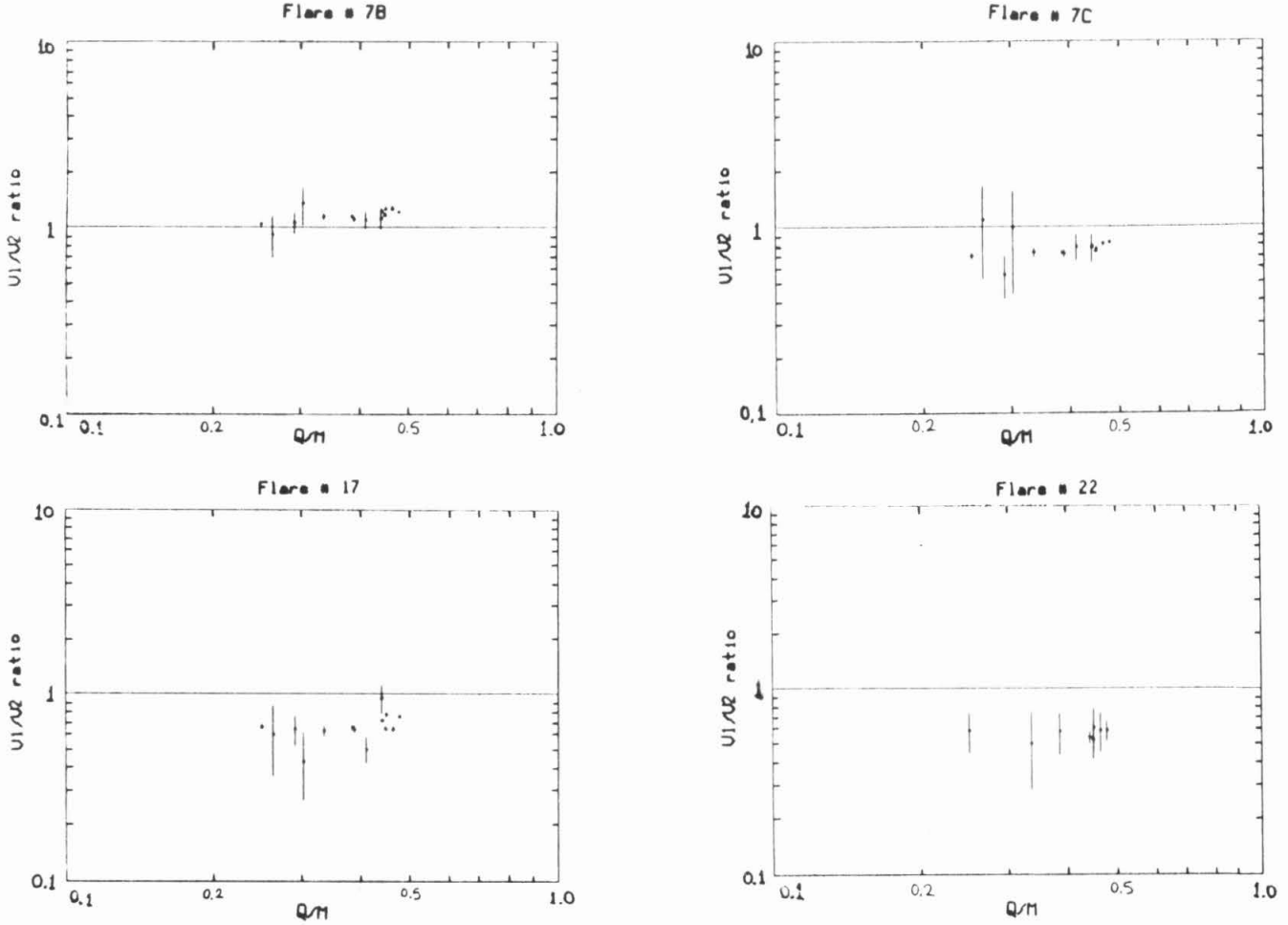

Fig. 4.3. Voyager 1/Voyager 2 ratio of weighted particle counts vs. Q/M for four representative flares. Values for Q were obtained from recent SEP ionic charge state measurements (Gloeckler et al. 1981, Luhn et al. 1984).

spanning the appropriate energy interval). The constant k is unimportant as it simply fixes the normalization of the abundance ratio; if the spectra of two elements have the same γ, the ratio of the k values is the abundance ratio. A difference in the spectral index γ for two elements indicates an energy-dependence in their abundance ratio. Fig. 4.4 shows a sample spectrum, with the best-fit power law, for an element in one typical flare as seen by one of the spacecraft.

If one looks at the best-fit spectral indices of different elements for individual flares one finds that for the small flares, the uncertainty in the determination of γ masks any possible difference. The large flares such as 5, 7a, 20 and 24 have very well-defined spectral indices, but they show little or no difference between elements ($\Delta\gamma \sim 0.5$ or less); the trends that are seen are modest (e.g., flare 1d), and only in a few cases such as flare 3 does the range of variation of γ amount to more than ~1. Even this degree of variation, however, is significant when the spectrum is integrated over the entire energy interval, and calls into question the significance of the "abundance ratio" for such flares measured in any particular energy interval. However, flares showing relatively large variations of γ have not been excluded from this study because as noted above, the spectral differences between elements in individual flares may be a manifestation of a rigidity-dependent acceleration and/or propagation effect, and therefore that γ may be correlated with mean Q/M of the particle. Indeed, when γ is plotted against Q/M for individual large flares, a smooth, power-law dependence is seen (Fig. 4.5). This dependence will be removed when the unfractionated coronal abundances are derived from the SEP observations by treating the average acceleration/propagation fractionation as a power-law function of rigidity. Since the spectral variation of individual flares shows the same type of dependence, this process will also remove any residual fractionation in the average abundances due to spectral variation in individual flares making up the average, although the presence of differing degrees of spectral variation between *flares* will contribute to the *uncertainty* in the average abundances.

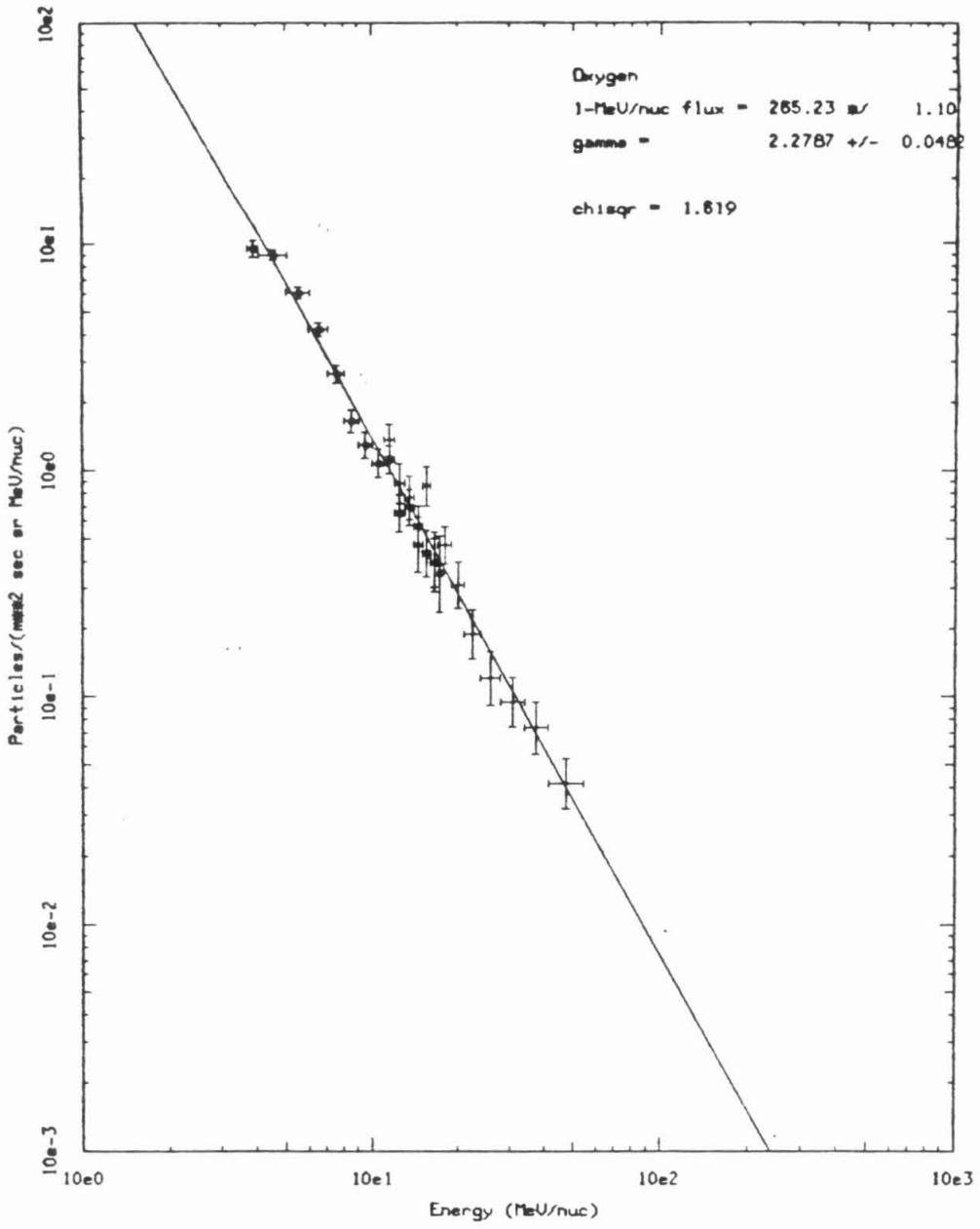

Fig. 4.4. Differential energy spectrum of oxygen from Voyager 1 CRS data for flare period 1e. Large points represent LET data, small points HET data. Also shown is the least-squares best fit power-law function of energy (Eq. 4.4) with the best-fit value of the spectral index and the χ^2 of the fit.

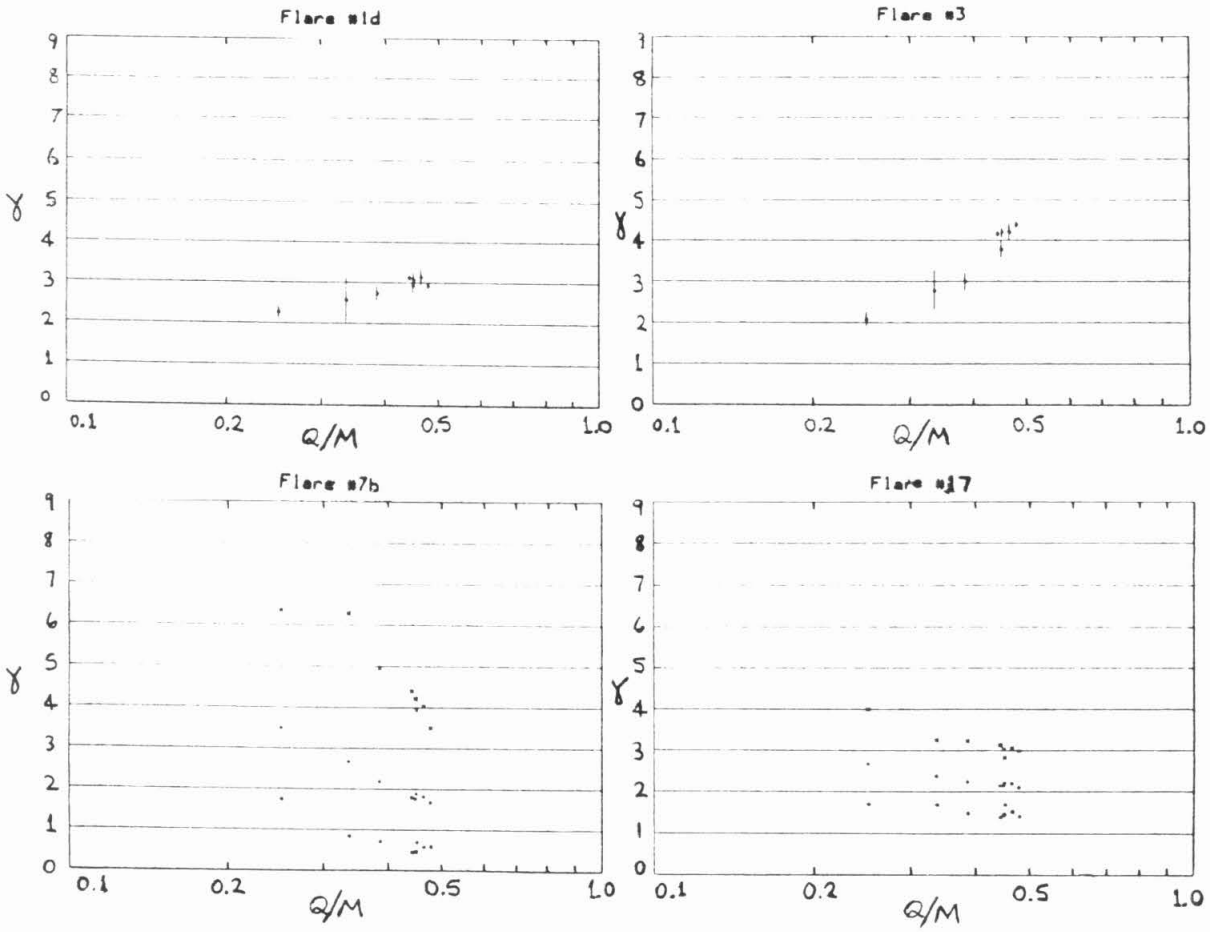

Fig. 4.5. Spectral indices for the eight most abundant elements (C, N, O, Ne, Mg, Si, S and Fe) plotted vs. Q/M for four representative flares using Voyager 2 data. Except for flares 7b, 7c and 17, the spectral indices were obtained by doing least-squares fits of the differential energy spectra (Fig. 4.4) to a power-law function of incident energy (Eq. 4.4). The three remaining flares were poorly fit by this functional form and were instead fit to the form of Eq. 3.14, the local spectral indices at energies of 5, 10 and 20 MeV/nucleon being obtained by analytic differentiation of Eq. 3.14 using the best-fit values of the parameters. The values of Q were obtained from recent SEP ionic charge state measurements (Gloeckler et al. 1981, Luhn et al. 1984).

Thus we conclude that while the energy-dependence of the abundance ratios may alter the measured average SEP composition, the alteration has a simple dependence on Q/M and will therefore be removed when unfractionated coronal and photospheric abundances are derived by applying an average Q/M correction to the average SEP abundances. The Q/M-dependence of γ will contribute to the uncertainty of these derived solar abundances, due to flare-to-flare spectral differences. Spectral differences do contribute significantly to differences in SEP composition determined over differing energy intervals for the same flare event, e.g., the typical ~20% differences between the present results for flares 1d, 1e, 3, 5, 7a, 7b and 7c and the results of Cook et al. (1980, 1984).

Since in flares where γ differs significantly between different elements, the Q/M-dependence tends to be smooth and monotonic, the difference in γ for neighboring elements on the charge scale is much less than the full range of variability in γ. Thus the abundance ratios and uncertainties for pairs of neighboring elements, which have similar Q/M, tend to be less fractionated by the Q/M-dependence of γ than ratios of widely separated elements.

We conclude that the flare-to-flare compositional differences outlined in Section 4.2 are real differences associated with the coronal source region of the particles, that they are correlated with the charge-to-mass ratios of the species in question and primarily reflect a rigidity-dependent selection effect in the SEP acceleration process, and that interplanetary propagation has a comparatively minor effect although it is also organized by Q/M.

4.2 Abundant Elements in Individual Flare Events

Table 4.3 lists the abundances relative to Si of the other seven abundant heavy elements (C, N, O, Ne, Mg, S and Fe) for each of the 22 flare periods in the Voyager data set, as calculated by the procedure in Chapter 3. Also tabulated for each flare are "raw counts," the actual number of PHA events counted in

Table 4.3. Abundances relative to Si for the seven most abundant heavy elements for the 22 flare periods in the Voyager LET/HET data set. "Raw counts" refers to the total PHA events in the time, energy and charge interval, and "weighted counts" to the PHA events corrected with the livetime-geometry factor weighting factors of Appendix F. Raw counts determine the statistical uncertainties in the abundances, while the weighted counts determine the actual abundance ratios.

Flare		C	N	O	Ne	Mg	Si	S	Fe
1a	raw cts.	151	44	315	43	49	20	1	24
	wtd. cts.	128.	36.6	274.	35.6	44.5	18.5	1.00	22.4
	Z/Si	$6.92^{+2.07}_{1.61}$	$1.98^{+0.66}_{0.52}$	$14.8^{+4.3}_{3.5}$	$1.93^{+0.65}_{0.51}$	$2.41^{+0.79}_{0.63}$	1.00	$.054^{+.127}_{.046}$	$1.21^{+0.48}_{0.36}$
1b	raw cts.	139	39	253	41	51	23	10	16
	wtd. cts.	123.	34.6	224.	38.2	47.4	22.0	9.77	14.9
	Z/Si	$5.58^{+1.55}_{1.23}$	$1.57^{+0.51}_{0.41}$	$10.2^{+2.8}_{2.2}$	$1.74^{+0.55}_{0.46}$	$2.16^{+0.66}_{0.53}$	1.00	$.444^{+.223}_{.166}$	$.679^{+.280}_{.218}$
1c	raw cts.	63	22	155	29	35	37	9	69
	wtd. cts.	60.4	21.6	144.	27.5	32.7	36.6	8.45	67.2
	Z/Si	$1.65^{+0.40}_{0.34}$	$.591^{+.194}_{.156}$	$3.93^{+0.84}_{0.71}$	$.753^{+.223}_{.186}$	$.894^{+.260}_{.209}$	1.00	$.231^{+.110}_{.080}$	$1.84^{+0.44}_{0.37}$
1d	raw cts.	1090	305	2343	332	415	348	70	502
	wtd. cts.	926.	271.	2104.	342.	390.	331.	64.5	471.
	Z/Si	$2.80^{+0.18}_{0.17}$	$.819^{+.068}_{.064}$	$6.36^{+0.38}_{0.36}$	1.03 ± 0.08	1.18 ± 0.09	1.00	$.195^{+.028}_{.026}$	1.42 ± 0.10
1e	raw cts.	1054	350	2769	542	727	732	188	1837
	wtd. cts.	933.	312.	2487.	480.	656.	663.	171.	1733.
	Z/Si	1.41 ± 0.07	$.471^{+.032}_{.031}$	3.75 ± 0.18	$724^{+.043}_{.041}$	$.989^{+.054}_{.052}$	1.00	$.258^{+.025}_{.021}$	$2.61^{+0.12}_{0.11}$
3	raw cts.	985	278	2020	318	315	277	84	374
	wtd. cts.	941	284	1955	301	304.	269.	80.9	363.
	Z/Si	$3.50^{+0.25}_{0.24}$	$.981^{+.069}_{.068}$	$7.26^{+0.49}_{0.46}$	$1.12^{+0.10}_{0.09}$	$1.13^{+0.10}_{0.09}$	1.00	$.301^{+.041}_{.037}$	1.35 ± 0.11
4	raw cts.	105	23	203	28	36	24	7	27
	wtd. cts.	100.	20.0	191.	25.2	34.1	23.7	7.00	27.0
	Z/Si	$4.22^{+1.17}_{0.94}$	$.841^{+.364}_{.242}$	$8.05^{+2.14}_{1.70}$	$1.06^{+0.37}_{0.30}$	$1.43^{+0.46}_{0.37}$	1.00	$.295^{+.176}_{.124}$	$1.14^{+0.39}_{0.31}$
5	raw cts.	4578	1296	10249	1574	2026	1403	296	1210
	wtd. cts.	4142.	1196.	9580.	1493.	1944.	1362.	291.	1202.
	Z/Si	$3.04^{+0.10}_{0.09}$	$.878^{+.035}_{.034}$	$7.03^{+0.21}_{0.20}$	1.10 ± 0.04	1.43 ± 0.05	1.00	213 ± .014	$.882^{+.036}_{.035}$

Table 4.3 (continued).

Flare		C	N	O	Ne	Mg	Si	S	Fe
6	raw cts.	33	8	58	4	4	4	2	1
	wtd. cts.	32.4	6.27	55.4	4.00	4.00	4.44	2.00	1.00
	Z/Si	$7.31^{+7.02}_{-3.46}$	$1.41^{+1.50}_{-0.80}$	$12.5^{+11.9}_{-6.6}$	$.901^{+1.108}_{-.591}$	$.901^{+1.106}_{-.591}$	1.00	$.450^{+.783}_{-.359}$	$.225^{+.864}_{-.219}$
7a	raw cts.	6142	1582	12333	1564	2061	1525	328	1089
	wtd. cts.	5448.	1434.	11221.	1439.	1915.	1420.	308.	1048.
	Z/Si	3.84 ± 0.11	1.01 ± 0.04	$7.90^{+0.22}_{-0.21}$	1.01 ± 0.04	1.35 ± 0.05	1.00	$.217^{+.014}_{-.013}$	$.738^{+.030}_{-.029}$
7b	raw cts.	18101	5923	50385	5405	9217	9095	2043	8213
	wtd. cts.	14615.	4860.	41902.	4597.	7979.	8408.	1959.	8163.
	Z/Si	1.74 ± 0.02	.578 ± .010	4.98 ± 0.06	$.547^{+.010}_{-.009}$	.949 ± .014	1.00	.233 ± .006	.971 ± .015
7c	raw cts.	18812	5278	42235	4600	7964	6155	1222	3710
	wtd. cts.	16409.	4717.	38595.	4288.	7561.	5989.	1206.	3689.
	Z/Si	2.74 ± 0.04	.787 ± .015	6.44 ± 0.09	.716 ± .014	1.26 ± 0.02	1.00	$.201^{+.007}_{-.006}$	.616 ± .013
8	raw cts.	225	64	396	53	76	33	3	5
	wtd. cts.	216.	64.6	408.	55.1	81.2	36.2	3.67	5.67
	Z/Si	$5.98^{+1.32}_{-1.10}$	$1.79^{+0.46}_{-0.38}$	$11.3^{+2.4}_{-2.0}$	$1.52^{+0.40}_{-0.33}$	$2.24^{+0.56}_{-0.46}$	1.00	$.101^{+.102}_{-.069}$	$.157^{+.111}_{-.075}$
9	raw cts.	36	16	121	17	16	21	3	22
	wtd. cts.	34.3	15.2	117.	15.8	16.3	21.9	3.00	24.4
	Z/Si	$1.57^{+0.59}_{-0.42}$	$.693^{+.292}_{-.266}$	$5.34^{+1.27}_{-1.23}$	$.723^{+.299}_{-.232}$	$.837^{+.340}_{-.265}$	1.00	$.137^{+.139}_{-.061}$	$1.11^{+0.43}_{-0.33}$
10	raw cts.	120	26	262	26	45	25	4	28
	wtd. cts.	109.	25.0	255.	26.0	47.7	25.2	4.00	29.7
	Z/Si	$4.32^{+1.16}_{-0.85}$	$.994^{+.342}_{-.275}$	$10.1^{+2.6}_{-2.1}$	$1.03^{+0.36}_{-0.29}$	$1.89^{+0.67}_{-0.47}$	1.00	$.159^{+.132}_{-.085}$	$1.18^{+0.40}_{-0.32}$
13	raw cts.	294	58	440	67	88	29	3	9
	wtd. cts.	287.	56.9	445.	69.2	90.5	30.3	3.00	9.00
	Z/Si	$9.47^{+2.23}_{-1.81}$	$1.88^{+0.51}_{-0.42}$	$14.7^{+3.4}_{-2.8}$	$2.28^{+0.61}_{-0.50}$	$2.98^{+0.76}_{-0.65}$	1.00	$.099^{+.099}_{-.066}$	$.297^{+.152}_{-.112}$
16	raw cts.	836	190	1547	202	215	149	36	141
	wtd. cts.	706.	165.	1377.	177.	199.	146.	33.2	136.
	Z/Si	$4.83^{+0.46}_{-0.43}$	$1.13^{+0.13}_{-0.12}$	$9.41^{+0.87}_{-0.80}$	$1.21^{+0.14}_{-0.13}$	$1.36^{+0.16}_{-0.14}$	1.00	$.227^{+.049}_{-.042}$	$.929^{+.118}_{-.106}$
17	raw cts.	15044	3935	32672	4481	6109	4807	991	3601
	wtd. cts.	12336.	3272.	27974.	3926.	5485.	4477.	946.	3710.
	Z/Si	2.76 ± 0.05	.731 ± .016	6.25 ± 0.10	$.877^{+.019}_{-.018}$	1.23 ± 0.02	1.00	$.211^{+.008}_{-.007}$	$.829^{+.019}_{-.018}$

Table 4.3 (continued).

Flare		C	N	O	Ne	Mg	Si	S	Fe
20	raw cts.	1509	396	3235	439	627	478	106	354
	wtd. cts.	1316.	347.	2934.	410.	599.	482.	108.	380.
	Z/Si	$2.73^{+0.15}_{-0.14}$	$.720^{+.051}_{-.049}$	$6.08^{+0.31}_{-0.30}$	$.850^{+.069}_{-.066}$	1.24 ± 0.08	1.00	$.223^{+.026}_{-.024}$	$.788^{+.056}_{-.055}$
22	raw cts.	45	13	109	12	16	11	10	8
	wtd. cts.	43.3	12.5	101.	12.1	15.5	11.0	10.0	8.00
	Z/Si	$3.93^{+1.80}_{-1.27}$	$1.14^{+0.63}_{-0.45}$	$9.20^{+4.03}_{-2.79}$	$1.10^{+0.63}_{-0.46}$	$1.41^{+0.75}_{-0.63}$	1.00	$.909^{+.548}_{-.366}$	$.727^{+.474}_{-.328}$
24	raw cts.	770	202	1453	211	255	174	38	80
	wtd. cts.	658.	178.	1338.	201.	250.	171.	38.3	82.2
	Z/Si	$3.84^{+0.35}_{-0.32}$	$1.04^{+0.12}_{-0.11}$	$7.80^{+0.87}_{-0.82}$	$1.17^{+0.13}_{-0.12}$	$1.46^{+0.16}_{-0.14}$	1.00	$.223^{+.048}_{-.040}$	$.479^{+.072}_{-.065}$
25	raw cts.	77	19	155	19	19	17	5	10
	wtd. cts.	69.0	17.7	152.	19.5	20.0	18.0	5.00	11.9
	Z/Si	$3.84^{+1.31}_{-1.00}$	$.988^{+.422}_{-.325}$	$8.46^{+2.78}_{-2.10}$	$1.08^{+0.46}_{-0.36}$	$1.11^{+0.46}_{-0.36}$	1.00	$.278^{+.209}_{-.136}$	$.664^{+.354}_{-.256}$

Table 4.4. Abundances relative to Si for five elements of intermediate abundance from the 10 flare periods in the Voyager LET/HET data set for which statistically meaningful abundances are obtainable. "Raw counts" refers to total PHA events in the time, energy and charge interval, and "weighted counts" to the PHA events corrected with the livetime-geometry factor weighting factors of Appendix F. Raw counts determine the statistical uncertainties in the abundances, while the weighted counts determine the actual abundance ratios.

Flare		Na	Al	Ar	Ca	Cr
1d	raw cts. Z	10	12	5	15	1
	wtd. cts. Z	8.94	11.9	5.00	14.4	0.50
	raw cts. Si	165	165	131	120	116
	wtd. cts. Si	161.	161.	127.	116.	112.
	Z/Si	$.0557^{+.0243}_{-.0179}$	$.0740^{+.0289}_{-.0219}$	$.0395^{+.0271}_{-.0176}$	$.125^{+.043}_{-.034}$	$.0045^{+.0104}_{-.0039}$
1e	raw cts. Z	28	39	12	62	12
	wtd. cts. Z	28.0	38.5	12.0	60.4	12.1
	raw cts. Si	456	456	409	390	384
	wtd. cts. Si	450.	450.	404.	385.	379.
	Z/Si	$.0621^{+.0144}_{-.0120}$	$.0855^{+.0166}_{-.0142}$	$.0297^{+.0114}_{-.0086}$	$.157^{+.024}_{-.021}$	$.0320^{+.0123}_{-.0093}$
3	raw cts. Z	5	9	4	11	1
	wtd. cts. Z	5.00	9.00	4.00	10.5	1.00
	raw cts. Si	121	121	92	88	83
	wtd. cts. Si	121.	121.	92.4	88.4	83.4
	Z/Si	$.0412^{+.0283}_{-.0183}$	$.0742^{+.0348}_{-.0253}$	$.0433^{+.0348}_{-.0214}$	$.119^{+.050}_{-.038}$	$.0120^{+.0279}_{-.0105}$
5	raw cts. Z	51	44	15	34	8
	wtd. cts. Z	49.7	44.3	15.0	34.0	8.28
	raw cts. Si	558	558	419	379	372
	wtd. cts. Si	552.	552.	413.	373.	366.
	Z/Si	$.0900^{+.0150}_{-.0131}$	$.0802^{+.0145}_{-.0125}$	$.0363^{+.0122}_{-.0095}$	$.0912^{+.0181}_{-.0163}$	$.0227^{+.0113}_{-.0080}$
7a	raw cts. Z	69	79	12	33	6
	wtd. cts. Z	69.5	77.4	12.0	33.3	6.00
	raw cts. Si	794	794	658	608	596
	wtd. cts. Si	782.	782.	646.	596.	584.
	Z/Si	$.0889^{+.0125}_{-.0111}$	$.0990^{+.0130}_{-.0117}$	$.0186^{+.0071}_{-.0054}$	$.0559^{+.0118}_{-.0100}$	$.0103^{+.0062}_{-.0041}$
7b	raw cts. Z	328	476	93	234	53
	wtd. cts. Z	313.	457.	92.7	233.	53.0
	raw cts. Si	5764	5765	4830	4524	4418
	wtd. cts. Si	5646.	5647.	4712.	4406.	4300.
	Z/Si	$.0555^{+.0033}_{-.0031}$	$.0809^{+.0040}_{-.0039}$	$.0197^{+.0023}_{-.0021}$	$.0530^{+.0038}_{-.0036}$	$.0123^{+.0019}_{-.0017}$
7c	raw cts. Z	232	263	21	69	16
	wtd. cts. Z	228.	259.	21.3	68.2	16.0
	raw cts. Si	2837	2838	2111	1877	1796
	wtd. cts. Si	2817.	2819.	2092.	1858.	1777.
	Z/Si	$.0811^{+.0059}_{-.0055}$	$.0918^{+.0063}_{-.0059}$	$.0102^{+.0028}_{-.0022}$	$.0367^{+.0051}_{-.0045}$	$.0090^{+.0029}_{-.0022}$

Table 4.4 (continued).

Flare		Na	Al	Ar	Ca	Cr
17	raw cts. Z	190	267	40	131	29
	wtd. cts. Z	177.	255.	39.7	127.	28.8
	raw cts. Si	2964	2965	2512	2369	2322
	wtd. cts. Si	2865.	2867.	2414.	2271.	2224.
	Z/Si	$.0617^{+.0049}_{-.0048}$	$.0889^{+.0060}_{-.0057}$	$.0165^{+.0031}_{-.0026}$	$.0558^{+.0054}_{-.0050}$	$.0129^{+.0029}_{-.0024}$
20	raw cts. Z	21	21	2	7	1
	wtd. cts. Z	19.0	20.5	2.00	7.00	1.00
	raw cts. Si	260	260	212	199	197
	wtd. cts. Si	257.	257.	209.	196.	194.
	Z/Si	$.0740^{+.0205}_{-.0187}$	$.0798^{+.0222}_{-.0180}$	$.0096^{+.0127}_{-.0064}$	$.0358^{+.0195}_{-.0135}$	$.0052^{+.0120}_{-.0045}$
24	raw cts. Z	14	12	1	2	2
	wtd. cts. Z	14.0	11.5	1.00	1.04	2.00
	raw cts. Si	82	82	69	61	61
	wtd. cts. Si	80.5	80.5	67.5	59.5	59.5
	Z/Si	$.174^{+.084}_{-.060}$	$.143^{+.057}_{-.044}$	$.0148^{+.0345}_{-.0129}$	$.0174^{+.0233}_{-.0117}$	$.0336^{+.0449}_{-.0226}$

the appropriate time, energy and charge interval by all operating LET and HET telescopes on both spacecraft, and "weighted counts," the sum of the PHA events after they have been multiplied by the geometry factor-livetime weighting factors described in Section 3.5 and listed in Appendix F. The raw event counts determine the statistical uncertainty in the abundances, while the corrected event counts give the abundance ratios themselves. Fig. 4.6 shows the abundance relative to Si of the abundant elements C, N, O, Ne, Mg, and Fe, for each of the 22 flare periods. For each abundance ratio, the different flares are ordered by the O/Si ratio. Table 4.4 and Fig. 4.7 provide the corresponding data for five elements of intermediate abundance (Na, Al, Ar, Ca and Cr) for each of the ten large flare events in the Voyager data set for which statistically meaningful abundances can be determined for these elements.

The abundances for the seven flare events 1d, 1e, 3, 5, 7a, 7b and 7c may be compared with those obtained by Cook et al. (1980, 1984) for the same flares using a subset of the present data set. The number of particles counted has been increased by a factor of ~7 - 11 depending on the flare, due primarily to the lower energy threshold used (5.0 vs. 8.7 MeV/nucleon), and, to a lesser extent, the selection of a longer time period for many flares, the inclusion of data from additional telescopes, and a higher high-energy cutoff (45 vs. 15 MeV/nucleon). This results in a significant improvement in precision over the earlier work. Most of the abundances agree to within ~20% with the values obtained by Cook et al. (1980, 1984), although a few differ by as much as 60%. More important, however, is that even the smaller differences in many cases are larger than the statistical uncertainty of the measurement. These differences can be accounted for by differences in time period and energy interval selection combined with velocity dispersion and spectral differences between elements in a given flare, as noted in Section 4.1.2.

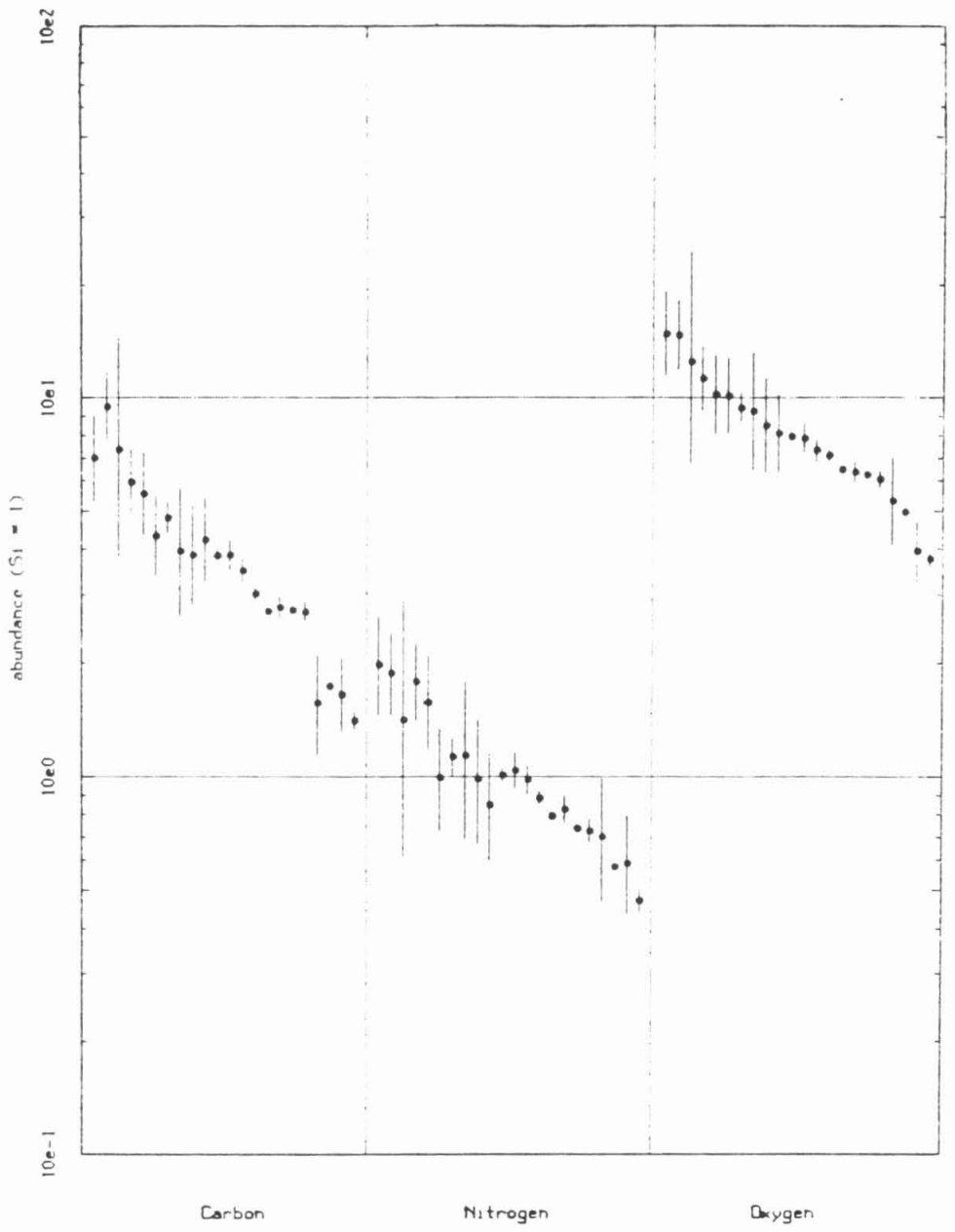

Fig. 4.6. Abundances of C, N, O, Ne, Mg, S and Fe with respect to Si in the 22 individual flare events in the Voyager CRS data set. The flares are ordered by the O/Si ratio.

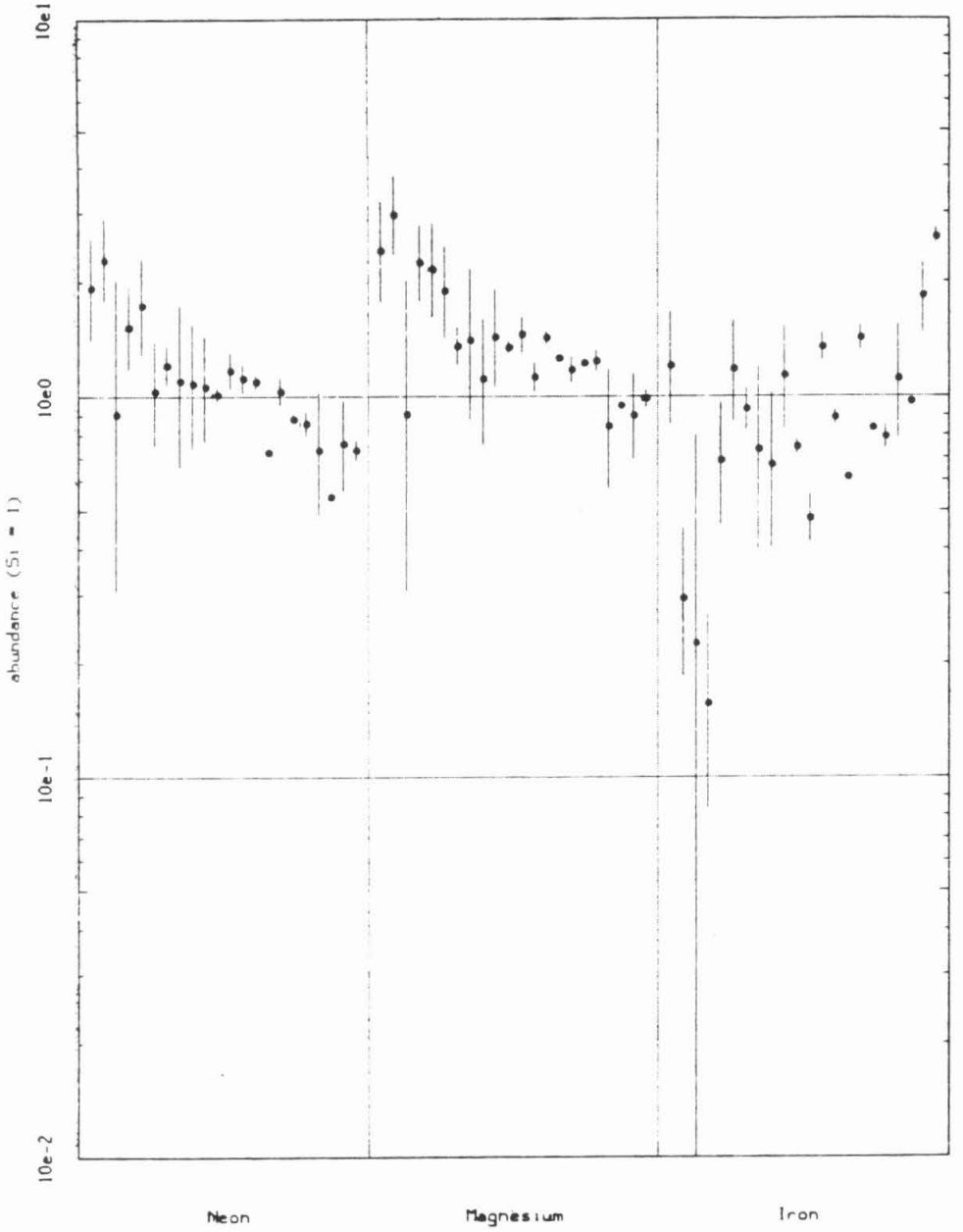

Fig. 4.6 (continued).

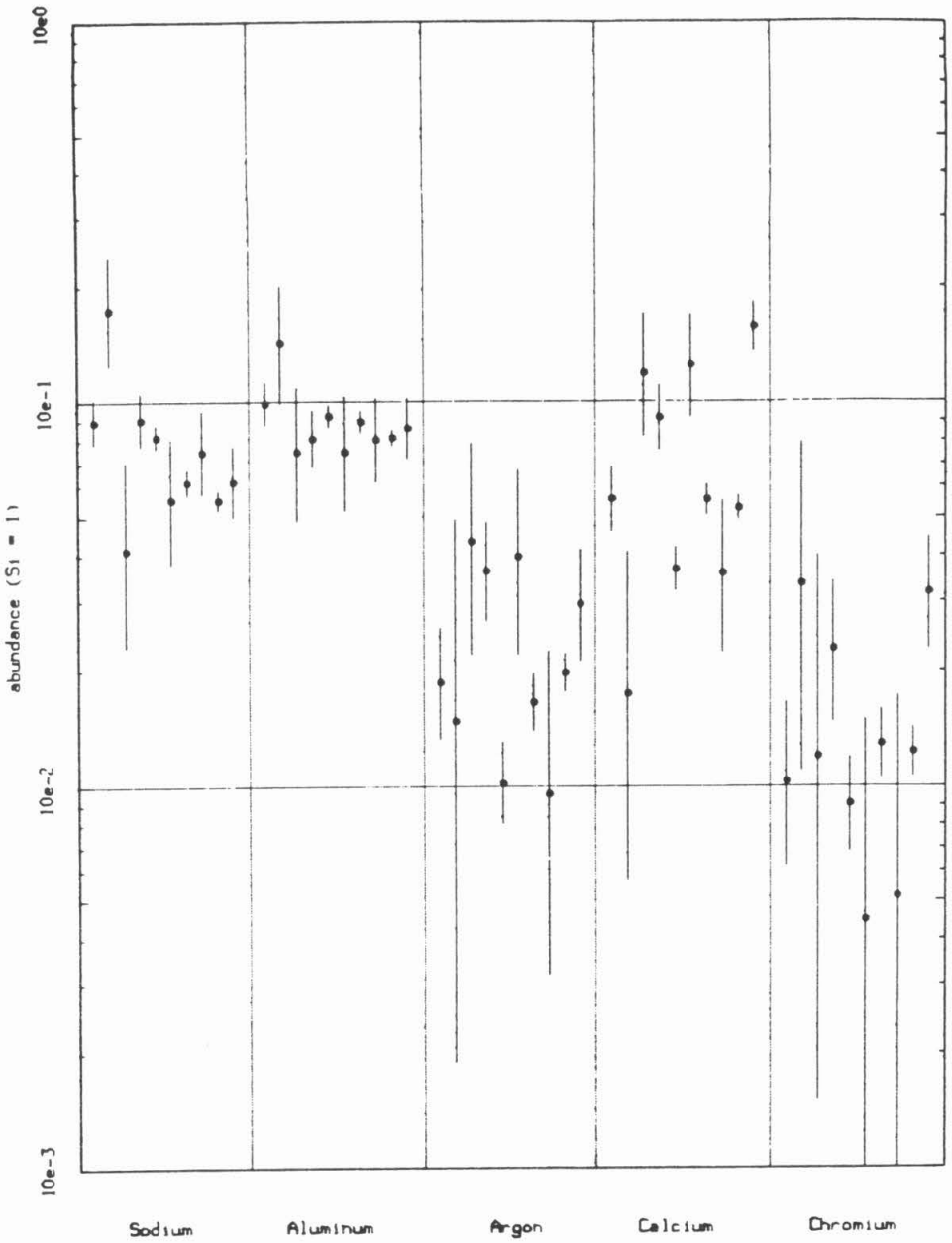

Fig. 4.7. Abundances of the five elements of intermediate abundance (Na, Al, Ar, Ca, Cr) in each of the 10 largest flare events. These are the only flares in the data set for which useful abundance figures can be obtained for this group of elements. As in Fig. 4.6, the flares are ordered by their O/Si ratio.

4.3 Average SEP Elemental Abundances

4.3.1 Determining the Average Abundance and its Uncertainty

As was noted in Section 4.1.1, the value of a given elemental ratio varies significantly between different flares, a situation that can be seen clearly in Table 4.3 and Fig. 4.6. It was argued that this property could be explained by variable acceleration and/or propagation fractionation effects. The systematic properties of the flare-to-flare variability will be taken up in Section 4.4; for now we are concerned only with the effect this variability has on the determination of average SEP abundances. The high degree of variability has been the source of much of the skepticism concerning the utility of SEP measurements in obtaining accurate solar composition information. However, the high variability in SEP composition reported in the past can be partly attributed to (1) poor particle counting statistics in individual flares, (2) the lack of an accurate characterization of the flare population distribution that gives rise to the flare-to-flare variability in composition, due in many cases to the small number of flares observed, and (3) considering only the abundances of all elements with respect to a fixed standard such as silicon or oxygen, which leads to a wide variability in abundance for elements far from the normalizing element on the charge scale (e.g., Fe) on account of the monotonic Q/M-dependent fractionation. This last point can be illustrated by noting that one consequence of a monotonic Q/M-dependent variability is that ratios of elements that are near neighbors on the charge scale show a much narrower range of variability than ratios of elements that are widely separated. For example, although the Fe/Si ratio in different flares varies over a range of an order of magnitude, ratios of neighboring elements, such as C/N or N/O, are much less variable. In fact, as Fig. 4.8 shows, the SEP composition is remarkably constant from one flare to another when expressed in terms of the ratios of adjacent (or as nearly adjacent as possible) elements. The average values of near-neighbor element ratios are thus much more precisely determined than the average values of widely-

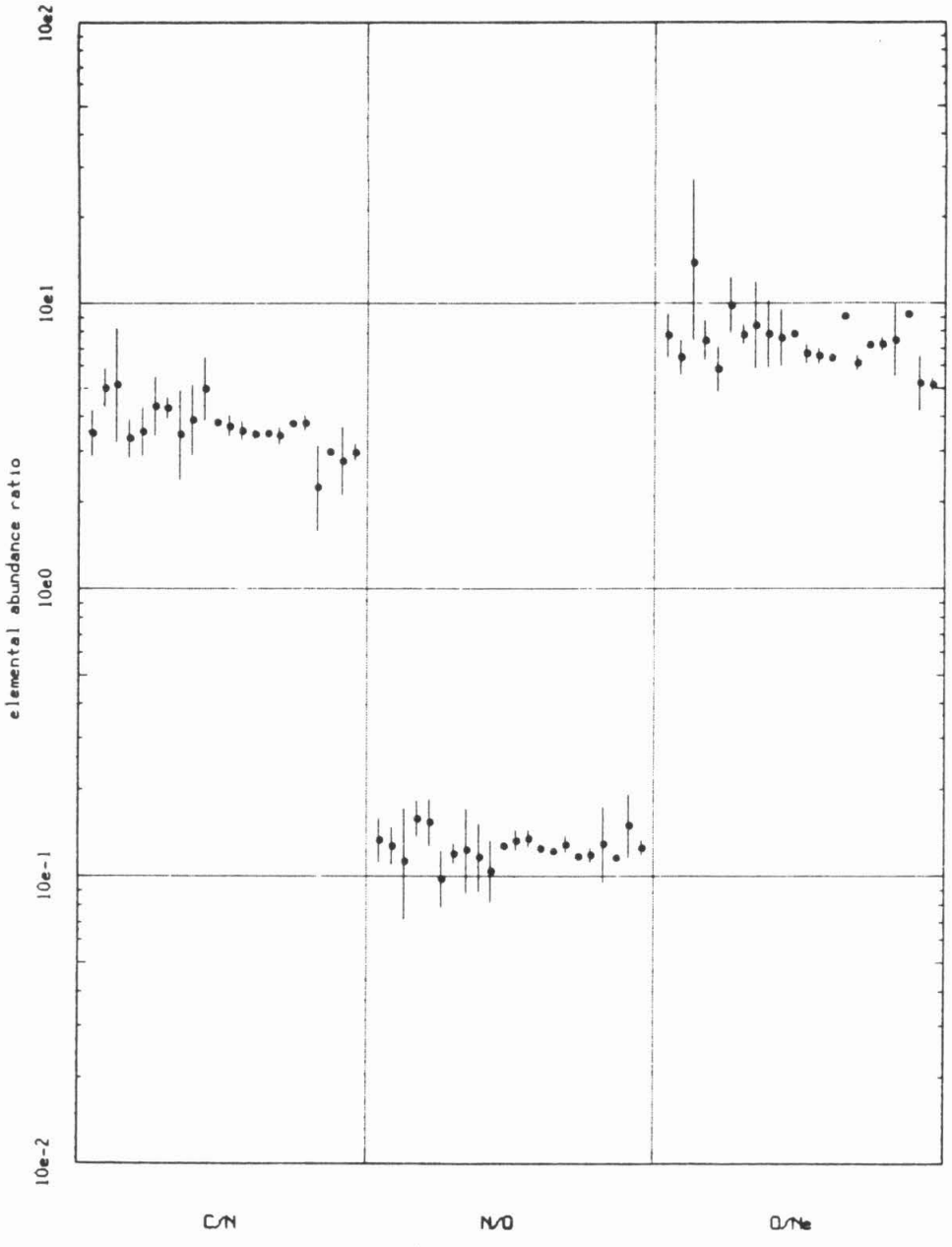

Fig. 4.8. Various abundance ratios of elements which are near neighbors on the charge scale, for individual flare events. This illustrates the tendency for neighboring-element ratios to show much less flare-to-flare variability than ratios of widely-separated elements (compare Figs. 4.6, 4.7).

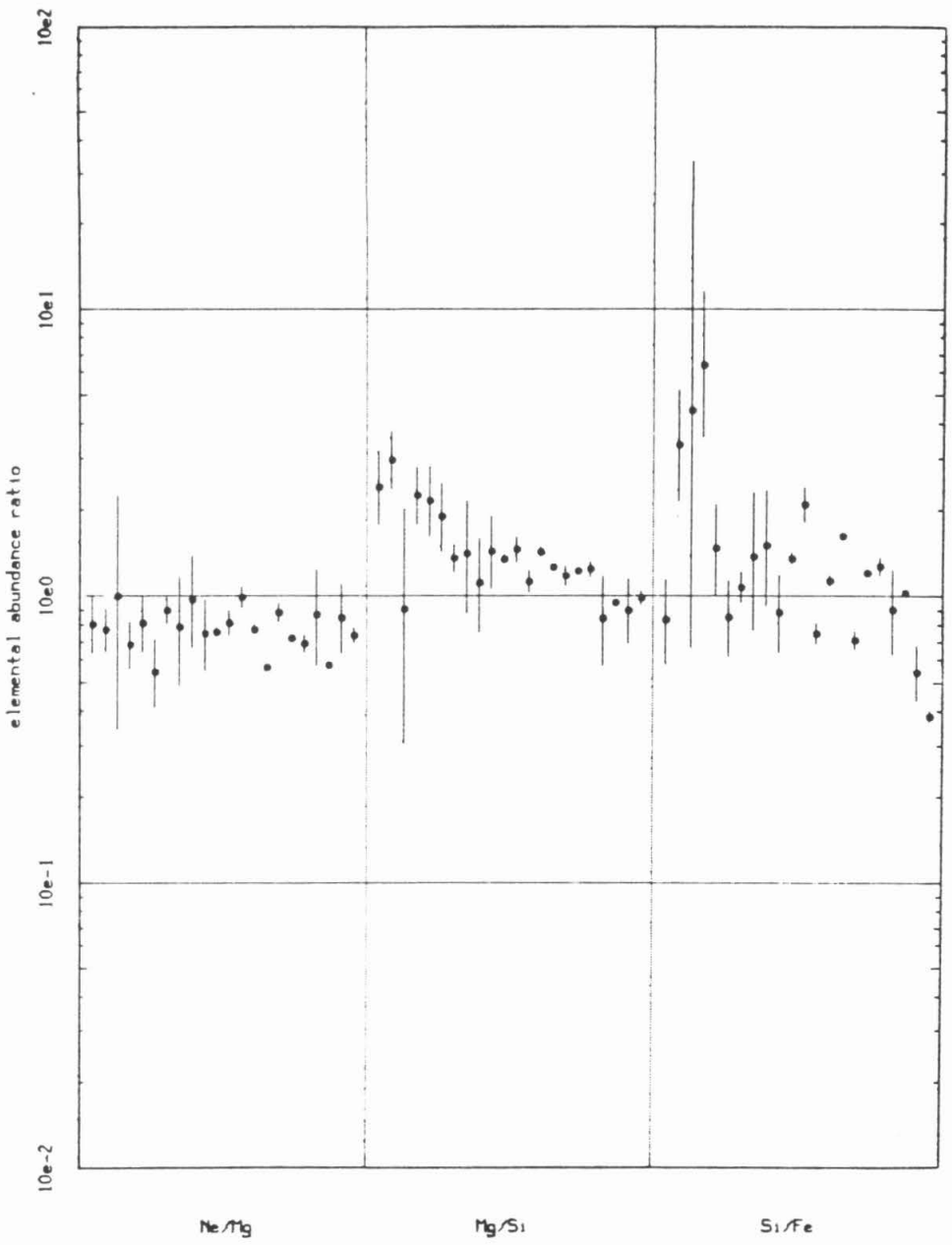

Fig. 4.8 (continued).

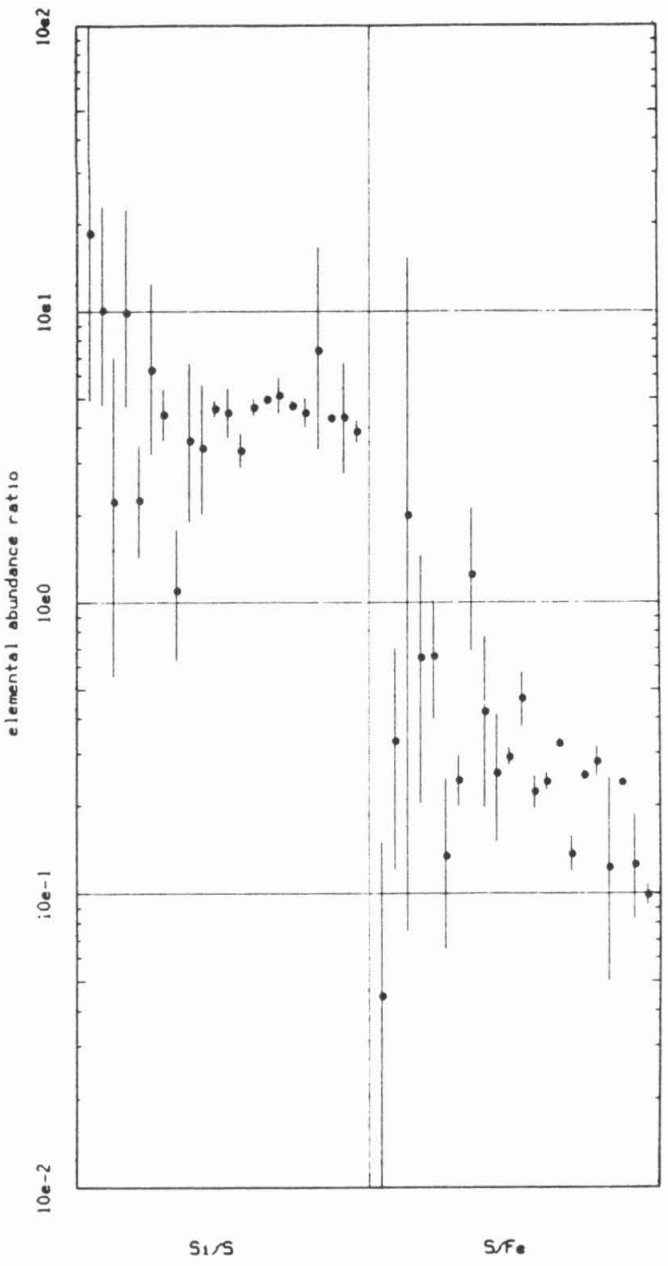

Fig. 4.8 (continued).

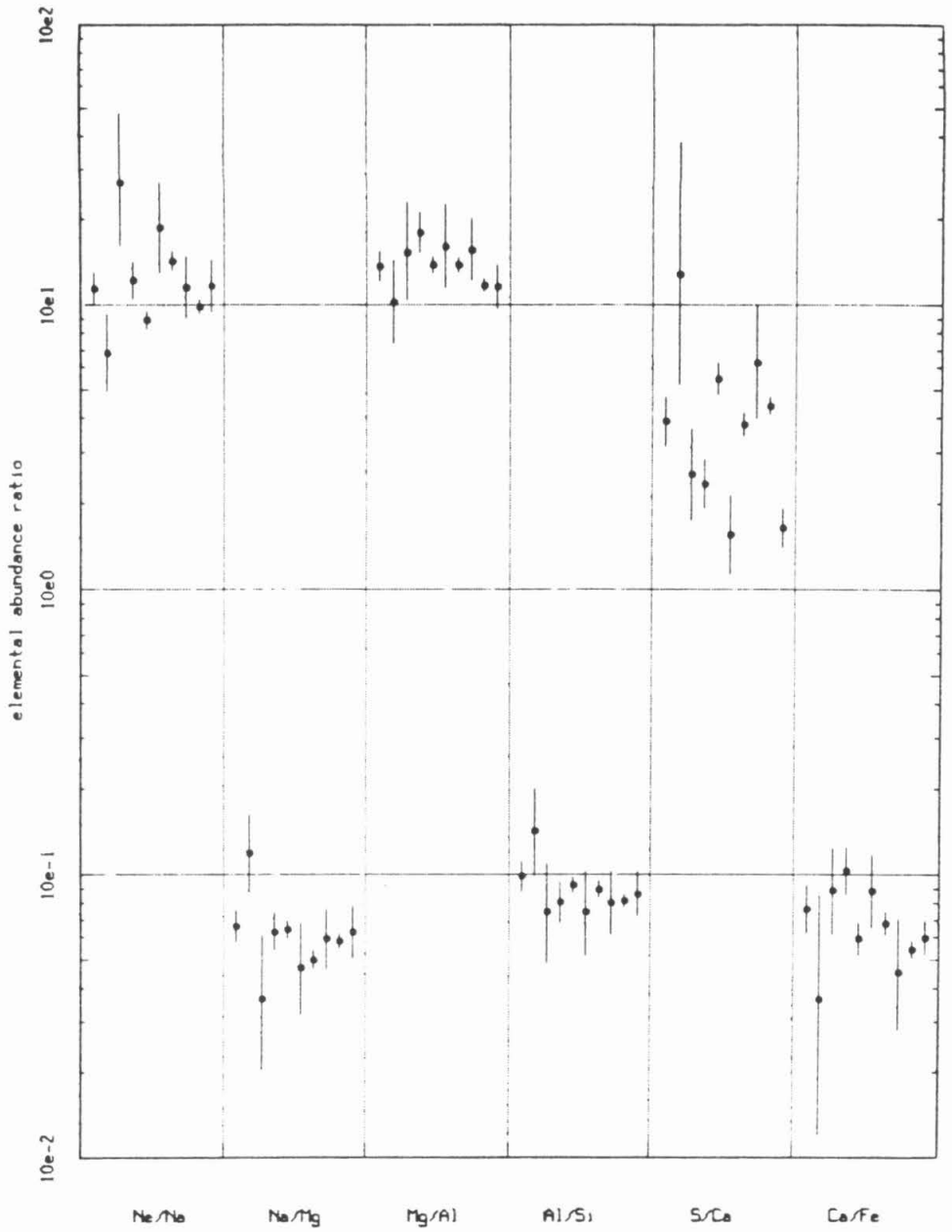

Fig. 4.8 (continued).

separated element ratios. However, if one requires the abundances of all elements relative to a fixed standard, the flare-to-flare variability becomes more important and a large statistical sample of flares, with good statistical accuracy in each, is essential to accurately characterize this variability. The present data set meets these conditions for the more abundant elements. However, since both statistical and real variation are present to differing degrees in the data set, some care must be taken in the method of calculating the mean value and uncertainty of the elemental ratios.

The best value and uncertainty of a particular abundance ratio may be characterized by a mean μ and uncertainty of the mean σ_μ, respectively, of the distribution of the ratio values for the different flares and applying either "weighted" and "unweighted" statistics, i.e., by either weighting each abundance ratio determination by its uncertainty or by treating all determinations equally. In what follows N is the number of flares, the x_i are the *logarithms* of the abundance ratios, so all mean values are log averages or "geometric means," and all uncertainties represent *factors* of error derived from particle counting statistics. The use of log averages is appropriate not only because of the wide range of values exhibited by some of the ratios, but because a power-law fractionation (as by rigidity) in individual flares will retain the same mathematical form in the averaged abundances.

The unweighted mean and standard deviation of a set of N values x_i are given by

$$\mu = \frac{1}{N}\sum_i x_i \qquad\qquad \sigma = \frac{1}{N-1}\sqrt{\sum_i x_i^2 - N\mu^2} \tag{4.5}$$

The uncertainty of the mean is given by

$$\sigma_\mu = \frac{\sigma}{\sqrt{N}} \tag{4.6}$$

If flare i is weighted by its statistical uncertainty $\sigma_{stat,i}$, the weighted mean and its uncertainty are given by

$$\mu = \frac{\sum_i \frac{x_i}{\sigma^2_{stat,i}}}{\sum_i \frac{1}{\sigma^2_{stat,i}}} \tag{4.7}$$

$$\sigma_\mu = \frac{1}{\sqrt{\sum_i \frac{1}{\sigma^2_{stat,i}}}} \tag{4.8}$$

The weighted σ of the distribution is given by

$$\sigma = \sigma_\mu \chi \tag{4.9}$$

where

$$\chi^2 = \sum_i \frac{(x_i - \mu)^2}{\sigma^2_{stat,i}} \tag{4.10}$$

For a data set of the present type, neither the weighted nor the unweighted method of averaging is completely satisfactory, on account of the presence of systematic (non-statistical) variation between flares, and the fact that the data points have individual uncertainties ranging from very much less than, to somewhat greater than, the width of the overall population distribution. The unweighted mean and standard deviation (Eqs. 4.5, 4.6) are reasonable if the data points have uncertainties that are essentially equal (or at least small compared to the population distribution width). In fact, many small flares have large uncertainties which tend to make this distribution width estimate too large and may bias the mean. On the other hand, the statistical weighting method (Eqs. 4.7, 4.8) gives almost no weight at all to the small flares, producing a width estimate and mean value close to what one would obtain by considering only the few largest flare events. Furthermore, it fails to account for the presence of real variation in the distribution of values, i.e., it treats the data as if the only variation is statistical. As was pointed out in Section 4.2, this is far from the case for the present data set. The result is that the largest flares may bias the mean value and the uncertainty obtained is unrealistically low. To

treat data in which real (non-statistical) variation is present, and in which the statistical precision of individual points ranges from negligible to comparable to the real variation, a hybrid weighting was adopted that has the correct properties in the two limiting cases of pure statistical variation and pure population variation. The weighted mean and standard deviation were applied, but using weighting factors that include uncertainties due both to statistics of the individual data point and the variation in the parent population. Thus Eqs. 4.7 and 4.8 are used but with the statistical uncertainty $\sigma_{stat,i}$ replaced by the total uncertainty $\sigma_{tot,i}$ given by

$$\sigma_{tot,i}^2 = \sigma_{stat,i}^2 + \sigma_{pop}^2 \tag{4.11}$$

where $\sigma_{stat,i}$ is the uncertainty in the ratio for flare i due to particle counting statistics, and σ_{pop} is the width of the parent population distribution. The latter quantity is approximated by Eq. 4.9, in which only statistical weights are used in the calculation of μ and χ. The modified weighting allows new values of μ, χ and σ_{pop} to be calculated, and the procedure is repeated iteratively until it converges on a self-consistent value of μ. In practice, for the present data set, the convergence is rapid, and in fact the final iterated μ differs by at most a few percent from the initial estimate obtained from the first weighting using Eq. 4.11 with σ_{pop} derived from statistical weighting only. However, the μ values obtained using Eq. 4.11 generally differ significantly from those obtained using statistical weighting. Nevertheless, the procedure used here is considered superior because it takes satisfactory account of the presence of real variability, while not permitting the poorly-determined ratios from the smaller flares to bias the result and enlarge the uncertainty. It has the correct values in the limiting cases; if statistical variation is negligible ($\sigma_{stat,i} \ll \sigma_{pop}$ for all i), it reduces to Eqs. 4.5 and 4.6, and if the only variation present is statistical, it reduces to Eqs. 4.7 and 4.8.

If this technique is applied to the full set of 22 flares for the abundant element ratios, one finds, by comparing σ_{pop} to $\sigma_{stat,i}$ for the individual flares, that

generally only a subset of the flares are statistically significant in the sense of having $\sigma_{stat,i} < \sigma_{pop}$. The remaining flares only add to the uncertainty in μ and provide little information on σ_{pop}, and it is advantageous to exclude them. The number of flares meeting this condition varies depending on the counting statistics and σ_{pop} for the ratio in question, but is typically about 11 (if the flares are ordered by number of particles observed, there is a sharp dropoff between the largest 11 flares and the next smaller ones).

The combined-variance-weighted ratios were used to construct the ratios to silicon of all of the relatively abundant elements, but using only the ten largest flares in the averaging process. This flare set (flares 1d, 1e, 3, 5, 7a, 7b, 7c, 17, 20, and 24) was chosen because (1) for most abundant-element ratios it approximates the set of statistically significant flares and (2) it coincides with the set of flares for which abundances could be determined for the elements of intermediate abundance, eliminating a need for any corrections to this group of elements relative to the other group.

All of the mean ratio determinations described above (flares unweighted, flares weighted by statistical variance only, and both 10-flare and 22-flare combined statistical and population variance weighting) for the ratios to silicon of the elements of high abundance are listed in Table 4.5. It can be seen from the table that the unweighted flare mean tends to closely approximate the 22-flare combined-variance-weighted mean (usually within 1σ), since the combined-variance weighting tends to roughly equalize the weights of all flares, despite the gross differences in statistical precision between flares reflecting orders-of-magnitude differences in the number of analyzed particles. The weights in the combined-variance-weighted case range over only about a factor of 2 or 3, since the statistical uncertainty of the abundant-element ratios for the smallest flares is on the order of the population width for the ratio, and the combined weight for the large flares is approximately this value since the statistical contribution is negligible for these flares. However, both of these averages differ significantly from the statistically-weighted mean and the 10-flare

Table 4.5. Average ratios of the more abundant heavy elements to silicon, calculated in five ways from the data in Tables 4.3 and 4.4: particle average (PA); unweighted flare average (UW); statistically-weighted flare average (SW); average of all 22 flares (for the more abundant elements only) weighted by combined statistical and population variances (SPW); and a combined-variance weighting of the 10 largest flares only (SPWL). The mean and uncertainty for UW were obtained using Eqs. 4.5 and 4.6 respectively, and the SW mean and uncertainty using Eqs. 4.7 and 4.8 respectively. The mean and uncertainty for SPW and SPWL also resulted from Eqs. 4.7 and 4.8, but with the statistical variance replaced by the combined statistical and population variances (Eq. 4.11). Uncertainty on the PA is the statistical uncertainty on the number of PHA counts in all flares combined. For PA, UW and SW, the ten largest flares only were used for Na, Al, Ar, Ca and Cr; for all other elements, all 22 flares were used. The relative uncertainties quoted on the ratios of the various means to SPWL are the relative uncertainty on SPWL. The SPWL means and uncertainties were used as the final determinations of these elemental abundance ratios. The maximum-likelihood abundances of the very rare elements were corrected to correspond to the SPWL means for the more abundant elements by interpolating between the values of PA/SPWL for the more abundant elements.

ratio	PA	UW	SW	SPW	SPWL	PA/SPWL	UW/SPWL	SW/SPWL	SPW/SPWL
C/Si	2.49 ± 0.02	$3.54^{+0.41}_{-0.37}$	2.42 ± 0.02	$3.39^{+0.37}_{-0.33}$	$2.71^{+0.27}_{-0.24}$	$0.918^{+0.091}_{-0.083}$	$1.307^{+0.130}_{-0.118}$	$0.893^{+0.089}_{-0.081}$	$1.252^{+0.124}_{-0.113}$
N/Si	0.723 ± 0.007	$0.972^{+0.084}_{-0.077}$	0.719 ± 0.007	$0.916^{+0.076}_{-0.070}$	$0.775^{+0.054}_{-0.051}$	$0.933^{+0.065}_{-0.061}$	$1.254^{+0.087}_{-0.082}$	$0.928^{+0.065}_{-0.061}$	$1.181^{+0.082}_{-0.077}$
O/Si	6.00 ± 0.04	$7.74^{+0.64}_{-0.59}$	5.90 ± 0.04	$7.26^{+0.50}_{-0.47}$	$6.23^{+0.36}_{-0.34}$	$0.964^{+0.056}_{-0.053}$	$1.243^{+0.072}_{-0.068}$	$0.948^{+0.055}_{-0.052}$	$1.165^{+0.066}_{-0.064}$
Ne/Si	0.750 ± 0.007	$1.05^{+0.08}_{-0.07}$	0.746 ± 0.007	$1.03^{+0.11}_{-0.10}$	$0.887^{+0.091}_{-0.083}$	$0.846^{+0.087}_{-0.079}$	$1.182^{+0.122}_{-0.110}$	$0.841^{+0.087}_{-0.078}$	$1.160^{+0.119}_{-0.108}$
Na/Si	.0664 ± .0022	$.0726^{+.0096}_{-.0081}$	$.0673^{+.0024}_{-.0023}$		$.0733^{+.0072}_{-.0066}$	$0.906^{+0.089}_{-0.081}$	$0.990^{+0.098}_{-0.089}$	$0.917^{+0.090}_{-0.082}$	
Mg/Si	1.16 ± 0.01	1.36 ± 0.10	1.15 ± 0.01	$1.32^{+0.08}_{-0.07}$	1.21 ± 0.06	$0.959^{+0.051}_{-0.049}$	$1.130^{+0.060}_{-0.057}$	$0.953^{+0.051}_{-0.048}$	$1.097^{+0.058}_{-0.056}$
Al/Si	.0862 ± .0026	$.0881^{+.0056}_{-.0052}$	$.0863^{+.0027}_{-.0026}$		$.0874^{+.0043}_{-.0041}$	$0.986^{+0.049}_{-0.046}$	$1.008^{+0.050}_{-0.047}$	$0.987^{+0.049}_{-0.046}$	
S/Si	0.220 ± 0.003	$0.219^{+0.028}_{-0.025}$	0.220 ± 0.003	$0.225^{+0.009}_{-0.008}$	$0.222^{+0.008}_{-0.007}$	$0.989^{+0.034}_{-0.033}$	$0.988^{+0.034}_{-0.033}$	$0.993^{+0.034}_{-0.033}$	$1.014^{+0.035}_{-0.034}$
Ar/Si	.0183 ± .0013	$.0209^{+.0039}_{-.0033}$	$.0193^{+.0015}_{-.0014}$		$.0207^{+.0035}_{-.0030}$	$0.885^{+0.150}_{-0.128}$	$1.010^{+0.171}_{-0.146}$	$0.932^{+0.158}_{-0.135}$	
Ca/Si	.0569 ± .0024	$.0617^{+.0148}_{-.0116}$	$.0600^{+.0027}_{-.0026}$		$.0684^{+.0115}_{-.0098}$	$0.832^{+0.140}_{-0.120}$	$0.902^{+0.151}_{-0.130}$	$0.880^{+0.148}_{-0.126}$	
Cr/Si	.0128 ± .0011	$.0126^{+.0030}_{-.0024}$	$.0134^{+.0014}_{-.0012}$		$.0143^{+.0029}_{-.0024}$	$0.893^{+0.179}_{-0.149}$	$0.881^{+0.177}_{-0.147}$	$0.937^{+0.188}_{-0.157}$	
Fe/Si	0.885 ± 0.008	$0.795^{+0.119}_{-0.103}$	0.884 ± 0.008	$0.934^{+0.081}_{-0.074}$	$0.959^{+0.105}_{-0.094}$	$0.922^{+0.101}_{-0.091}$	$0.829^{+0.090}_{-0.082}$	$0.922^{+0.100}_{-0.091}$	$0.974^{+0.106}_{-0.096}$

combined-variance-weighted mean, both of which reflect the composition of the larger flares. The latter two differ somewhat from each other since the statistical weighting yields highly unequal weights, even within the group of largest flares, while the combined-variance-weighting of this group is virtually an unweighted average since the statistical uncertainties of these flares are negligible compared to the population variance.

Also shown in the table is a "particle average" abundance obtained by simply summing the observed PHA events in all flare periods. Since the larger flares contribute the most particles to the sum, this average also emphasizes data from the large flares and produces abundances and uncertainties close to those of the statistically-weighted flare mean. Although the particle-average μ and σ were not used in the final abundance determinations for the abundant elements, it is important to examine the degree to which this weighting scheme differs from the adopted one for various elemental ratios in order to relate these abundances to the abundance determinations for the rarest elements, which are by necessity equivalent to particle averages. Like the statistically-weighted flare mean, the particle average is often significantly below the combined-variance-weighted mean. This implies the need for an upward correction averaging about 5 percent to the particle-average abundances for the very rare elements. The required correction, obtained by interpolation or extrapolation in Z from the measured values for the more abundant elements, is typically a few percent and at worst about 20 percent, generally small compared to the statistical uncertainty for the elements in question.

Also evident in Table 4.5 is an effect apparent in Fig. 4.6, that the large flares tend to have relatively low values of Z/Si for $Z < 14$ and the small flares relatively high values. It can be seen that the statistically-weighted mean ratio tends to be lower than the unweighted mean, since it emphasizes the larger flares. The combined-variance-weighted means tend to be in between, since they also emphasize the large flares but to a lesser degree. This effect can also be seen by comparing the combined-variance weighting of all 22 flares with the

same weighting of just the 10 largest flares. This effect may be due to a tendency for smaller flares to be more highly fractionated than larger flares.

The quantitative evaluations of the flare-to-flare variability described above are also used to estimate the total uncertainty for the very rare elements. A contribution due to flare-to-flare variation must be combined with the statistical uncertainty determined by the maximum-likelihood fitting procedure. The contribution is estimated from the combined-variance-weighted iterated population widths σ_{pop} for the abundant elements, interpolated or extrapolated in Z; this is not an unreasonable estimate since this measure of flare-to-flare variability is a relatively smooth function of Z. This number was converted to an estimate of the uncertainty of the mean σ_{μ} for the rare elements by dividing by $\sqrt{N_{eff}}$, where N_{eff} is the effective number of flares that contribute to the data set for that element. Although all 22 flares contribute in principle, only the few largest do in practice on account of the poor statistics of the rare elements and the great inequality between the flares in their particle contribution to the total data set. For many rare elements the estimate of the flare-to-flare variability is negligible compared to the statistical uncertainty.

In Table 4.6 are shown the combined-variance weighted average values for several ratios of elements which are near neighbors on the charge scale. When compared with Table 4.5, this illustrates how the neighboring-element ratios show a much lower population variance than ratios of widely separated elements. While the ratios of C and Fe to Si are uncertain by 10 percent, the ratios of elements separated by one or two charge units are typically uncertain by only about 5 percent.

Although some individual flares have significant energy-dependence to their abundances, essentially all of this dependence averages out when the combined-variance weighted mean is calculated. This was shown by comparing the mean Fe/Si ratios calculated using lower-energy thresholds of 5 and 8 MeV/nucleon. The resulting mean values (0.96 and 0.98) differ by ~2.5%. Thus

Table 4.6. Average neighboring-element ratios of the more abundant heavy elements, calculated from the data in Table 4.4 using the method of combined statistical and population variance weighting of flares described in Section 4.3.1. The mean and uncertainty were obtained from Eqs. 4.7 and 4.8, but with the statistical variance replaced by the combined statistical and population variance (Eq. 4.11).

ratio	combined-variance weighted mean
C/N	$3.48^{+0.12}_{-0.11}$
N/O	0.123 ± 0.002
O/Ne	$7.04^{+0.46}_{-0.43}$
Ne/Mg	$0.731^{+0.046}_{-0.044}$
Mg/Si	1.21 ± 0.06
Si/Fe	$1.04^{+0.11}_{-0.10}$
Ne/Na	$11.3^{+1.0}_{-0.9}$
Na/Mg	0.060 ± 0.004
Mg/Al	$13.4^{+0.8}_{-0.7}$
Al/Si	0.087 ± 0.004
Si/S	4.50 ± 0.15
S/Ca	$3.29^{+0.51}_{-0.44}$
Ca/Fe	0.067 ± 0.006

Table 4.7. Average SEP abundances relative to Si for the more abundant elements with $3 \leq Z \leq 30$, compared to other published SEP composition measurements: Mason et al. (1980) and Cook et al. (1984), and the "mass-unbiased baseline" of Meyer (1985), an interpolation between SEP abundances obtained by several different investigative groups. Uncertainties on the Cook et al. SEP measurements, like those on the present SEP results, include the effects of both particle counting statistics and of the flare-to-flare variability, and also, where important, the effects of finite charge resolution and instrumental background. Figures in parentheses are factors of uncertainty.

Z	this work	Cook et al. (1984)	"mass-unbiased baseline" Meyer (1985)	Mason et al. (1980)
6	2710. (1.099)	2740. (1.335)	2900. (1.30)	4200. (1.44)
7	775. (1.070)	700. (1.253)	810. (1.33)	
8	6230. (1.058)	5800. (1.250)	6500. (1.13)	8300. (1.33)
10	887. (1.103)	970. (1.089)	840. (1.32)	1330. (1.40)
11	73.3 (1.099)	70. (1.429)	85. (1.47)	
12	1206. (1.053)	1200. (1.165)	1230. (1.28)	1250. (1.41)
13	87.4 (1.049)	100. (1.194)	89. (1.55)	
14	1000.	1000.	1000. (1.37)	1000.
16	222. (1.034)	200. (1.175)	200. (1.80)	
18	20.7 (1.170)	30. (1.845)	38. (1.70)	$670._{-300.}^{+330}$
20	68. (1.168)	120. (1.288)	76. (1.55)	
24	14.3 (1.201)	20. (1.782)	22.5 (1.90)	
26	959. (1.109)	1140. (1.327)	990. (1.47)	$1170._{-730.}^{+850.}$
28	33.8 (1.155)	60. (1.503)	45. (1.75)	

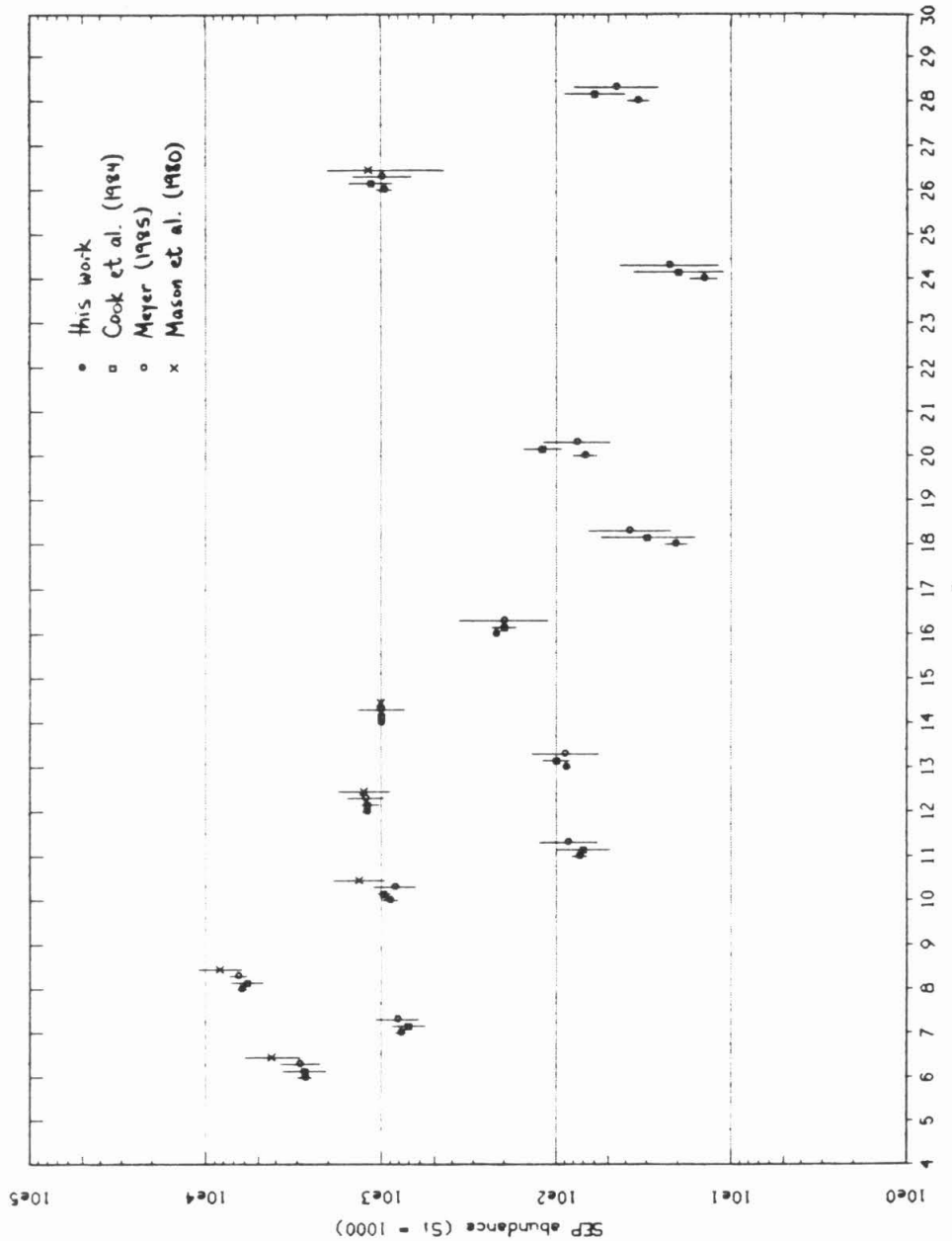

Fig. 4.9. SEP composition results from the present work for the more abundant elements, compared to other recent SEP composition measurements. The present results are in generally excellent agreement with earlier results but have approximately three times higher precision.

the mean abundances of the elements of intermediate abundance (Na, Al, Ar, Ca, Cr), obtained using the higher energy threshold, will not be biased relative to the more abundant elements by energy-dependence of individual flare abundances.

4.3.2 Comparison With Other SEP Composition Measurements

The average SEP abundances relative to silicon obtained for the most abundant elements in the charge range $3 \leq Z \leq 30$ are listed in Table 4.7. Included are abundances relative to silicon obtained for Ni by the maximum-likelihood procedure of Section 3.6 and the combined statistical- and population-variance-weighted average ratios obtained for the abundant elements by the procedures of Sections 3.5 and 4.3.1. In the table and in Fig. 4.9 these abundances are compared to several other recent SEP composition determinations. The quoted uncertainties on the SEP measurements represent the effects of counting statistics, finite charge resolution, instrumental background, and flare-to-flare variability of the abundances.

The SEP composition measurements of Cook et al. (1980, 1984) were derived from Voyager LET data for a four-flare subset of the present flare set. It can be seen that the two sets of SEP abundances agree with each other to within the uncertainty, strengthening the belief that the present flare sample is large enough and representative enough to provide a meaningful average SEP composition determination. The present results show average values close to Cook et al. for the light elements, and slightly lower for the heavier elements. This can be interpreted as a manifestation of the monotonic Q/M-dependent flare-to-flare variability, which allows the mean abundance determined from an average of four flares to be systematically different from an average of 10 flares, in this case a slight systematic enhancement of the heavier elements. Nevertheless, the difference is within the measurement uncertainty, indicating that it can be accounted for purely the limited number of flares in the data sets. More important is the reduction in uncertainty, typically by a factor of

three, resulting from the larger number of flares in the new data and the increased number of particles counted in individual flares. For the most abundant elements (C, O, Ne, Mg, Si, S-Ca, and Cr-Ni), the present results also agree well with those obtained by Mason et al. (1980) at somewhat lower energies (~1 MeV/nucleon) for flares during the 1973-1977 time period, again with greatly improved precision.

The present results agree to within uncertainty with the "mass unbiased baseline" (Meyer 1981, 1985), obtained as an interpolation within a combined set of SEP measurements obtained by several different investigative groups. Since this baseline is not an "average" SEP composition in any sense, but rather an attempt to find a SEP composition which is unfractionated (apart from the first ionization potential effect), this agreement only shows that the average of the present observations is a composition close to solar system (or photospheric) composition in general, a result in agreement with the earlier results of Meyer. In the earlier work the mass-unbiased baseline was arrived at by finding a SEP composition, within the continuum of observed compositions, for which the Mg, Si and Fe were fractionated relative to the photospheric values in a way that depends smoothly on FIP. This attempted to remove any Z-dependent fractionation of the coronal particles, since these three elements have similar low first ionization potentials and therefore should not be fractionated from the photosphere during the formation of the corona. In Section 4.5, a more systematic attempt will be made to perform this correction by fitting all of the well-determined abundances of elements with low first ionization potentials as a function of their charge-to-mass ratio.

It should be noted that in constructing the mass unbiased baseline, a "local galactic" Fe abundance of 0.88 ± 0.06 relative to Si (Meyer 1979), based on both meteoritic and photospheric data, was used. This value is some 33% lower than the most recent photospheric value of 1.320 ± 0.045 (Grevesse 1984). It is primarily the Fe abundance that determines the mass unbiased baseline, since Mg shows comparatively little variation with Si from flare to flare. If the more

recent Fe value is accurate, then the similarity between the present SEP average abundances and the mass unbiased baseline primarily reflects the similarity between the Meyer (1979) local galactic Fe abundance and the raw SEP average obtained here (0.96 ± 0.10) and is essentially coincidental. It is also coincidental if the lower Fe abundance is correct, and the average SEP composition has no overall non-FIP fractionation. However, in Section 4.5, results based on the present data will be presented as evidence of significant fractionation of the average SEP composition by Q/M, and arguments will be developed in support of the higher Fe abundance.

4.3.3 Comparison With Other Elemental Abundance Standards

The average SEP abundances relative to silicon obtained for all of the elements in the charge range $3 \leq Z \leq 30$ are listed in Table 4.8 and plotted vs. Z in Fig. 4.10. Included are abundances relative to silicon obtained for the rare elements by the maximum-likelihood procedure of Section 3.6 and the combined statistical- and population-variance-weighted average ratios obtained for the abundant elements by the procedures of Sections 3.5 and 4.3.1. It can be seen that the abundances measured span four orders of magnitude, and that finite abundances as opposed to upper limits are obtained for all elements with $6 \leq Z \leq 30$ except F, Sc, V, Co and Cu. (For Li, Be, and B, one-sigma upper limits are quoted; these elements are known to be very rare in the sun, and although some events are seen in this region of the charge scale, they are likely due to a small uniform instrumental background in this region of the charge scale). The uncertainties quoted here include both (1) the measurement uncertainty due to particle counting statistics, background contamination and finite charge resolution, and (2) the uncertainty in the true average abundance due to variability in abundance between the different flares in a finite flare sample. The relative importance of the two contributions depends on the particular element. For elements of high abundance and far from Si on the charge scale, such as C, N, O and Fe, contribution (2) is dominant, while for P, a relatively

Table 4.8. Average SEP abundances relative to Si for elements with $3 \leq Z \leq 30$, compared to other published types of elemental composition measurements: abundances from the "solar system" compilation of Anders & Ebihara (1982), abundances from C1 and C2 type carbonaceous chondrites (Meyer 1978), photospheric abundances from Grevesse (1984), two sets of coronal composition measurements (Meyer and Reeves (1977) and Veck and Parkinson (1981)), the solar abundance compilation of Ross and Aller (1976) derived from a variety of measurements, and solar wind abundances inferred from abundances relative to hydrogen and helium in Bochsler and Geiss (1976). The uncertainties on the SEP results include both the effect of particle counting statistics and the effect of the flare-to-flare variability, and also, where important, the effects of finite charge resolution and instrumental background. Uncertainties on the Meyer meteoritic abundances represent the spread in the measurements, while the uncertainties in the meteoritic abundances of Anders and Ebihara are uncertainties of the mean. Figures in parentheses are factors of uncertainty.

Z	SEP this work	"Solar System" Anders and Ebihara (1982)	Carbonaceous Chondrites (Meyer 1978) C1	Carbonaceous Chondrites (Meyer 1978) C2	Photosphere Grevesse (1984)	Ross and Aller (1976)	Corona Meyer and Reeves (1977)	Veck and Parkinson (1981)	Solar Wind Bochsler and Geiss (1976)
3	< 1.36	$.0597 \pm .0009$	0.060 ± 0.002	0.052 ± 0.003	0.00028	$.00022^{+.00006}_{-.00005}$			
4	< 0.17	$.00078 \pm .00003$	$.00090 \pm .00035$	$.00090 \pm .00035$	0.00040	$.00032^{+.00018}_{-.00012}$			
5	< 0.34	0.024 ± 0.001	0.053 ± 0.023	0.030 ± 0.015	0.011	$0.0028^{+0.0017}_{-0.0010}$			
6	$2710.^{+270}_{-240}$	$12100. \pm 3630.$			13800.	$9300.^{+3000}_{-2250}$	7000. (2)		
7	$775.^{+54}_{-51}$	$2480. \pm 992.$			2750.	$1950.^{+800}_{-570}$	$2000. \pm 800.$		
8	$6230.^{+360}_{-340}$	$20100. \pm 4020.$			$22900. \pm 500.$	$15500.^{+2700}_{-2300}$	12000. (2)	6020.	$6600. \pm 3700.$
9	$(0.29^{+0.29}_{-0.29})$*	0.843 ± 0.048	0.93 ± 0.2	0.57 ± 0.20	1.02	$0.81^{+0.93}_{-0.43}$			
10	$887.^{+91}_{-85}$	$3760. \pm 1128.$			2800.	$830.^{+265}_{-200}$	$1500. \pm 700.$	950.	$1000. \pm 500.$
11	$73.3^{+7.2}_{-6.6}$	57.0 ± 1.0	$60. \pm 4.$	$35. \pm 6.$	60.3 ± 2.1	$42.7^{+5.2}_{-4.6}$	60. (1.6)	68.	
12	$1206.^{+84}_{-81}$	$1075. \pm 10.$	$1050. \pm 30.$	$1050. \pm 30.$	$1070. \pm 60.$	$890.^{+370}_{-260}$	$1000. \pm 300.$	950.	
13	$87.4^{+4.3}_{-4.1}$	84.9 ± 1.0	$84. \pm 4.$	$84. \pm 4.$	83.	$74.^{+24}_{-18}$	70. (2)		
14	1000.	$1000. \pm 14.$	$1000. \pm 30.$	$1000. \pm 30.$	$1000. \pm 60.$	$1000.^{+200}_{-170}$	1000.	1000.	1000.
15	$4.78^{+0.64}_{-0.70}$	10.4 ± 0.5	9.6 ± 1.5	7.9 ± 1.0	7.9	$7.1^{+2.9}_{-2.1}$			
16	$222.^{+8}_{-7}$	$515. \pm 30.$	$500. \pm 80.$	$215. \pm 20.$	$460. \pm 30.$	$355.^{+150}_{-100}$	300. (2)	170. (2.1)	
17	$2.01^{+0.63}_{-0.62}$	5.24 ± 0.25	4.7 ± 1.0	2.1 ± 0.5	9.	$7.1^{+10.7}_{-4.3}$			
18	$20.7^{+3.5}_{-3.0}$	$104. \pm 21.$			107.	$22.4^{+13.1}_{-8.3}$	170. (3)	50. (2.4)	$24. \pm 13.$
19	$2.95^{+1.01}_{-0.93}$	3.77 ± 0.06	3.7 ± 0.5	2.2 ± 0.4	3.7 ± 0.6	$3.24^{+0.84}_{-0.67}$			
20	$68.^{+12}_{-10.}$	61.1 ± 1.1	$64. \pm 10.$	$64. \pm 10.$	64.6 ± 1.5	$50.^{+13}_{-10}$		70. (2.2)	
21	$(0.22^{+0.36}_{-0.22})$*	$.0338 \pm .0008$	0.035 ± 0.005	0.035 ± 0.005	0.035	$0.0245^{+0.0043}_{-0.0037}$			
22	$3.5^{+1.4}_{-1.1}$	2.40 ± 0.05	2.7 ± 0.4	2.7 ± 0.4	2.95	$2.51^{+0.80}_{-0.61}$			
23	$(0.34^{+0.48}_{-0.34})$*	0.295 ± 0.005	0.26 ± 0.05	0.26 ± 0.05	0.28	$0.234^{+0.097}_{-0.069}$			
24	$14.3^{+2.9}_{-2.4}$	13.4 ± 0.3	13.0 ± 1.2	13.0 ± 1.2	13.2 ± 0.5	$11.5^{+4.4}_{-3.2}$			
25	$5.0^{+2.7}_{-1.9}$	9.51 ± 0.23	9.3 ± 1.3	6.2 ± 0.2	7.9	$5.9^{+2.8}_{-1.8}$			
26	$959.^{+105}_{-94}$	$900. \pm 6.$	$880. \pm 60.$	$880. \pm 60.$	$1320. \pm 45$	$710.^{+140}_{-120}$	$1000. \pm 400.$	950.	$700. \pm 500.$
27	< 13.5	2.25 ± 0.04	2.1 ± 0.3	2.1 ± 0.3	2.34 ± 0.11	$1.8^{+0.9}_{-0.6}$			
28	$33.6^{+6.0}_{-5.9}$	49.3 ± 0.6	$48. \pm 6.$	$48. \pm 6.$	50.1 ± 2.3	$43.^{+10}_{-8}$	50. (1.6)	54.	
29	$(0.40^{+0.64}_{-0.40})$*	0.514 ± 0.025	0.52 ± 0.08	0.39 ± 0.04	0.46 ± 0.02	$0.26^{+0.09}_{-0.07}$			
30	$1.09^{+0.92}_{-0.63}$	1.26 ± 0.01	1.35 ± 0.15	0.60 ± 0.10	1.12 ± 0.10	$0.63^{+0.26}_{-0.18}$			

* Abundances for these elements are based on fewer than 5 particles and are highly uncertain.

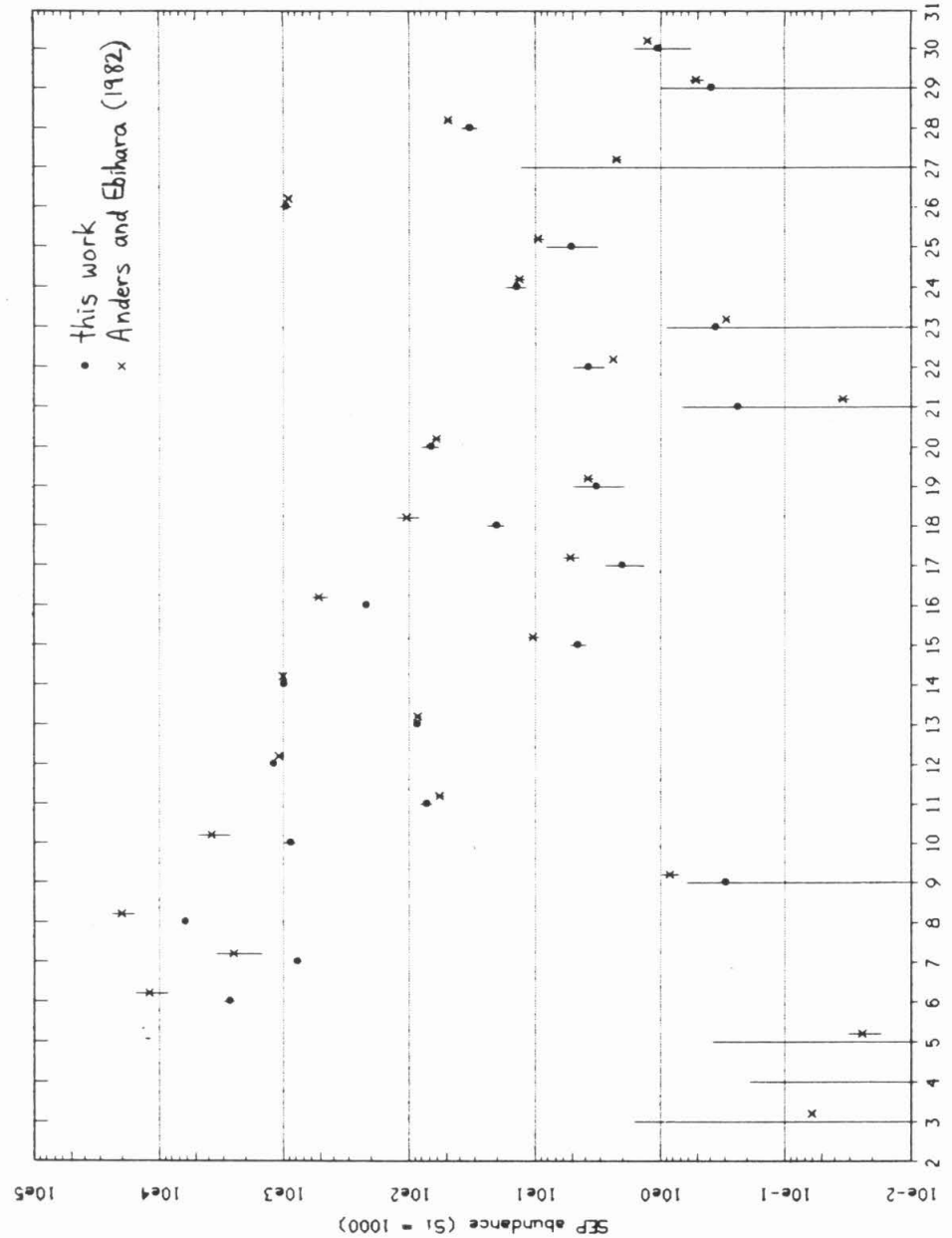

Fig. 4.10. SEP composition results from the present work for all elements with $3 \leq Z \leq 30$, compared to the "solar system" abundance compilation of Anders and Ebihara (1982). Finite abundances have been obtained for all elements in this charge range except Li, Be, B, F, Sc, V, Co and Cu.

rare element close to Si, contribution (1) is most important. For the abundant elements, the flare weighting scheme described in Section 4.3.1 incorporates the effects of both statistics and population variance; background and resolution difficulties are essentially nonexistent for these elements. For the rare elements, contribution (1) is taken to be the uncertainty derived from the maximum likelihood fitting procedure, which includes the effects of background and imperfect resolution as well as statistics. Contribution (2) was estimated for the rare elements by interpolation between the abundant element values as described in Section 4.3.1; for the rarest elements this contribution is insignificant compared to the statistical uncertainty. It should be noted that the magnitude of the flare-to-flare variation contribution is peculiar to the choice of Si for the abundance normalization.

In Table 4.8, the average SEP abundances from the present work are compared to solar elemental abundances obtained from several other independent sources: photospheric spectroscopy (Grevesse 1984), coronal spectroscopy including X-ray data (Veck and Parkinson 1981) and a compilation of both X-ray and extreme ultraviolet (XUV) data (Meyer and Reeves 1977), the solar wind (Bochsler and Geiss 1976), the solar abundance compilation of Ross and Aller (1976), carbonaceous chondrites (Meyer 1978), and the "solar system" compilation of Anders and Ebihara (1982), derived from a combination of meteoritic and solar and stellar composition data. The differences noted above between the different SEP abundance determinations are small compared to some of the differences with the other types of solar composition data, and to the uncertainties in these data. The present SEP results agree well with the coronal and solar wind abundances where these are available, although the major source of uncertainty is in the coronal (spectroscopic) or solar wind measurement. There is also good agreement with the values obtained from carbonaceous chondrites; more will be said later on the comparison with C1 and C2 type carbonaceous chondrites. Clear differences are seen between SEP composition and the photosphere and the differences are well-ordered by first ionization

potential (FIP), in agreement with earlier results (Cook et al. 1979, 1980, 1984; Meyer 1981, 1985). But this affects primarily the elements C, N, O, Ne and Ar, for which useful meteoritic data are lacking; most of the other elements agree well between photosphere and carbonaceous chondrites as well as with SEPs. For several relatively abundant heavy elements, such as Ca, Cr, and Fe, the present SEP results are in closer agreement with the meteoritic and photospheric values than are the Cook et al. (1980, 1984) SEP data.

The same pattern is present also in the comparison to the "solar system" compilation of Anders and Ebihara (1982), shown also in Fig. 4.10. This elemental abundance compilation was obtained principally from meteoritic abundances but also (in the case of the volatiles C, N, O, Ne and Ar) from astronomical measurements (solar wind, photospheric spectroscopy, spectroscopy of stars and interstellar gas). It is seen that for some elements the SEP and "solar system" measurements agree well, while in other cases the SEP abundance is significantly depleted with respect to the solar system abundance. Since the ionic charge state measurements (Gloeckler et al. 1981, Luhn et al. 1984) and compositional data (Cook et al. 1979, 1980, 1984) are consistent with SEPs originating at a typical coronal temperature $\sim 2 \times 10^6$ °K, and these properties are presumably present at the time of acceleration and not altered by propagation, we are led to models in which the material which forms the corona is extracted from the photosphere by a process that depends on FIP, and are subsequently accelerated from the corona by a process that depends on the ionization states present at the much higher coronal temperature.

The present results permit a test of the FIP ordering for a number of new, relatively rare elements in SEPs including F, P, Cl, K, Ti, Mn, and Zn. Fig. 4.11 shows the ratio of SEP to "solar system" abundance (Anders and Ebihara 1982) plotted versus first ionization potential for all elements with reasonably good SEP abundance values. The following observations can be made:

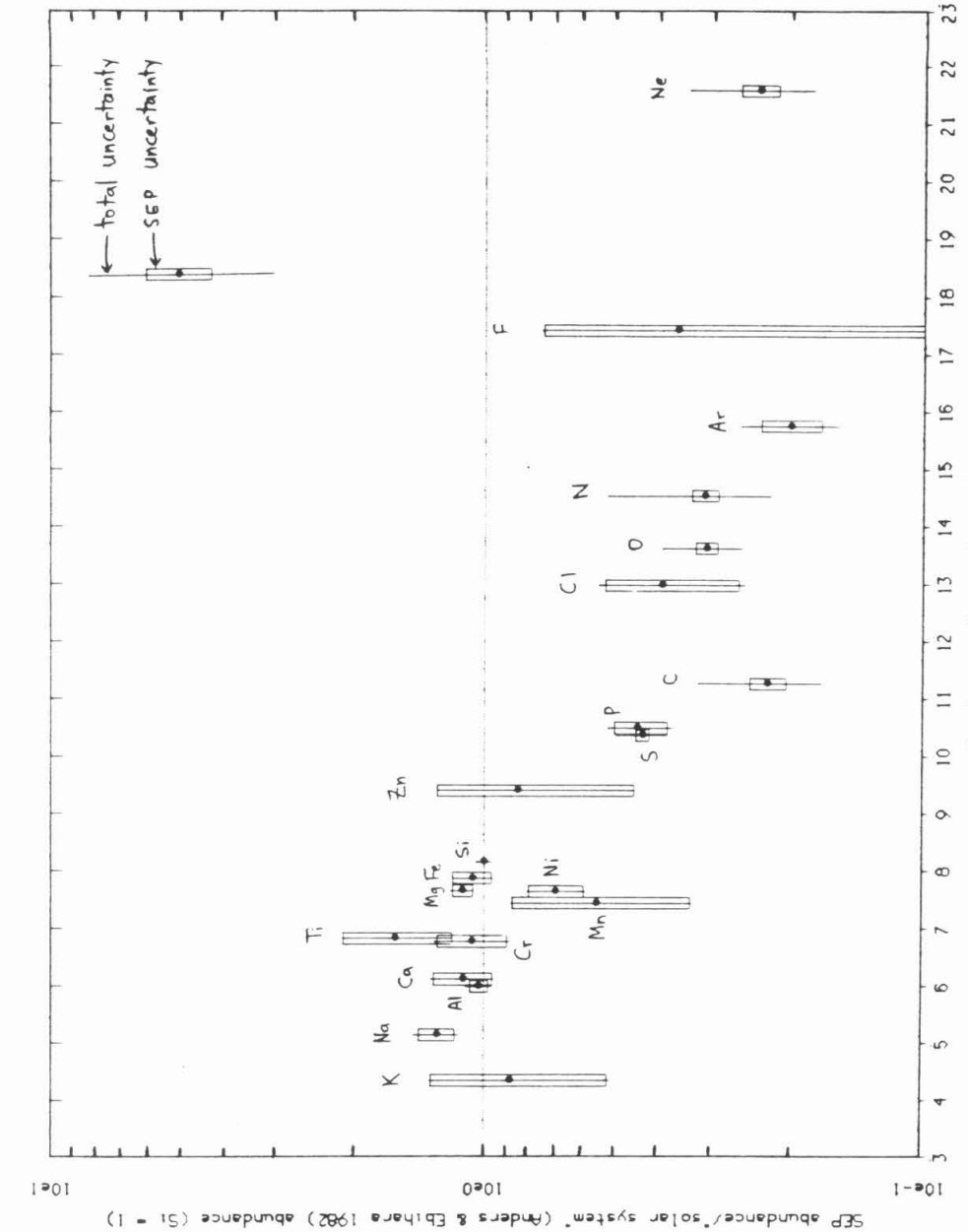

Fig. 4.11. Ratio of SEP abundances to the "solar system" compilation of Anders and Ebihara (1982), plotted vs. first ionization potential. "Total uncertainty" is the quadratic sum of the uncertainties in the SEP abundance and the abundance standard. Where no total uncertainty is shown, there is no published uncertainty for the abundance standard.

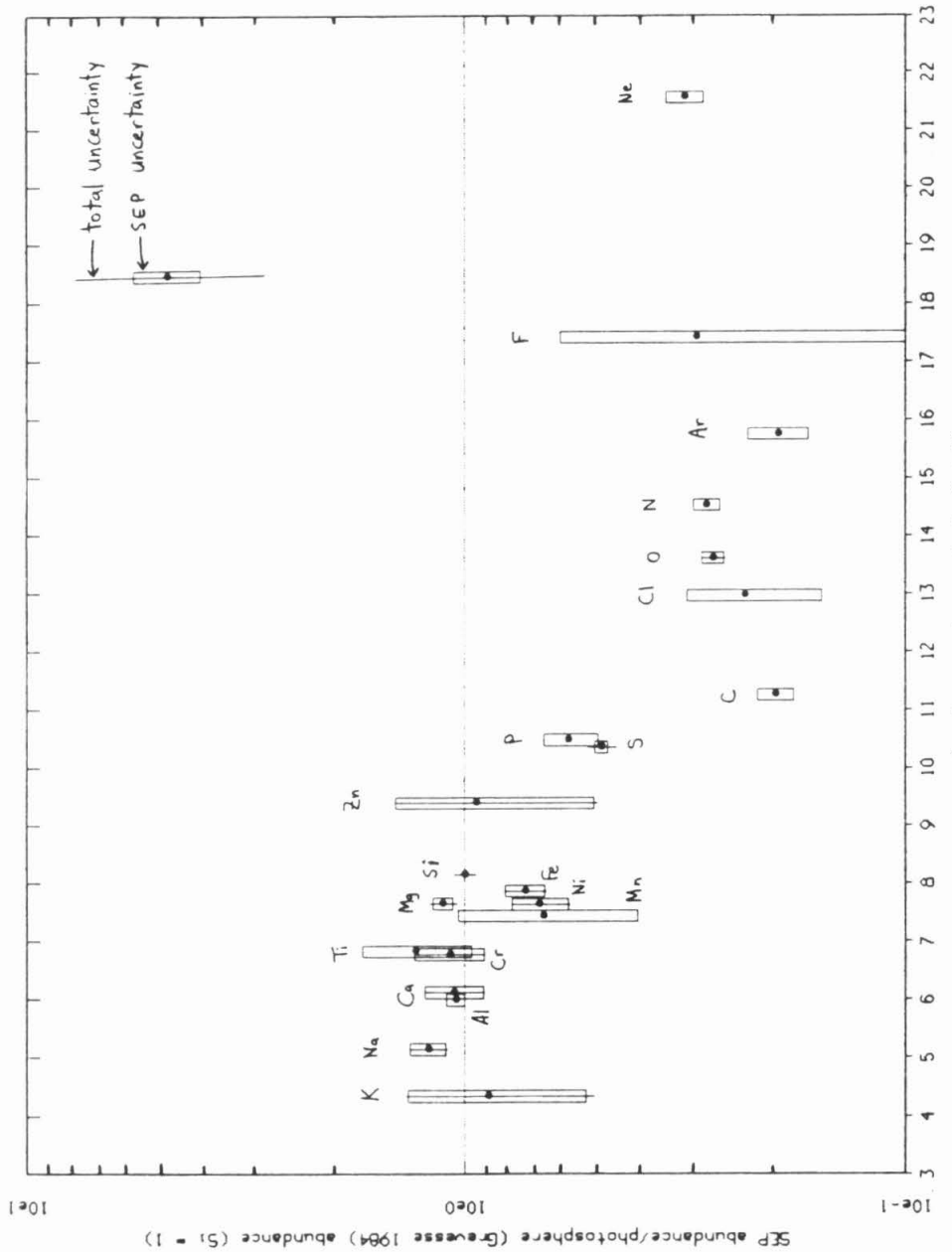

Fig. 4.12. Ratio of SEP abundances to the photospheric spectroscopic abundances of Grevesse (1984), plotted vs. first ionization potential. "Total uncertainty" is the quadratic sum of the uncertainties in the SEP abundance and the abundance standard. Where no total uncertainly is shown, there is no published uncertainty for the abundance standard.

(1) The FIP ordering previously observed for the more abundant elements (C, N, O, Ne, Na, Mg, Al, Si, S, Ca, Fe, Ni) is still apparent in the new abundance data presented here.

(2) The previously observed ordering continues to hold for most of the newly-measured elements, including F, P, Cl, Ti, and Zn.

(3) A few elements appear somewhat more depleted than would be expected based on FIP alone, notably Mn and Ni.

This pattern is repeated when the SEP data are compared to the photospheric composition data of Grevesse (1984) (Fig. 4.12). While the general pattern holds of equality for elements with FIP < 9 eV and depletion in SEPs by a factor of ~4 for high-FIP elements, there are a few exceptions, and an overall raggedness to the ordering which exceeds the probable errors in the SEP, "solar system" or photospheric data. This suggests that FIP is at least not the only important parameter in ordering the SEP/solar system deviations.

The plots of the SEP/"solar system" and SEP/photosphere abundance ratios vs. FIP (Figs. 4.11 and 4.12) also make it clear that there is no apparent correlation of the abundance ratio with Z; in fact, apart from the FIP-associated depletions the Z-dependence is remarkably flat. This is a somewhat surprising result in view of the pronounced composition differences between individual flares. As described in Section 4.2, the ratios of individual flare abundances to the average flare abundance show a monotonic Q/M-dependence whose magnitude and sign (relative to the average) is different for each flare. But yet that average abundance, obtained by combining the data from all 22 flares, is essentially equal to the "solar system" composition for all low-FIP Z. This is in accordance with the previous observation that the average SEP abundance is close to the "mass unbiased baseline" (Meyer 1981, 1985) since the latter was defined as a SEP composition which resembles as closely as possible the solar system/photospheric composition (apart from the FIP effect). Nevertheless, the organization is not perfect; there seems to be some residual

scatter in the data that may be interpreted in terms of acceleration-induced fractionation between the SEP particles and the true coronal composition. This possibility will be taken up in Section 4.5.

4.4 Systematics of Flare-to-Flare Variability

We next examine the systematic properties of the flare-to-flare variation, with the objective of understanding the source of this variability and what effect this may have on the determination of true coronal composition from the average SEP composition. In Fig. 4.6 the abundances relative to Si of C, N, O, Ne, Mg, and Fe in each of the 22 flare periods are ordered by the O/Si ratio. From this figure one notes the following:

(1) The range of variation between flares is least for Ne and Mg, and greatest for C and Fe. In general, the range of variation is proportional in some way to how far the element is from the normalizing element on the charge scale, with the widest distribution of values (up to an order of magnitude in range) occurring for the elements furthest from Si on the charge scale.

(2) Elements near each other on the charge scale correlate well with each other, and anticorrelate with elements on the opposite side of the normalizing element, in this case Si. Thus a flare which has a relatively low C/Si ratio tends also to have relatively low values of N/Si and O/Si, and a relatively high value of Fe/Si. Some of the apparent correlation in the smaller flares is a statistical artifact of the silicon normalization; if a particular flare has a relatively high O/Si ratio due to statistical fluctuation in the small number of silicon particles, other ratios such as C/Si and N/Si will also tend to be relatively high for the same reason, not necessarily because of a real correlation in the true abundance ratios.

(3) For any ratio showing wide variation, the larger flares (i.e., the best-determined abundance values) tend to be clustered near the center of the distribution, with the smaller flares mostly near the extremes of the distribution. This would be expected just on statistical grounds even if the well-determined and poorly-determined values sampled the same particle population. However, the important point is that the variability shown by the large flares is very large compared to the measurement uncertainties of the data points. Hence a large component of the observed variation is due to a real systematic effect and not merely statistical fluctuation. This also follows from point (2), since a purely statistical variation between flares would result in only random correlations between different abundance ratios.

(4) The flares with the poorest statistics appear to be asymmetrically distributed about the mean, with the majority of the small flares concentrated in the part of the distribution characterized by relatively high values of Z/Si for $Z < 14$ and low values of Z/Si for $Z > 14$. The possibility of this being an artifact of contamination of the smaller flares by non-flare particles has been minimized by the flare time period selection criteria described in Section 3.4; as mentioned in Section 4.3.1, this effect may indicate that the smaller flares tend to be more highly fractionated than the larger flares. The observation of C-rich, Fe-poor small flares is contrary to studies at lower energies (~1 MeV/nucleon), where Fe-rich flares are seen (Mason et al. 1979). However, these are very small flares compared to any of the flares in this study, and they are thought to involve other, more localized acceleration processes than the large-scale coronal shock acceleration considered here.

The observations above are consistent with a characteristic average SEP composition which is modified in individual flares by a roughly monotonic Z-dependent function whose magnitude and sign is different for different flares. This description is further supported when the elements of intermediate

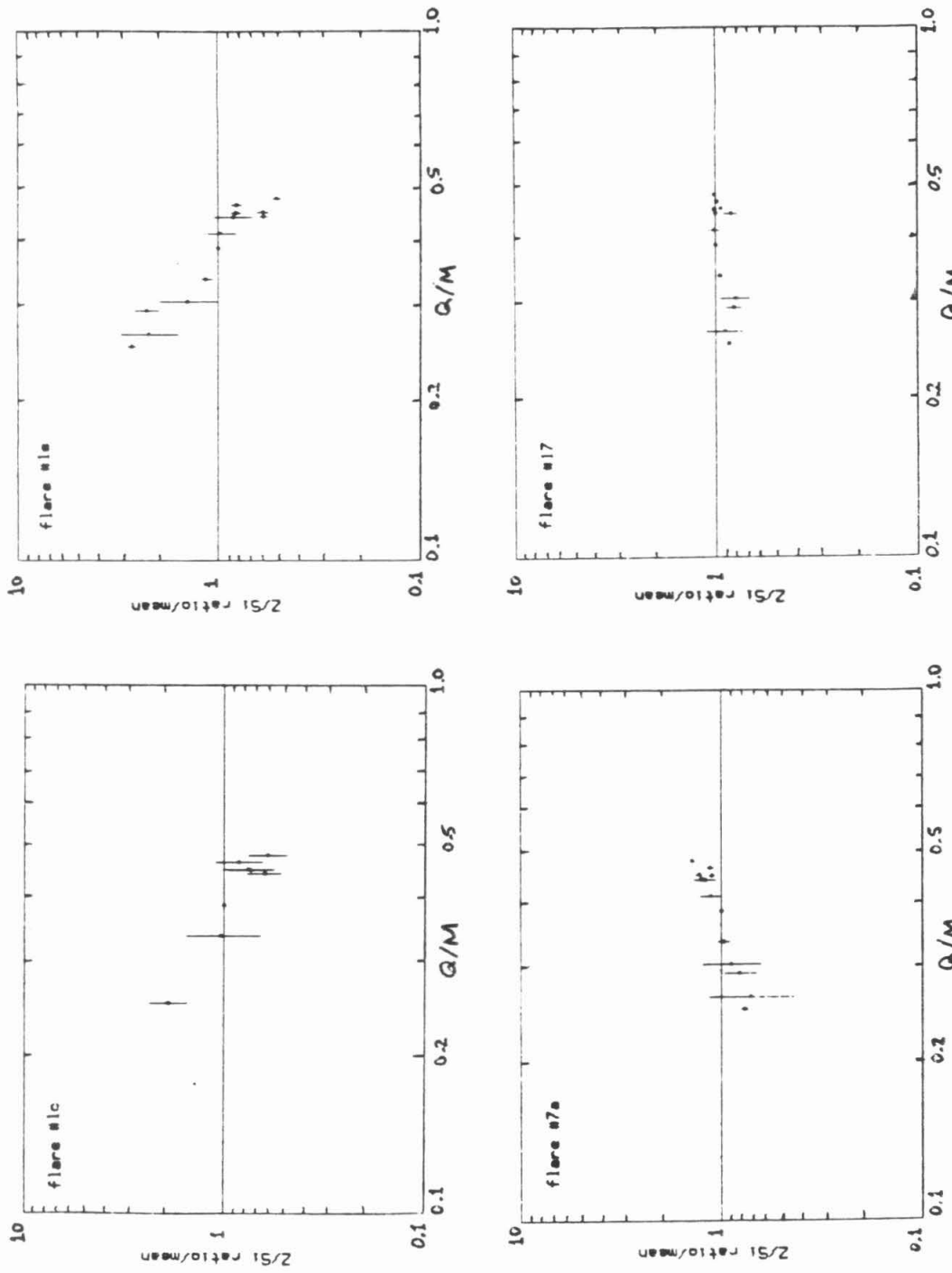

Fig. 4.13. Abundance ratios to Si relative to the mean ratio vs. mean Q/M for four representative flare events. The Q values were obtained from recent SEP ionic charge state measurements (Gloeckler et al. 1981, Luhn et al. 1984).

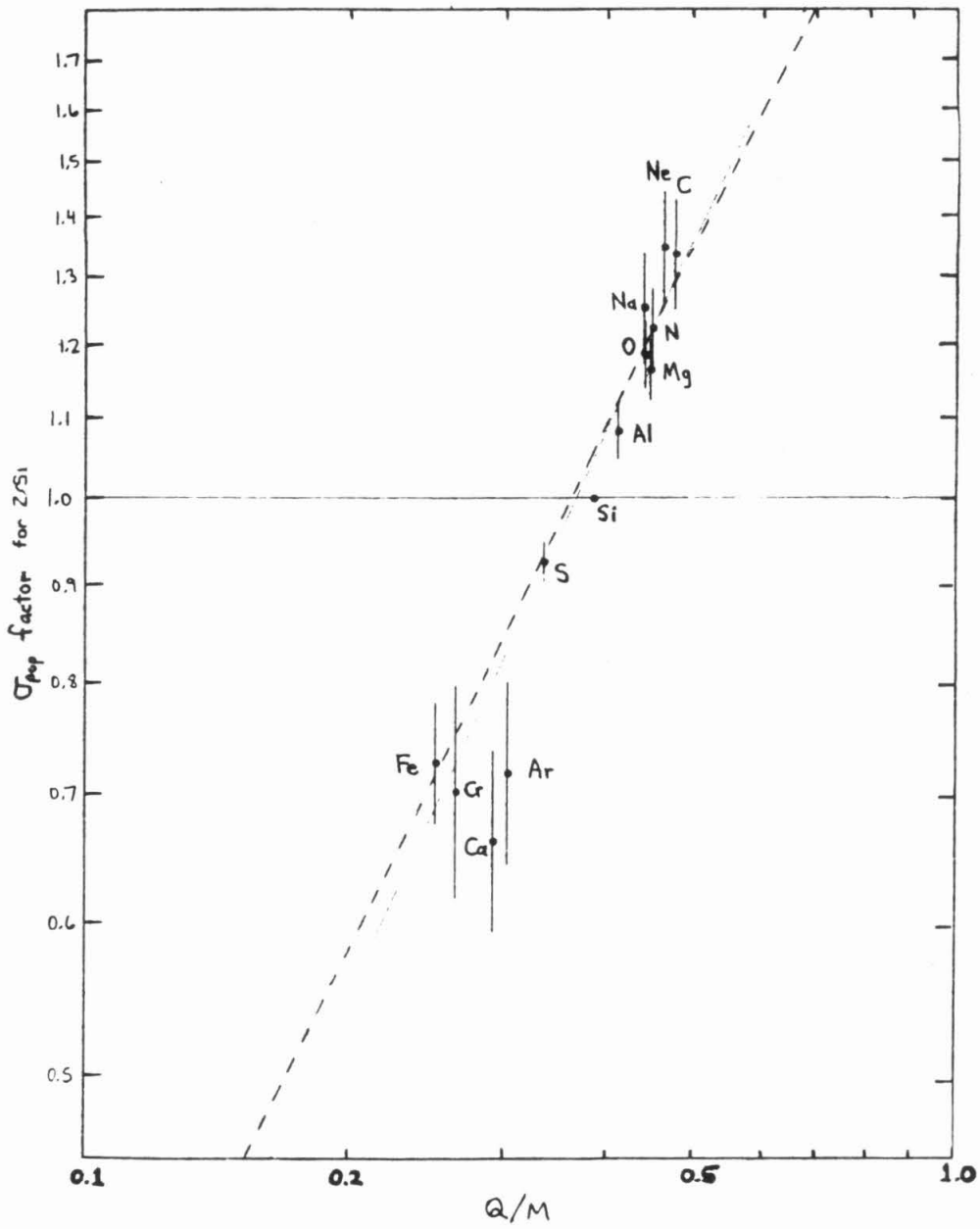

Fig. 4.14. σ_{pop} for the abundance ratio Z/Si vs. Q/M. σ_{pop} is a measure of the width of the flare population distribution for a given elemental ratio; it is obtained through the iterative hybrid weighting procedure described in Section 4.3.1. σ_{pop} is expressed as a factor of dispersion; e.g., the C/Si ratio distribution has a width extending a factor of 1.34 on either side of the mean. The values for elements heavier than Si have been reflected about the horizontal line so that all of the data could be fit to a single power-law function of Q/M. The best fit has a power-law exponent of 0.99 ± 0.08 and a reduced χ^2 of 0.96. The Q values were obtained in the manner described in Section 4.1.1.

abundance are included with the same flare ordering, even though fewer flares are available to study and the effect is somewhat obscured by statistical fluctuations (Fig. 4.7). This behavior had been previously noted (Cook et al. 1979, 1980, 1984; McGuire et al. 1979; Mason et al. 1980; Meyer 1981, 1985) based on other, generally smaller sets of flares, but it is even more apparent in the larger and more varied set of flares considered here. The effect of this degree of variability on the determination of mean SEP composition was discussed in Section 4.3.1; we have already noted (in Section 4.1.1) its possible interpretation in terms of rigidity-dependent propagation and acceleration processes, and thus it must also play a role in deriving true coronal abundances from the measured SEP abundances. Supporting evidence for this model is provided by the abundances in individual flares relative to the average SEP composition, which show a smooth ordering by mean Q/M (Fig. 4.13). The presence of such a relationship is not surprising in view of the behavior described above, since to first order Q/M in SEPs is roughly ordered by Z. The same property is also evident in a plot of the ratio population width σ_{pop} vs. Q/M (Fig. 4.14). Since the variability shown in Figs. 4.13 and 4.14 is well described by a power-law function of Q/M, one anticipates that the *average* SEP composition relative to the true coronal composition should show the same dependence.

4.5 The SEP-Derived Coronal Composition

In order to separate the rigidity-dependent fractionation effect from the FIP effect, we will for now consider only the elements with low FIP (< 10 eV), for which SEP and photospheric abundances are roughly equal. For these elements, our model (Section 4.1.1) assumes that rigidity-dependent effects are the *only* source of fractionation between the photosphere and the SEPs, since these elements are easily ionized and therefore should be equally abundant in the photosphere and the corona. We infer coronal abundances from the photospheric measurements rather than use direct coronal spectroscopic measurements because the photospheric data have much higher precision and are

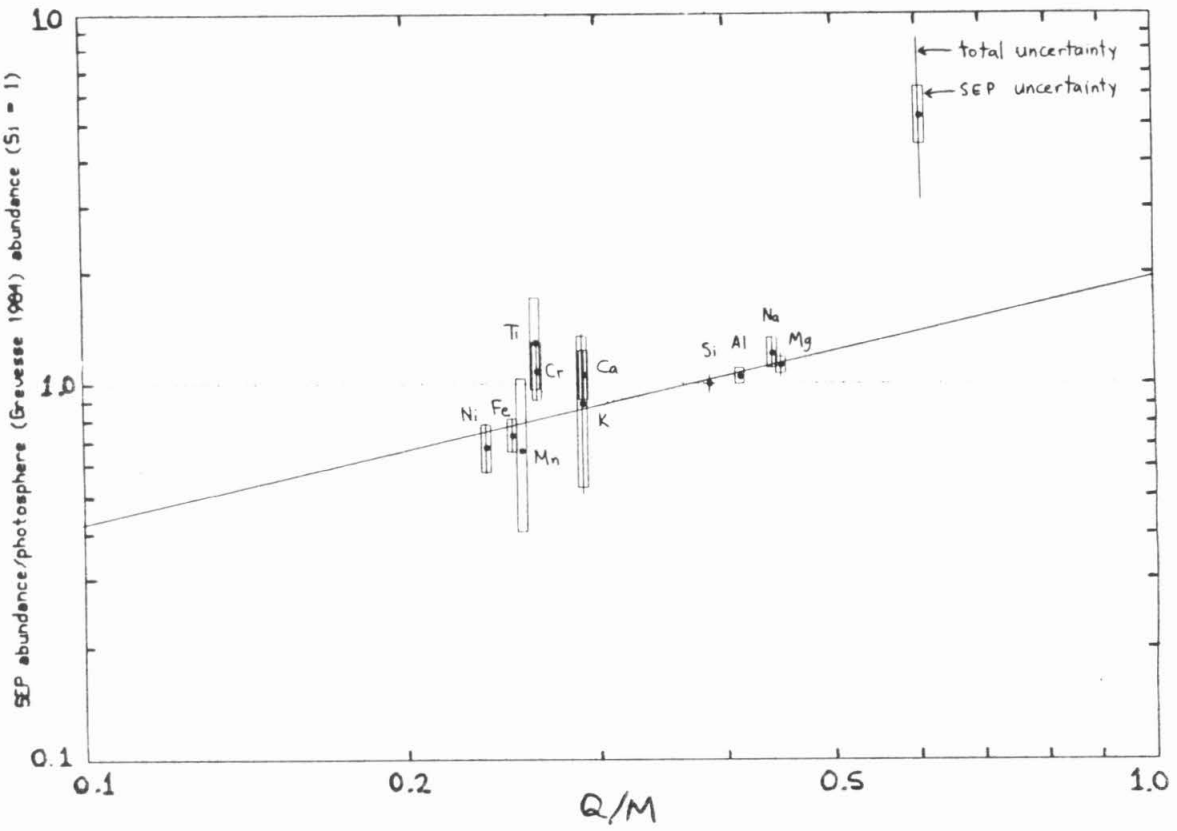

Fig. 4.15. SEP abundance relative to the photospheric abundance (Grevesse 1984) for elements with low first ionization potential (FIP < 9 eV) vs. mean Q/M. The Q values were obtained from recent SEP ionic charge state measurements (Gloeckler et al. 1981, Luhn et al. 1984). "Total uncertainty" is the quadratic sum of the SEP and Grevesse uncertainties. Where no total uncertainty is shown, there is no published uncertainty for the Grevesse abundance. Also shown is the best fit to a power-law function of Q/M, obtained by a weighted least-squares fit of the eight points for which photospheric values are known well (uncertainties quoted). The quoted error bars on the Q measurements range from ~1 to ~6%; these are small compared to the abundance uncertainties and have been neglected in the fitting process.

available for many more elements.

Fig. 4.15 shows the ratio of SEP to photosphere (Grevesse 1984) abundances for the 11 most abundant low-FIP elements (Na, Mg, Al, Si, K, Ca, Ti, Cr, Mn, Fe and Ni) plotted against the mean Q/M. A least-squares fit to a power law

$$\frac{(Z/\,Si)_{SEP}}{(Z/\,Si)_{photosphere}} = K\,(Q/\,M)_z^{\alpha} \qquad (4.12)$$

was done using eight of the points, weighting each point by an uncertainty that combines the quoted photospheric and SEP uncertainties (Al, Ti and Mn were omitted from the fit because no uncertainties were quoted for these elements in the Grevesse (1984) photospheric tabulation). Uncertainties in the measured Q (Luhn et al. 1984) were not included, but they are generally much smaller than the abundance uncertainties (~1 - 6%). The result is a good fit (reduced χ^2 = 1.0) and a best-fit power-law exponent α of 0.66 ± 0.17. This allows one to define an enhancement/depletion factor for SEPs relative to corona for *all* elements, regardless of their FIP.

If the SEP abundances for all elements are divided by the appropriate SEP enhancement/depletion factor, one obtains an estimate of coronal composition by a method completely independent of, and of much higher precision than, spectroscopic methods. The set of abundances resulting from this correction, the "SEP-derived corona," is given in Table 4.9. Included in the quoted uncertainties is a contribution due to the uncertainty in α resulting from the fitting process. In Fig. 4.16, the abundances of the SEP-derived corona relative to photosphere are plotted against FIP. As expected, this results in a better organization of the data by FIP, but this is true for the high-FIP elements that were not part of the fit as well as for the low-FIP elements; all elements with FIP greater than 11 eV, with the exception of C, are uniformly depleted by a factor of 4. Elements with FIP less than 9 eV are equal in the corona and photosphere, again with the exceptions of Ti and Cr (and possibly Ca), although the photospheric uncertainty on Ti may make that deviation insignificant. P and S appear

Table 4.9. Rigidity-dependent fractionation correction factors and SEP-derived coronal abundances. The correction factor is obtained for each element by evaluating the best-fit power law function of Q/M (Fig. 4.15) at the appropriate value of Q/M using the observed SEP ionic charge states (Gloeckler et al. 1981, Luhn et al. 1984), interpolated and extrapolated to elements not measured using the ionization equilibrium calculations of Shull and van Steenberg (1982). The SEP abundance figures in Table 4.8 are divided by this correction value to obtain the derived coronal composition. Numbers in parentheses are factors of uncertainty.

Z	Q/M correction	SEP-derived corona
6	1.156 (1.037)	$2350._{-230.}^{+250.}$
7	1.110 (1.027)	$700._{-49.}^{+52.}$
8	1.096 (1.023)	$5680._{-340.}^{+360.}$
9	1.081 (1.020)	$(0.28^{+0.29}_{-0.28})$*
10	1.133 (1.032)	$783._{-77.}^{+84.}$
11	1.094 (1.023)	$67.0^{+6.8}_{-6.2}$
12	1.107 (1.026)	$1089._{-82.}^{+64.}$
13	1.044 (1.011)	$83.7^{+4.2}_{-4.0}$
14	1.000 (1.000)	1000.
15	0.942 (1.015)	$4.89^{+0.86}_{-0.72}$
16	0.916 (1.022)	$242._{-9.}^{+10.}$
17	0.861 (1.038)	$2.38^{+0.84}_{-0.80}$
18	0.859 (1.039)	$24.1^{+4.2}_{-3.6}$
19	0.834 (1.047)	$3.9^{+2.1}_{-1.6}$
20	0.836 (1.046)	$82._{-12.}^{+14.}$
21	0.792 (1.060)	$(0.31^{+0.55}_{-0.31})$*
22	0.781 (1.064)	$4.9^{+1.6}_{-1.3}$
23	0.771 (1.068)	$(0.48^{+0.69}_{-0.48})$*
24	0.783 (1.064)	$18.3^{+3.9}_{-3.3}$
25	0.765 (1.070)	$6.8^{+3.9}_{-2.7}$
26	0.755 (1.073)	$1270._{-150.}^{+170.}$
27	0.731 (1.082)	< 18.1
28	0.727 (1.084)	$46.5^{+8.1}_{-7.4}$
29	0.682 (1.102)	$(0.57^{+0.87}_{-0.57})$*
30	0.657 (1.112)	$1.61^{+0.87}_{-0.76}$

* Abundances for these elements are based on fewer than 5 particles and are highly uncertain.

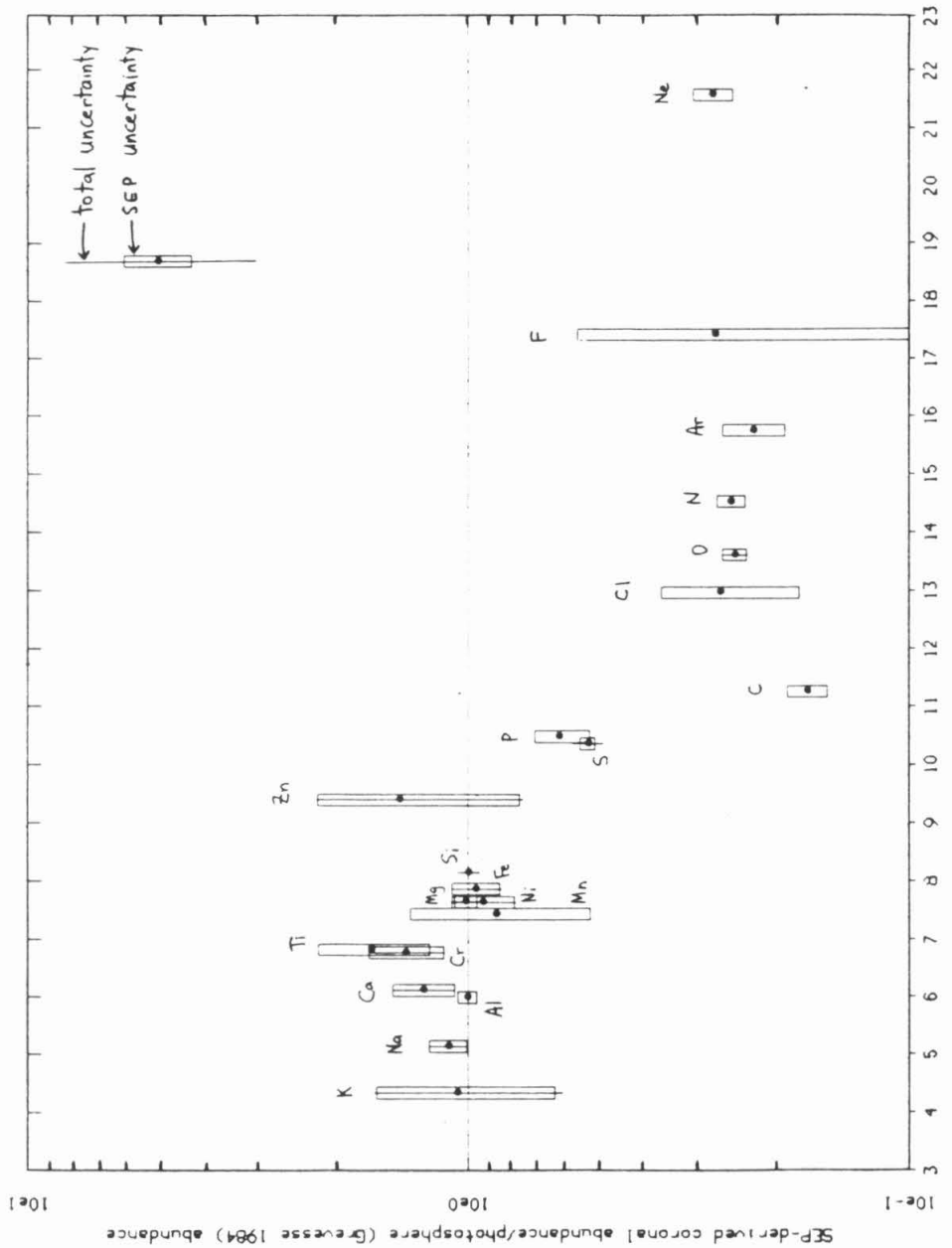

Fig. 4.16. SEP-derived coronal abundance relative to photospheric abundance (Grevesse 1984), plotted vs. first ionization potential. "Total uncertainty" is the quadratic sum of the SEP and Grevesse uncertainties. Uncertainty associated with the fit to the Q/M fractionation is also included. Where no total uncertainty is shown, there is no published uncertainty for the Grevesse abundance.

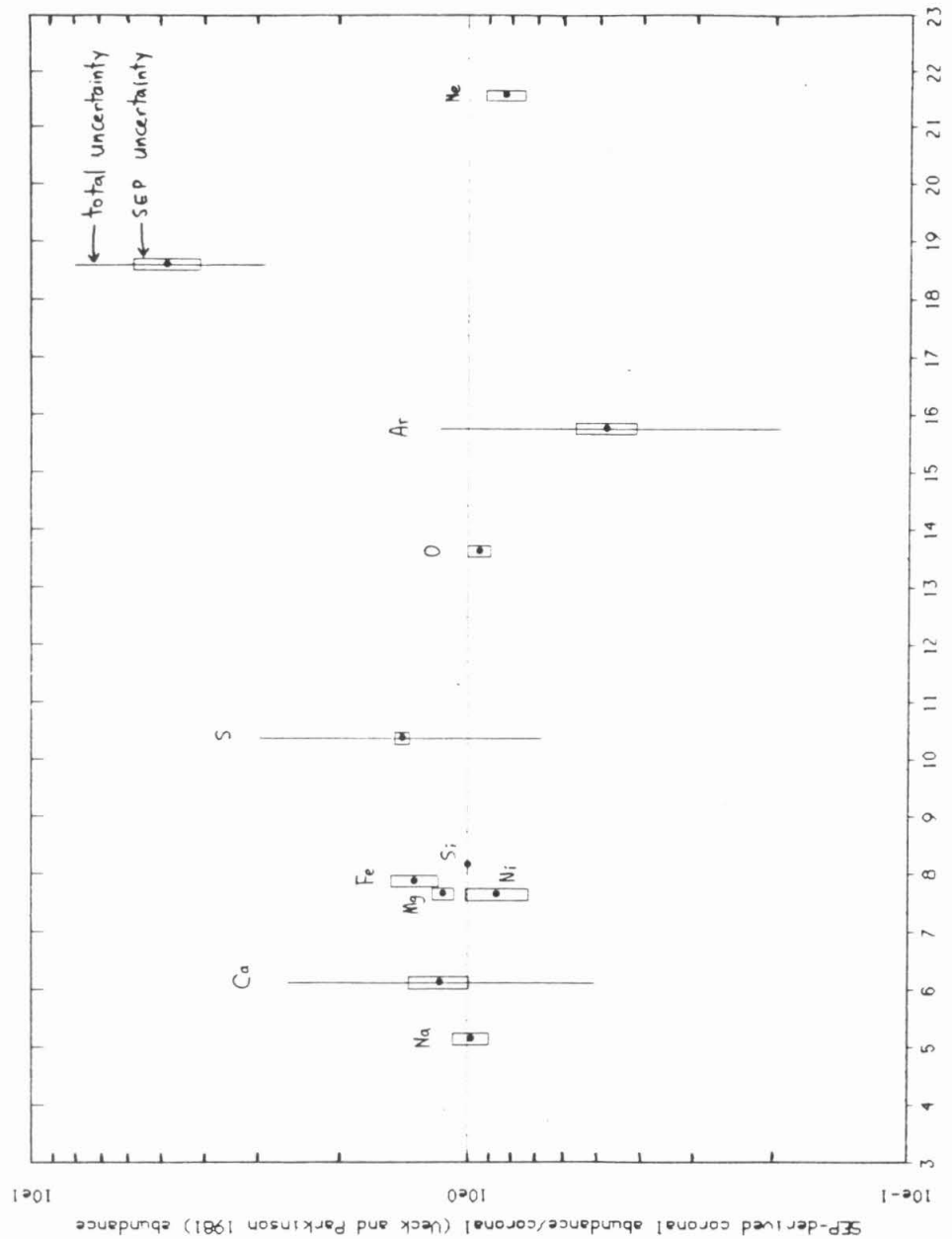

Fig. 4.17. SEP-derived coronal abundance relative to spectroscopic coronal abundance (Veck and Parkinson 1981), plotted vs. first ionization potential. "Total uncertainty" is the quadratic sum of the SEP and spectroscopic uncertainties. Uncertainty associated with the fit to the Q/M fractionation is also included. Where no total uncertainty is shown, there is no published uncertainty for the spectroscopic abundance.

to be in a transitional region. The only real anomalies are Cr and C; there is a suggestion that Cr (and possibly Ca and Ti) may be somewhat overabundant, and C somewhat overly depleted in the corona based on this model. The underabundance of C is particularly significant since the Geiss and Bochsler (1984) model predicts that C should if anything be *less* depleted than N, O, Ne and Ar.

It is clearly of interest to compare the SEP-derived coronal composition with available coronal measurements obtained by spectroscopic techniques. This is done in Fig. 4.17, in which the ratio of SEP-derived corona to coronal abundances from Veck and Parkinson (1981) is plotted versus FIP. The two coronal measurements agree to within a factor of ~2 and show no apparent trend with FIP. The differences of up to a factor of 2 are large compared to the SEP uncertainty, even when the uncertainty in the rigidity-dependent fractionation correction is included, but are comparable to the quoted uncertainties in the spectroscopic coronal measurements. Thus the two coronal measurements are not inconsistent, and the SEP-derived measurement is of much higher precision and is available for a larger set of elements. Similar statements may be made concerning the SEP-derived coronal composition relative to the solar wind (Fig. 4.18).

From Table 4.8 it can be seen that among the more abundant elements, the principal difference between the photospheric tabulation of Grevesse (1984) and the other abundance standards is the high abundance of Fe in Grevesse. There is in fact some uncertainty concerning the true photospheric abundance of Fe (Blackwell et al. 1984) due to poorly known atomic oscillator strengths and uncertainties in the solar atmospheric model. Since the Grevesse tabulation was used as the photospheric standard in generating the SEP-derived coronal composition and since the Fe point is an important contributor to the fit, it is necessary to address the likelihood that the photospheric Fe abundance actually is higher than in meteoritic material. The present results support this possibility for the following reasons:

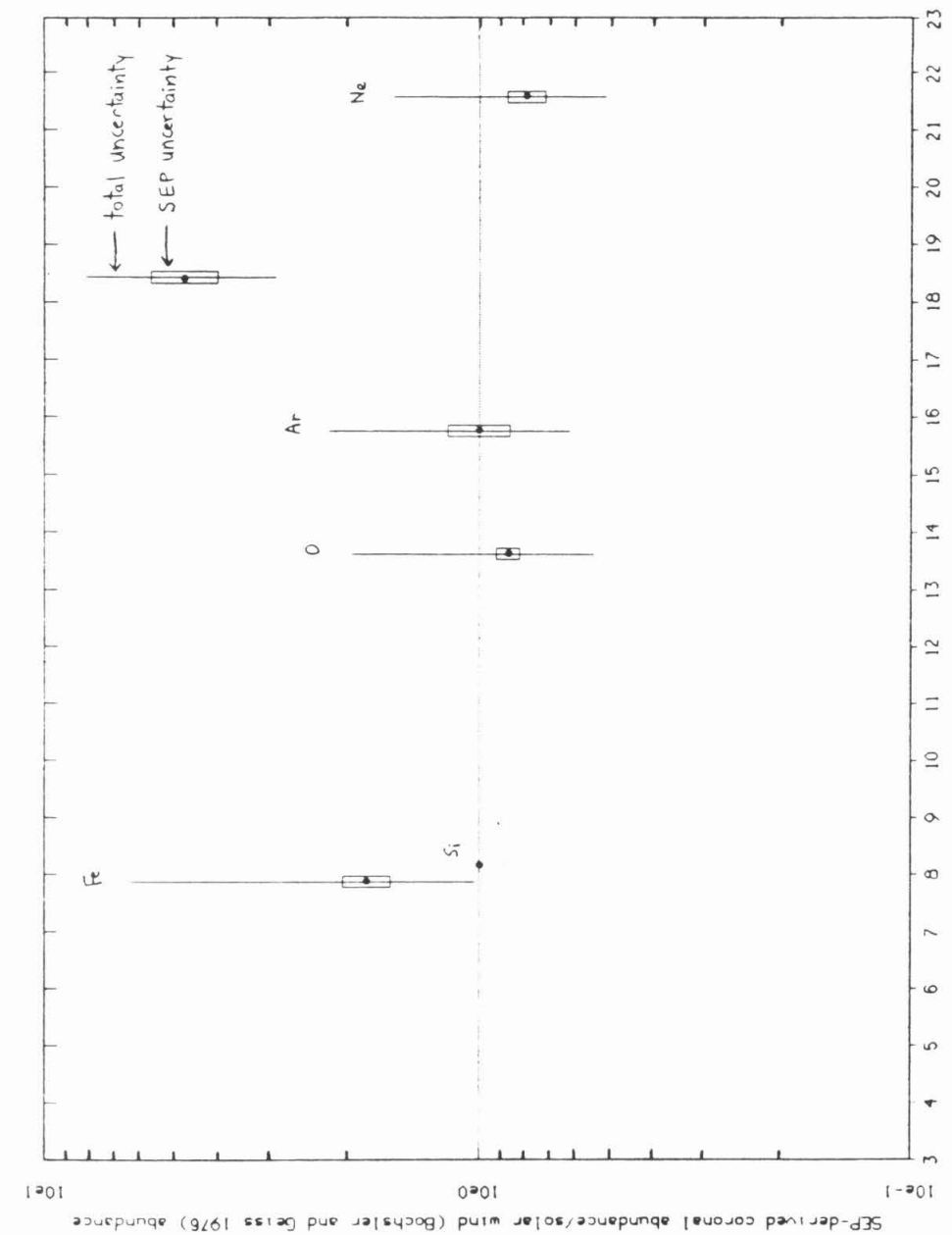

Fig. 4.18. SEP-derived coronal abundance relative to solar wind abundance (Bochsler and Geiss 1976), plotted vs. first ionization potential. "Total uncertainty" is the quadratic sum of the SEP and spectroscopic uncertainties. Uncertainty associated with the fit to the Q/M fractionation is also included.

(1) The raw SEP composition (Table 4.8) is already as rich in Fe as meteorites or the earlier photospheric data of Ross and Aller (1976), even without any Q/M fractionation correction.

(2) If one derives a correction factor in the manner described above to correct for rigidity-dependent acceleration fractionation of SEPs, one obtains a positive slope α, and hence a coronal composition richer in Fe, even if the Anders and Ebihara (1982) abundance standard is used instead of Grevesse.

(3) If the Grevesse composition is used as the standard, a better fit is obtained than by using C1 composition (reduced χ^2 = 1.2), C2 composition (reduced χ^2 = 2.3) or the Anders and Ebihara (1982) "solar system" composition (reduced χ^2 = 1.6). Ross and Aller (1976) gives a fit of comparable quality to the Grevesse fit (reduced χ^2 = 0.9), but only because the uncertainties in the Ross and Aller data are much larger than those of Grevesse. The Grevesse standard also yields a smaller percentage uncertainty (~25%) on the fitted value α than do the other abundance standards (typically ~60%).

(4) The quality of the fit using the Grevesse standard is of course heavily affected by the use of the Fe data point in question. However, if that point is omitted from the fitting process, the fit still yields a positive slope (α = 0.55 ± 0.21) and hence a significant upward correction to Fe.

An independent test of the reasonableness of a correction of this magnitude can be made by recalling that there is evidence to suggest that higher-rigidity species are less efficiently accelerated, and therefore the SEP-derived coronal composition should be richer in Fe than SEPs from most individual flares. If one fits to a power-law in Q/M the SEP abundances of individual flares relative to their average (e.g., Fig. 4.12) one finds that for only two of the 22 flares is the best-fit slope significantly less than $-\alpha$ = -0.66, i.e., only two flares (1c and 1e) are richer in Fe than the SEP-derived coronal composition, apparently corresponding to the infrequent case of the higher-rigidity species

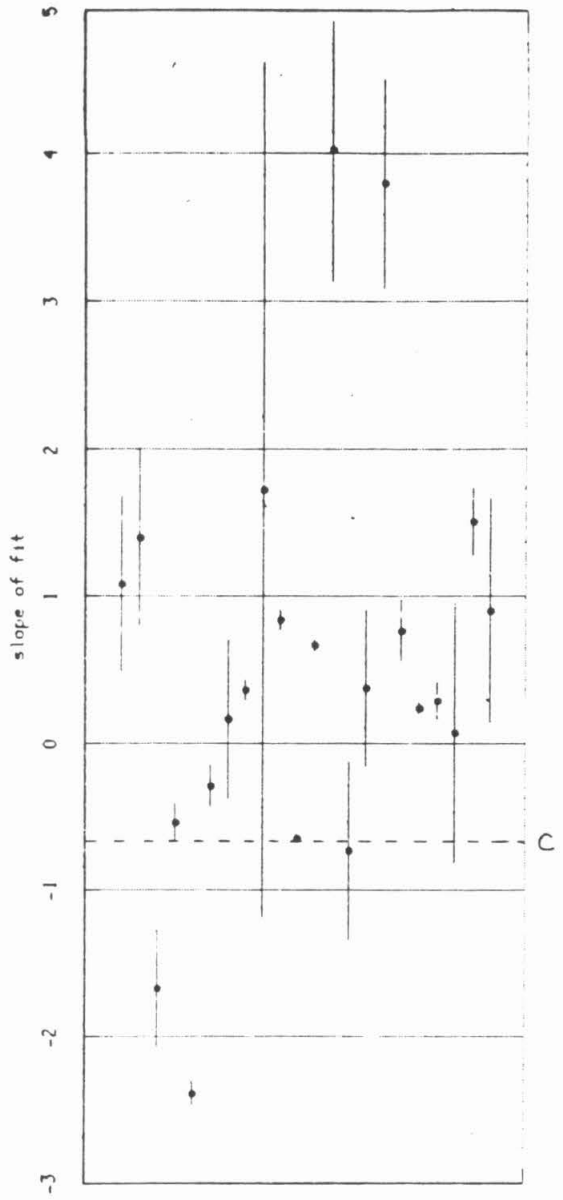

Fig. 4.19. Best-fit slopes of fit of SEP abundances in individual flares relative to the average SEP abundance vs. Q/M to a power-law function of Q/M (e.g., Fig. 4.13). The dotted line marked C represents the slope corresponding to the SEP-derived coronal composition.

being *more* efficiently accelerated (Fig. 4.19). These two exceptions may be accounted for by propagation effects; although acceleration fractionation in our model would tend to always deplete Fe to some degree, propagation fractionation can have an enhancing effect at the onset of the flare, as noted in Section 4.1.2. Both flares 1c and 1e do show higher Fe abundance at the onset compared with the decay phase. A plot of heavy ion counting rate as a function of time shows that flare 1c had a sharp rise and a relatively steep falloff in intensity with time, indicating that the onset period made a relatively large contribution to the average composition for this flare. This was not the case for flare 1e, but the decay phase abundance of Fe indicates a composition nearly unfractionated by acceleration. In this case even a modest degree of propagation fractionation dominates and yields an average SEP composition for the flare which is richer in Fe than coronal. Other flares more heavily fractionated by acceleration are still deficient in Fe after propagation.

We conclude that the data support a model in which the acceleration process acts only to deplete high-rigidity species relative to low-rigidity species, and that the occasional overabundances, relative to the unfractionated coronal composition, of high-rigidity species in individual flares may be accounted for by the relative importance for these flares of propagation effects which enhance the high-rigidity species.

Finally, we note that the Q/M-dependence of the average fractionation (Fig. 4.15) is a relatively weak dependence, i.e., the fractionation of a given element changes little, compared to its range of variability from flare to flare, when the Q/M values are changed by amounts that are reasonable based on the expected degree of coronal temperature variability. This implies that the bulk of the fractionation due to the acceleration process is caused by changes in the rigidity-dependence of this process rather than by changes in the rigidities themselves.

4.6 The SEP-Derived Photospheric Composition

Having obtained a coronal composition from the SEP measurements by correcting for a rigidity-dependent acceleration fractionation of SEPs, one may further correct for the FIP-dependent process of coronal formation to obtain a derived photospheric composition. As noted in Section 4.3.3, the dynamical model of Geiss and Bochsler (1984) predicts a FIP-dependent fractionation of the corona relative to the photosphere resulting from differing degrees of ionization of neutral atoms moving upward from the photosphere (for example in spicules) on a time scale of ~10 sec, and separation of charged and neutral species in the chromosphere or lower transition region. This model predicts a general ordering by FIP but is affected somewhat by other atomic parameters. We shall assume that elements with FIP < 10 eV are uniformly unfractionated, since they are either already ionized in the photosphere or else ionize rapidly relative to the time scale of the coronal formation process. Elements with FIP > 11 eV are taken to be uniformly depleted by a factor of ~4 in the corona. This is harder to justify based on FIP alone, but it agrees with the present data (Fig. 4.16), and also (except for C) with the Geiss and Bochsler (1984) calculation. The elements between 10 and 11 eV (P and S) are apparently in a transitional region, with intermediate degree of fractionation.

To derive a "SEP-derived photospheric abundance" by correcting the SEP-derived coronal abundances for the FIP fractionation, the high-FIP elements N, O, F, Ne, Cl, and Ar are multiplied by $4.03^{+0.27}_{-0.25}$, the ratio of O/Si in the photosphere (Grevesse) to O/Si in the SEP-derived corona. Only oxygen is used for this because it is the only high-FIP element with a well-determined photospheric abundance, but a weighted average of these high-FIP elements (using SEP uncertainties) does not differ significantly ($3.95^{+0.17}_{-0.16}$). Thus the SEP-derived photospheric oxygen abundance is derived circularly and is identically equal to the Grevesse abundance, but the remaining high-FIP elements are derived with the assumption that elements with FIP > 11 eV are uniformly depleted by a factor best estimated by using the oxygen abundances. Since

Table 4.10. Abundances of the high-FIP (> 11 eV) elements relative to oxygen for the SEP-derived corona. Except for carbon, the same abundances hold for the SEP-derived photosphere, since these elements are corrected by the same factor relative to the low-FIP (< 10 eV) elements. The relative uncertainties are changed by the oxygen normalization because the ratio population variances are different (lower for C and N, higher for Ar).

Z	SEP-derived corona
6	$411._{-17.}^{+18.}$
7	$121.2_{-2.2}^{+2.3}$
8	1000.
10	$137.3_{-8.5}^{+9.0}$
18	$4.46_{-0.76}^{+0.89}$

Table 4.11. SEP-derived photospheric abundances, obtained by multiplying the SEP-derived coronal abundance figures in Table 4.9 by FIP-dependent fractionation correction factors. The correction factor for elements with FIP > 11 eV is $4.03^{+0.27}_{-0.25}$, the ratio of oxygen abundances in the photosphere (Grevesse 1984) and the SEP-derived corona (Table 4.9). For P and S, the correction factor is 1.89 ± 0.14, the photosphere/SEP-derived corona ratio of sulfur abundances. For C, the correction factor is the geometric mean of the O and S correction factors. For the remaining elements (FIP < 10 eV) there is no correction. The uncertainty in the correction factor is not incorporated into the quoted uncertainties for the high-FIP elements, since it affects each of these elements in the same way.

Z	SEP-derived photosphere
6	$6490.^{+280.}_{-270.}$
7	$2775.^{+53.}_{-50.}$
8	22900.
9	$(1.1^{+1.2}_{-1.1})$*
10	$3140.^{+205.}_{-195.}$
11	$67.0^{+6.8}_{-6.2}$
12	$1089.^{+64.}_{-62.}$
13	$83.7^{+4.2}_{-4.0}$
14	1000.
15	$9.24^{+1.46}_{-1.54}$
16	$460.^{+42.}_{-39.}$
17	$9.6^{+3.5}_{-3.3}$
18	$102.^{+20.}_{-17.}$
19	$3.9^{+2.1}_{-1.6}$
20	$82.^{+14.}_{-12.}$
21	$(0.31^{+0.55}_{-0.31})$*
22	$4.9^{+1.8}_{-1.3}$
23	$(0.48^{+0.69}_{-0.48})$*
24	$18.3^{+3.9}_{-3.3}$
25	$6.8^{+3.9}_{-2.7}$
26	$1270.^{+170.}_{-150.}$
27	< 18.1
28	$46.5^{+8.1}_{-7.4}$
29	$(0.57^{+0.87}_{-0.57})$*
30	$1.61^{+0.87}_{-0.76}$

* Abundances for these elements are based on fewer than 5 particles and are highly uncertain.

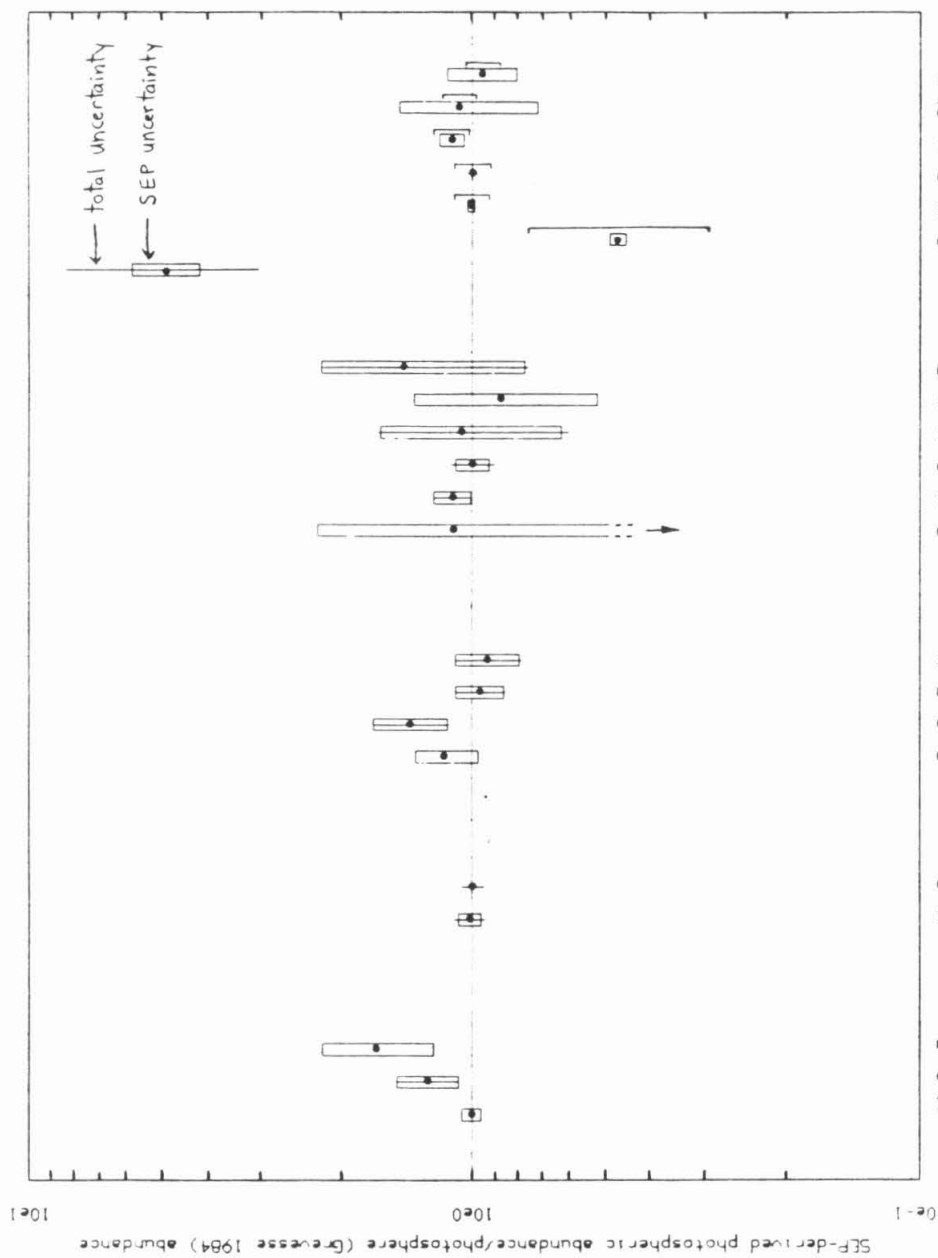

Fig. 4.20. SEP-derived photospheric abundance relative to photospheric abundance (Grevesse 1984). The elements are grouped into the five cosmochemical classes (based on condensation temperature) used in meteoritic studies: refractories, silicate, siderophiles, volatiles and highly volatiles. "Total uncertainty" is the quadratic sum of the SEP and Grevesse uncertainties. Where no total uncertainty is shown, there is no published uncertainty for the Grevesse abundance. The values for the high-FIP elements have been determined relative to oxygen; for these elements, the uncertainty plotted does not include the uncertainty in the FIP fractionation correction factor (due mainly to SEP population variance of the O/Si ratio). This uncertainty, which affects the high-FIP elements as a group, is indicated by the brackets next to the points. The adopted value for C results from applying the average of the O and S corrections; although the proper FIP correction for C is unknown, the calculation of Geiss and Bochsler (1984) suggests that it should be intermediate between those for O and S. The bracket for C reflects this large uncertainty in the correction factor.

most of the uncertainty in the value of this correction is due to the population variance of the O/Si ratio, and since it affects all of the high-FIP elements in the same way, this uncertainty was not incorporated into the total uncertainty in the derived photospheric abundances for each of these elements; only the uncertainty in their ratio to oxygen was included, although the O/Si population variance introduces another factor of uncertainty to the abundances relative to Si of the high-FIP group as a whole. The abundances of these elements relative to oxygen in the SEP-derived photosphere are given in Table 4.10.

Similarly, P and S are multiplied by the ratio of S/Si in Grevesse to S/Si in the SEP-derived corona (1.89 ± 0.14), again because P is not as well known in the photosphere as S. (Although the degree of fractionation varies significantly within this range of FIP, this procedure is valid since P and S have nearly identical FIP). For carbon, the adopted value is taken to be that derived by applying a correction which is the geometric mean of the oxygen and sulfur corrections. Although the proper FIP correction for C is not known, it should be intermediate between the O and S corrections, based on the Geiss and Bochsler (1984) model. The low-FIP elements are of course unchanged. The resulting SEP-derived photospheric abundances relative to Si are given in Table 4.11.

In Fig. 4.20 is plotted the ratio of the SEP-derived photospheric abundance to the Grevesse (1984) photospheric abundance. The elements are grouped into the five cosmochemical groups (based on condensation temperature) used in meteoritic studies. Apparent are the anomalies noted earlier in connection with the SEP-derived coronal abundances: the lower abundance of C (by at least 50% and possibly much more), and the significant excess of Cr (and possibly Ti). All other elements agree within about one standard deviation or less. When the SEP-derived photospheric abundances are compared to the "solar system" abundances of Anders and Ebihara (1982) (Fig. 4.21), one sees, in addition to significant excesses of Ca, Cr and Ti, a 40% excess of Fe. The uniformly higher abundance of this group of heavy elements is also displayed in Table 4.12, in which the abundances of Ca, Ti and Cr relative to Fe are shown for the SEP-

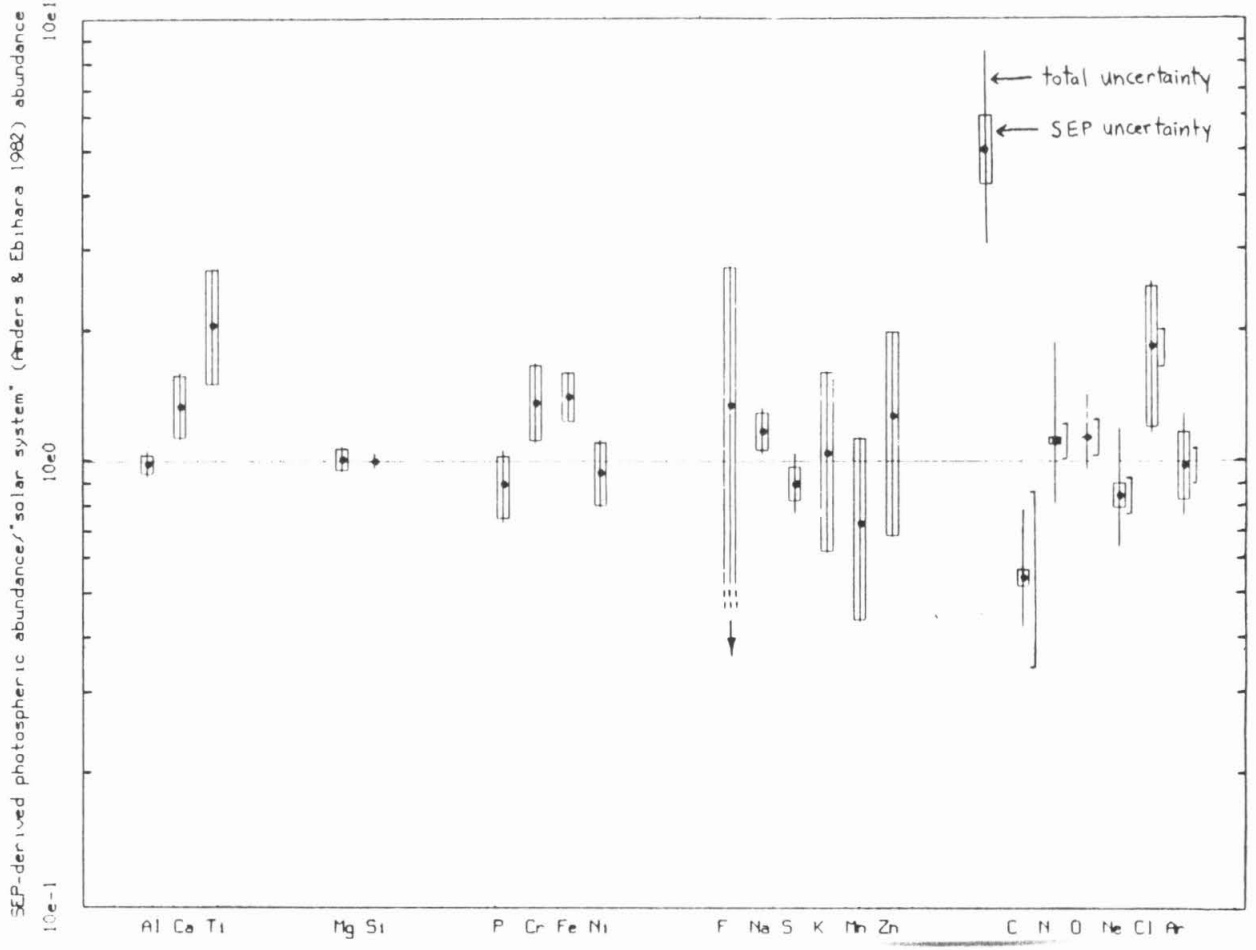

Fig. 4.21. SEP-derived photospheric abundance relative to "solar system" abundance (Anders & Ebihara 1982). The elements are grouped into the five cosmochemical classes (based on condensation temperature) used in meteoritic studies. "Total uncertainty" is the quadratic sum of the SEP and "solar system" uncertainties. The values for the high-FIP elements have been determined relative to oxygen; for these elements, the uncertainty plotted does not include the uncertainty in the FIP fractionation correction factor (due mainly to SEP population variance of the O/Si ratio). This uncertainty, which affects the high-FIP elements as a group, is indicated by the brackets next to the points. The adopted value for C results from applying the average of the O and S corrections; although the proper FIP correction for C is unknown, the calculation of Geiss and Bochsler (1984) suggests that it should be intermediate between those for O and S. The bracket for C reflects this large uncertainty in the correction factor.

Table 4.12. Abundances of Ca, Ti and Cr relative to Fe in the SEP-derived corona (same as SEP-derived photosphere for these elements), compared to "solar system" abundances from Anders and Ebihara (1982) and spectroscopic photospheric abundances from Grevesse (1984). No uncertainty is quoted for the Grevesse abundance of Ti.

Z	SEP-derived corona	Anders and Ebihara (1982)	Grevesse (1984)
20	$60.7^{+5.7}_{-5.3}$	67.9 ± 1.3	$48.9^{+2.1}_{-2.0}$
22	$3.9^{+1.0}_{-0.8}$	2.66 ± 0.06	2.2
24	$14.3^{+2.4}_{-2.0}$	14.9 ± 0.4	10.0 ± 0.5
26	1000.	1000.	1000.

derived corona (equal to the SEP-derived photosphere for these elements), Anders and Ebihara (1982) and Grevesse (1984). The uncertainties in the SEP values are reduced by normalizing to Fe, since the difference in Q/M for these elements is less than when normalizing to Si. It can be seen that the SEP-derived ratios of Ca, Ti and Cr to Fe agree well with Anders and Ebihara even though Fe itself is low relative to Si in Anders and Ebihara. On the other hand, the Grevesse Fe abundance agrees with the SEP-derived figure but the abundances of Ca, Ti and Cr are systematically lower in Grevesse.

Although the SEP-derived photospheric abundances are not always of higher precision than spectroscopic photospheric measurements, they are determined for many elements for which accurate spectroscopic data is lacking on account of the scarcity or absence of strong, unblended lines in the photospheric spectrum. This is particularly true of elements in the high-FIP group (C, N, O, Ne, Cl and Ar). In addition, the derivation of solar abundances from SEPs involves the use of fewer parameters that may contribute to systematic errors. In the case of the spectroscopic measurements, such parameters include both atomic physics parameters and parameters of the solar atmospheric model: temperature structure, microturbulence velocity, damping constants, oscillator strengths, line equivalent widths, as well as theoretical assumptions in the model itself. Errors in these parameters are often difficult to quantify but may be significant. Similar statements about possible systematic errors may be made concerning meteoritic abundances, despite the high *precision* of the basic composition measurements. On the other hand, using only two simple models (with three free parameters) for photospheric/coronal fractionation and rigidity-dependent acceleration/propagation fractionation of SEPs, both of which are supported by observational and theoretical arguments, the coronal and photospheric composition may be determined from SEPs to an accuracy limited primarily by particle and flare counting statistics.

Chapter 5

Summary and Conclusions

The elemental composition of solar energetic particles (SEPs) from 22 solar flare events has been determined using data collected by the Low-Energy and High-Energy Telescopes aboard the Voyager 1 and 2 spacecraft during the 1977-1982 time period. Finite abundances were obtained for all elements with $3 \leq Z \leq 30$ except for Li, Be, B, F, Sc, V, Co and Cu, for which upper limits were obtained. The large number of analyzed particles available in the Voyager data set permitted the average abundances of several rare elements (e.g., P, Cl, K, Ti) to be measured for the first time, and the abundances of others (e.g., Na, Al, Ar, Cr) to be determined with significantly improved accuracy. For the most abundant elements (C, N, O, Ne, Mg, Si, S and Fe), SEP abundances were determined in each of the individual flares; the large number of distinct flare events in the data set made possible a more accurate characterization of the flare-to-flare variability and its influence on the determination of the average SEP abundance. The result was an improvement of a factor of ~3 in the precision of the average SEP abundances compared to earlier studies. The new abundances themselves generally agreed well with previously published values.

The importance of interplanetary propagation effects was assessed by investigating the time- and energy-dependence of abundance ratios, comparing Voyager 1 with Voyager 2 measurements, and comparing flares observed at differing radial distances from the sun. It was found that propagation effects, while present, were generally small compared to the range of variability in abundance ratios between different flares, when averaged over a suitably long time period. In addition, it was found that even these small propagation effects typically exhibited a simple power-law dependence on the ionic charge-to-mass (Q/M) ratio of the ionic species making up the SEPs. Thus it was concluded that most of the flare-to-flare variability was an inherent property of the SEP source region and was most likely a variable acceleration-induced fractionation caused

by variation from flare to flare in the rigidity-dependence of the shock acceleration process.

The average SEP composition was compared to other elemental abundance standards, including those derived from spectroscopic studies of the photosphere and the corona, analysis of carbonaceous chondrite meteorites, and the solar wind. The fractionation of SEP abundance relative to photosphere based on first ionization potential (FIP) reported in the past was seen, and the pattern continued to hold for the newly-measured rarer elements. The SEP abundances agreed with solar wind and spectroscopic coronal data within the relatively large uncertainties of the latter measurements.

The systematic properties of the flare-to-flare variability were surveyed with the sample of 22 flare events. It was found, in agreement with previous research, that in individual flares there is a high degree of correlation between elements in their enhancement or depletion relative to the flare average, and that this flare-to-flare variability, which had previously been described as a roughly monotonic function of Z, could be better described as a monotonic dependence on Q/M. Ratios of elements that are near neighbors on the charge scale (and therefore with similar Q/M) show much less variability than ratios of widely-separated elements. The Q/M-dependence suggested that the flare-to-flare variability is most likely a product of rigidity-dependent fractionation during acceleration and, to a lesser degree, interplanetary propagation. Thus one expected that the average SEP composition should show a similar type of fractionation relative to the true coronal composition.

Motivated by these observations, it was found that the small differences between SEP average and photospheric abundances for the low-FIP elements (those equally abundant in the corona and the photosphere) could be ordered by Q/M; specifically, elements with higher rigidity (lower Q/M) are less efficiently accelerated and thus are depleted in SEPs. By fitting the data to a power-law dependence on Q/M, a single-parameter correction function was

obtained that allowed the derivation of true coronal abundances of *all* elements from the SEP measurements. The resulting SEP-derived coronal abundances were consistent with the available spectroscopic coronal data but had much higher precision and were available for a much larger set of elements. All but two of the 22 flares are consistent with being depleted in high-rigidity species relative to the SEP-derived corona; propagation effects may account for these exceptions. The average fractionation of SEPs was found to be relatively insensitive to systematic shifts in Q/M values associated with different coronal temperatures, making it likely that variability in the rigidity-dependence of the shock acceleration process rather than in coronal temperature is the primary source of the flare-to-flare composition variability of SEPs.

The SEP-derived coronal abundances relative to the spectroscopic photospheric abundances were found to be well-organized by FIP, the major anomalies being an excess of Cr (and possibly Ti) and deficiency in C of at least 50%. Even though the abundances of the high-FIP elements (N, O, F, Ne, Cl, Ar) are poorly known in the photosphere, the coronal abundances of these elements appear to be uniformly depleted by a factor of 4. A SEP-derived photospheric composition was obtained by correcting the coronal abundances by this factor, a procedure supported by both observational and theoretical considerations. An additional factor was used to correct the two elements of intermediate FIP fractionation, P and S, and C was corrected using the mean of the oxygen and sulfur factors. The major difference between the SEP-derived photospheric abundances and meteoritic abundances, besides those mentioned above for the corona, is a 40% higher abundance of Fe, in agreement with the most recent spectroscopic data on the photosphere. The uncertainties in the SEP-derived photospheric abundances are not generally smaller than those quoted for the spectroscopic photospheric tabulation. However, abundance determinations from spectroscopy rely on many more physical parameters that must be measured, calculated or estimated. Furthermore, the use of SEP measurements, permits the determination of photospheric abundances for several elements (C, N, Ne, Ar) which

cannot be directly measured spectroscopically. We conclude that solar energetic particles represent an important new source of information on solar coronal and photospheric composition.

Appendix A

Final Energy Calibration from In-Flight Data

The energy calibrations obtained in the laboratory were modified slightly by the use of in-flight data. The procedure used was analogous to that described by Cook (1981); the basic concept was to utilize the flight data for oxygen to derive scale factors to the energies measured from each detector, so that these energies agreed with those expected based on the oxygen range-energy relation of Vidor (1975) with the detector mean pathlength values determined in Section 2.7.1. Oxygen was the element chosen for this purpose because it has the highest abundance, and therefore best statistical accuracy, of any heavy element; is one of the best-resolved elements in the CRS instruments; and is virtually mono-isotopic and thus lacks the complications introduced by the presence of multiple isotopes.

The first step of this procedure was to define the set of oxygen events to be used in the calibration. The time period chosen was flare period 7 (see Table 3.7), which comprises three large solar flares and represents a major fraction of the SEP data collected by Voyager. (For LET C on Voyager 1, the procedure also had to be carried out using data from another time period, flare period 17, on account of an anomalous gain-shift problem occurring during period 7; this will be discussed in more detail in Section 3.8.) For each LET or HET telescope, all three-parameter data collected during the indicated time period were displayed on a ΔE vs. E' plot like Fig. 2.3, only using raw pulse heights instead of calculated energies; on such a plot the oxygen "track" is clearly evident and it is straightforward to draw a "box" around the track to define the set of events to be considered oxygen. These events were then ordered by E' (L3 or C1) pulse height and binned in groups of ~20 - 30 events. The mean and standard deviation of the ΔE pulse heights (L1 and L2 in LET, A1 and A2 in HET) were calculated for the events in each E' bin; to suppress statistical fluctuations, the standard deviations for each bin were replaced by the average of the standard

deviations of the nine bins centered on the bin in question (fewer values were used in the averaging for bins near the ends of the track). The revised oxygen track definition was a band extending 2.5σ on either side of the mean ΔE pulse height. This had the effect of discarding some of the "outliers" present in the initial "box" estimate of the oxygen track.

Once the set of oxygen events had been defined, the laboratory energy calibration was applied to the mean pulse heights and sigmas to produce energy loss means and sigmas. The expected true energy loss in the ΔE-detector (L1, L2, A1 or A2) can be found from the range-energy relation R(E) for oxygen (in this case that of Vidor (1975)), the mean pathlength T in the ΔE-detector, and the true energy loss in the E'-detector (L3 or C1) by solving for ΔE in the equation

$$R(E'+\Delta E) = R(E') + T \tag{A.1}$$

to obtain ΔE as a function of E'.

$$\Delta E = f(E') \tag{A.2}$$

If it is assumed that an energy loss E_{cal} based on the laboratory calibration and the true energy E differ by a constant scale factor F_E for any given detector,

$$E = F_E E_{cal} \tag{A.3}$$

then this factor may be estimated by doing a least squares fit of the oxygen data points with the scale factors as the free parameters, that is by minimizing

$$\chi^2(F_{\Delta E}, F_{E'}) = \sum_i \frac{1}{\sigma_i^2}\left[\frac{f(F_{E'}E'_{cal,i})}{F_{\Delta E}} - \Delta E_{cal,i}\right] \tag{A.4}$$

where the sum is over the E' bins.

The gain correction factors obtained by this process are listed in Table A.1. For LET, the values obtained here differ by 1% or less from those obtained

previously by Cook (1981) using a similar procedure. This difference primarily represents differences in the selection of the data to be fit; the statistical uncertainty of the fit is about an order of magnitude smaller than this.

For the HETs, an attempt was made to improve on the manufacturer-supplied detector thicknesses by considering the quality of these fits to the oxygen flight data, i.e., by making T in Eq. (A.4) another free parameter. It was found that when the ΔE-detector thickness was changed in Eq. (A.4), the best-fit gain factor would almost perfectly compensate for it, resulting in a comparably good fit. To achieve an actual minimum in χ^2 as a function of both the F_E and T required both the thickness and gain factors to change by amounts far greater than the realistic uncertainties in these quantities. It was concluded that the procedure was not sensitive enough to physically reasonable variations in the thickness parameter. Therefore the adopted values of the detector thicknesses were taken to be the manufacturer's values, and the adopted gain correction factors were taken to be those that gave the best fit to the oxygen data when the manufacturer's thicknesses were used.

Table A.1. Gain correction factors for LET and HET detectors obtained from final energy calibration using oxygen flight data. Uncertainties on these values are ~0.0005 for F_{L1} and F_{L2}, and ~0.001 for F_{L3}.

VGR	LET	F_{L1}	F_{L2}	F_{L3}
1	A	0.9775	0.9911	0.9341
1	B	0.9971	0.9971	0.8954
1	C	1.0444	1.0220	0.9096
1	D	1.0100	0.9785	0.9734
2	A	0.9511	0.9784	0.9322
2	B	0.9880	0.9594	0.9090
2	C[1]	0.9546	1.0149	0.9334
2	C[1]	0.9419	1.0124	1.3758
2	D	1.0122	1.0428	0.9474

VGR	HET	F_{A1}	F_{A2}	F_{C1}
1	1	0.9730	0.9970	0.9141
1	2	0.9720	1.0007	0.8928
2	1	0.9566	0.9982	0.8876
2	2	0.9698	0.9925	0.9151

[1] The second set of figures for Voyager 2 LET C applies to flare period 7 only. The first set of figures applies to all other flare periods.

Appendix B

Range Correction Parameters for Charge Calibration

Table B.1. Range correction parameters used in HET charge calibration. A set of parameters was obtained for each HET and separately for 2- and 3-parameter data, for the elements oxygen, neon, magnesium, silicon and iron. The typical uncertainties of these values range from ~2% for A_4 to ~20% for A_8, although the uncertainties for individual cases range about a factor of 4 on either side of these average values. In most cases these uncertainties for a given parameter A_i are small compared to the differences between values of the parameter obtained for different elements, indicating that a large part of this variation is due to correlations between the parameters in the behavior of the function $C(x)$ (Eq. 3.2) and not due to statistics. This also accounts for the apparently random variation of individual parameters with Z; individual parameters cannot be considered in isolation, so the interpolation to other values of Z must be carried out on the function values themselves, not on each of the parameters.

VGR	HET	2/3 pars.	Z	A_1	A_2	A_3	A_4	A_5	A_6
1	1	3	8	1.45082	0.74925	9.54661	2.38147	0.00002	24.1309
1	1	3	10	1.12060	0.11728	173.459	2.08849	0.06168	128.516
1	1	3	12	2.26270	0.46382	259.573	1.63655	0.28479	689.376
1	1	3	14	1.17567	0.37990	300.961	1.66050	0.04443	2136.46
1	1	3	26	1.76214	1.01316	17.4161	2.06999	0.00125	41.8583
1	1	2	8	8.00317	6.39809	7.92221	2.29343	0.54118	130.433
1	1	2	10	5.20508	2.63199	36.3184	2.31280	0.11345	103.638
1	1	2	12	2.75827	2.14975	2.29275	1.44925	0.09676	775.886
1	1	2	14	7.34432	7.81950	1.49830	1.30982	0.34496	1942.05
1	1	2	26	7.04420	8.39465	1.53683	1.27915	0.30578	698.241
1	2	3	8	2.46987	0.16229	38.0816	2.30268	0.19948	6.74827
1	2	3	10	1.07583	0.09191	93.1307	2.03979	0.01213	75.4560
1	2	3	12	3.05522	0.20000	117.399	1.24310	0.31346	133.795
1	2	3	14	0.87742	0.40591	244.297	1.72857	0.00320	1613.40
1	2	3	26	3.06842	0.70909	7.45512	1.62625	0.11099	2.38437
1	2	2	8	6.22982	3.81285	10.3564	2.36099	0.46361	53.0041
1	2	2	10	5.48203	5.71635	2.09515	1.59161	0.22151	990.505
1	2	2	12	4.85966	3.06350	17.7673	1.91095	0.33296	170.360
1	2	2	14	4.47886	3.44059	4.75645	1.54036	0.26867	2513.85
1	2	2	26	4.25056	3.69663	4.44279	1.23739	0.14416	1316.18
2	1	3	8	1.39528	0.79078	8.60334	2.36115	0.00449	23.4604
2	1	3	10	3.10802	3.01635	2.16906	1.76477	0.26107	412.691
2	1	3	12	2.27112	1.22715	3.92867	1.61474	0.23738	3161.52
2	1	3	14	2.91829	1.82041	4.30447	1.63236	0.31655	515.052
2	1	3	26	4.38571	2.06779	40.1961	1.67262	0.52717	241.283
2	1	2	8	5.17859	3.90253	6.57772	2.04926	0.37337	90.5016
2	1	2	10	6.38067	2.21109	5.15505	1.85501	0.22469	3.70003
2	1	2	12	4.77043	3.27066	5.75801	1.79855	0.33036	67.3886
2	1	2	14	5.02567	4.25276	2.68183	1.48801	0.29887	2929.20
2	1	2	26	5.51365	3.69510	3.42827	1.14204	0.33097	251.496
2	2	3	8	11.3089	1.84467	12.5961	2.30264	0.36717	3.86907
2	2	3	10	1.96995	0.90463	6.53748	2.18779	0.01715	6.48957
2	2	3	12	17.8777	0.87521	31.8527	1.85903	0.28730	2.11079
2	2	3	14	3.06986	1.91623	5.89269	1.64242	0.20396	349.780
2	2	3	26	3.85811	2.24042	17.5692	1.69940	0.45568	210.325
2	2	2	8	6.55293	4.30193	8.18806	1.83613	0.61672	171.950
2	2	2	10	6.17769	2.81793	61.3200	2.40149	0.04199	143.513
2	2	2	12	5.68887	3.13406	8.66409	2.13086	0.34074	27.7181
2	2	2	14	6.83484	3.55785	2.79045	1.54870	0.22998	2.78037
2	2	2	26	4.63811	3.97469	3.56231	1.36270	0.22151	2122.69

Table B.2. Range correction parameters used in LET charge calibration. For each of the elements oxygen, neon, magnesium and silicon, a single set of parameters was obtained for all LET 2- and 3-parameter events. For iron, a separate parameter set was obtained for 2- and for 3-parameter events, on account of the importance of the charge pickup effect at high charges and low energies. Uncertainties on these values are similar to those on the HET parameter values (Table B.1). As with HET, the interaction between the terms in the function $C(\boldsymbol{x})$ (Eq. 3.2) results in meaningless variation of the individual parameters with Z, and requires that interpolation to other values of Z be carried out on the function values themselves, not on the individual parameters.

2/3 pars.	Z	A_1	A_2	A_3	A_4	A_5	A_6
3	8	4.49349	2.82581	5.49858	1.79321	0.59557	215.390
3	10	3.77272	2.20353	6.73493	1.87348	0.53465	140.629
3	12	3.61972	2.50528	3.09368	1.63469	0.38118	299.741
3	14	2.40585	1.36299	2.60594	1.51003	0.22489	286.408
3	26	2.39328	1.63964	1.67335	1.25813	0.16729	76.5896
2	26	2.39765	1.66821	1.07046	1.09732	0.26932	3433.04

Appendix C

Charge Interval Boundaries

Table C.1. Adopted charge interval boundaries for the more abundant elements. For the rarer elements, a different procedure was used to arrive at the best estimate of the number of particles of a given element.

Z	lower limit	upper limit
6	5.30	6.60
7	6.60	7.45
8	7.45	8.85
10	9.50	10.75
11	10.75	11.45
12	11.45	12.75
13	12.75	13.45
14	13.45	14.75
16	15.40	16.75
18	17.55	18.65
20	19.30	20.70
26	24.60	27.15

Appendix D

LET and HET Incident Energy Ranges

Table D.1. Typical incident energy ranges for elements with $3 \leq Z \leq 30$ in the Voyager LET and HET telescopes.

Z	LET 2-parameter incident energy (MeV/nucleon)	LET 3-parameter incident energy (MeV/nucleon)	HET 2-parameter incident energy (MeV/nucleon)	HET 3-parameter incident energy (MeV/nucleon)
3	2.2 - 3.0	3.2 - 9.2	5.9 - 7.7	7.9 - 28.2
4	2.6 - 3.6	3.8 - 11.1	7.1 - 9.3	9.4 - 33.7
5	2.9 - 4.1	4.4 - 12.9	8.2 - 10.8	11.0 - 39.1
6	3.3 - 4.7	5.0 - 14.9	9.4 - 12.5	12.7 - 45.3
7	3.5 - 5.1	5.4 - 16.2	10.1 - 13.6	13.8 - 49.5
8	3.7 - 5.4	5.7 - 17.5	10.7 - 14.6	14.9 - 53.3
9	3.7 - 5.4	5.8 - 18.0	10.9 - 14.9	15.3 - 55.2
10	3.9 - 5.8	6.2 - 19.5	11.7 - 16.0	16.5 - 60.0
11	3.9 - 5.9	6.2 - 20.1	12.1 - 16.5	16.9 - 62.1
12	4.1 - 6.2	6.6 - 21.4	12.9 - 17.7	17.9 - 66.3
13	4.1 - 6.3	6.7 - 22.0	13.3 - 18.1	18.5 - 68.4
14	4.3 - 6.6	7.0 - 23.3	14.2 - 19.2	19.9 - 72.8
15	4.3 - 6.7	7.0 - 23.7	14.4 - 19.5	20.2 - 74.5
16	4.6 - 7.0	7.4 - 24.9	15.2 - 20.5	21.3 - 78.6
17	4.5 - 7.0	7.3 - 25.1	15.3 - 20.6	21.5 - 79.6
18	4.8 - 7.4	7.7 - 26.3	16.2 - 21.6	22.6 - 83.8
19	4.8 - 7.4	7.7 - 26.7	16.5 - 21.8	23.0 - 85.4
20	5.0 - 7.8	8.0 - 27.9	17.3 - 22.7	24.1 - 89.3
21	4.8 - 7.6	7.7 - 27.4	17.1 - 22.2	23.8 - 88.4
22	4.8 - 7.6	7.8 - 27.7	17.4 - 22.4	24.2 - 89.8
23	4.7 - 7.5	7.8 - 28.0	17.8 - 22.5	24.6 - 91.2
24	4.9 - 7.8	8.1 - 29.0	18.6 - 23.2	25.6 - 94.6
25	4.8 - 7.8	8.1 - 29.3	19.0 - 23.3	26.0 - 95.9
26	5.0 - 8.0	8.4 - 30.3	19.8 - 24.0	27.0 - 99.4
27	4.9 - 7.9	8.3 - 30.4	20.1 - 24.0	27.2 - 100.4
28	5.1 - 8.3	8.7 - 31.7	21.0 - 25.0	28.4 - 104.8
29	4.9 - 8.1	8.5 - 31.3	20.9 - 24.4	28.1 - 104.0
30	5.0 - 8.2	8.6 - 31.9	21.4 - 24.8	28.7 - 106.2

Appendix E
Heavy Charged Particle Enhancements

Table E.1. Complete listing of all heavy charged particle enhancement periods observed by at least one Voyager spacecraft from launch until January 1983. Two time periods (1, 7) actually consist of several closely spaced flare events.

flare period	V1 time period	% of total V1 LET flare data	V2 time period	% of total V2 LET flare data
1	1977: 251.7-275.0	5.06	1977: 252.2-276.0	5.11
2	1977: 285.3-294.8	0.06	1977: 284.1-288.9	0.05
3	1977: 326.3-335.3	2.26	1977: 325.9-334.7	2.49
4	1978: 005.2-022.1	0.23	1978: 005.0-013.7	0.40
5	1978: 044.8-056.5	8.94	1978: 044.7-054.0	8.32
6	1978: 068.0-081.9	0.12	1978: 067.1-073.2	0.12
7	1978: 098.7-135.1	63.42	1978: 107.6-134.0	49.62
8	1978: 177.7-181.6	0.35	1978: 176.0-180.8	0.60
9	1978: 197.1-200.9	0.04	1978: 194.8-198.8	0.19
10	1978: 269.2-287.1	0.51	1978: 268.2-285.7	0.63
11	----------	0.00	1979: 038.2-046.5	0.08
12	1979: 100.1-111.0	0.04	----------	0.00
13	1979: 160.7-171.2	0.30	1979: 160.1-166.1	0.91
14	1979: 192.8-203.5	0.22	----------	0.00
15	1979: 218.1-234.8	0.06	----------	0.00
16	1979: 237.6-256.1	0.46	1979: 234.6-253.3	1.83
17	1979: 261.7-291.1	14.10	1979: 256.1-285.1	21.92
18	1980: 224.0-240.9	0.16	1980: 223.3-233.9	0.14
19	1980: 325.1-349.1	0.35	1980: 321.5-345.0	0.13
20	1981: 125.9-158.1	2.33	1981: 117.0-158.7	3.15
21	1981: 268.2-285.3	0.13	1981: 264.0-279.5	0.32
22	1981: 286.7-313.8	0.26	1981: 285.6-312.9	0.58
23	----------	0.00	1982: 040.3-063.3	0.11
24	1982: 160.5-227.3	0.53	1982: 160.0-229.2	2.80
25	1982: 352.7-1983: 011.4	0.07	1982: 340.2-1983: 017.1	0.48

Appendix F
Event Weighting Factors

Table F.1. Weighting factors used for different subsets of LET/HET data in determining abundant element relative abundances. All values are relative to 3-parameter LET = 1.000 for each spacecraft. The values are the product (geometry factor*livetime) for 3-parameter LET for given data set divided by this product for the indicated data set from the same spacecraft. These values are multiplied by the number of events in the data set before summing all the events in a given time period. No weighting is done between the two spacecraft.

flare	2-parameter LET		2-parameter HET		3-parameter HET	
period	V1	V2	V1	V2	V1	V2
1a	-----	1.000	1.548	1.441	1.454	1.353
1b	-----	1.000	1.542	1.493	1.448	1.403
1c	1.000	1.000	1.500	1.487	1.408	1.397
1d	1.000	1.000	1.069	0.937	1.004	0.880
1e	1.000	1.000	1.359	1.193	1.277	1.120
3	1.000	1.000	1.480	1.428	1.390	1.341
4	1.000	1.000	1.466	1.500	1.377	1.409
5	1.000	1.000	1.409	1.366	1.323	1.283
6	1.000	1.000	1.535	1.541	1.441	1.447
7a	1.000	1.000	1.409	1.345	1.323	1.263
7b	1.000	1.000	1.294	1.170	1.215	1.099
7c	1.000	1.000	1.362	1.280	1.279	1.202
8	1.333	1.000	1.488	1.313	1.398	1.233
9	1.345	1.000	1.680	1.372	1.578	1.289
10	1.333	1.000	1.427	1.508	1.340	1.416
13	1.333	1.000	1.583	1.535	1.487	1.441
16	1.337	1.000	1.640	1.155	1.540	1.085
17	1.342	1.000	1.375	1.002	1.291	0.941
20	1.337	1.000	1.520	1.130	1.428	1.061
22	-----	1.000	-----	1.178	-----	1.106
24	2.020	1.000	1.399	1.145	1.314	1.075
25	1.966	1.000	1.487	1.104	1.397	1.037

Appendix G
Instrumental Anomalies and Other Problems

The analysis of data from the Voyager CRS LET and HET telescopes was complicated by several instrumental problems. These are described in detail elsewhere (Breneman 1984); they are summarized here.

G.1. Pulse Height "Multiplication" Effect

This effect has been observed many times in numerous surface-barrier detectors, both in flight and in the laboratory (Cook 1981, Breneman 1982). Particles passing completely through a detector sometimes yield pulse heights that are anomalously high (by about 10 - 30 %). It occurs most often for particles with high dE/dx in the detector in question, and therefore at a given initial energy, the effect occurs more often for elements higher on the charge scale; in the data it is most prominent for Fe. On a ΔE vs. E' plot, the effect appears as a more or less diffuse "track" above and roughly parallel to the nominal track for the element, since ΔE is anomalously high for the affected particles (Fig. G.1). A charge determination of such an event will of course be high, generally by ~2-3 charge units at Fe. Since the effect is strongly dependent on dE/dx, it is usually evident only in the ΔE-detector immediately before the E'-detector. When Z is calculated for 3-parameter events involving such anomalous pulse heights, Z_2 is more strongly affected than Z_1, since the anomalous pulse height has the role of ΔE for Z_2, while for Z_1 the same detector PHA usually makes only a modest contribution to E' with ΔE normal. On a Z_1 vs. Z_2 plot (e.g., Fig. 3.1), the effect takes the form of a cluster of events to the right of, and slightly above, the main cluster along the diagonal. All of the Voyager LETs show the effect for Fe; although its rate of occurrence varies somewhat between the different telescopes, it is generally in the range of ~5 - 10% of all the 3-parameter Fe SEP events in a given telescope. The fraction of 2-parameter events affected is larger, since the E'-detector is thinner and therefore a larger fraction of the

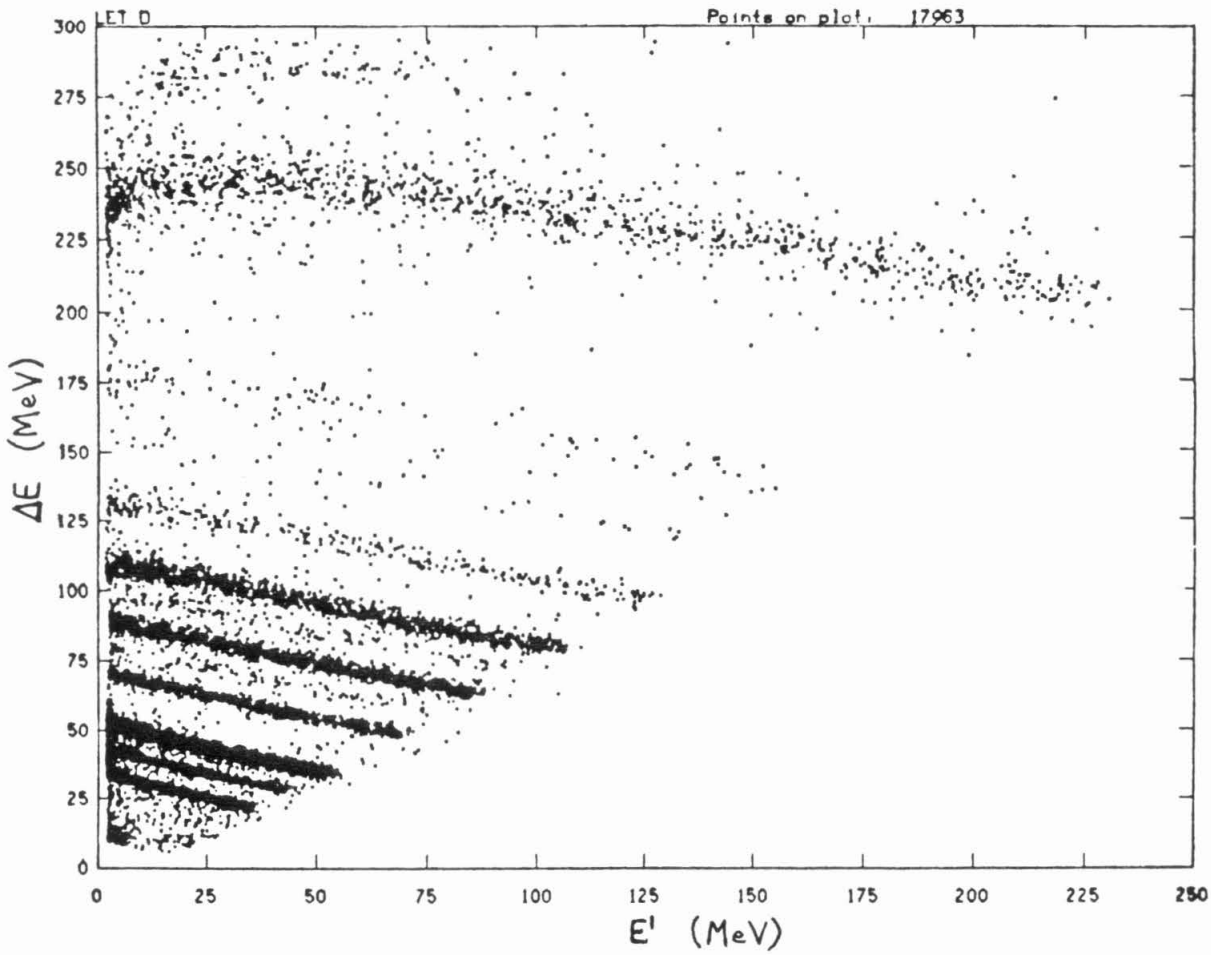

Fig. G.1. ΔE vs. E' plot of Voyager 1 LET D data from flare period 7 exhibiting the pulse height multiplication effect for iron events. Particles with high dE/dx in the ΔE-detector tend to yield pulse heights in that detector which are 10 - 30% too high, resulting in the diffuse band of events above the high-ΔE end of the Fe track.

data has high dE/dx in the ΔE-detector. At least one LET (Voyager 1 LET A) shows evidence for the effect at charges as low as 20.

In the HETs the problem is worse in several respects. Its rate of occurrence at Fe, as a percentage of the total Fe event sample, is generally much larger than in the LETs (~40 % for Voyager 1 HET 2); it is clearly seen for elements as low on the charge scale as Mg in some telescopes (Voyager 1 HET 2 and Voyager 2 HET 2); and for 3-parameter events it can sometimes be seen occurring in either (or both) ΔE-detectors, rather than just the last one, resulting in several displaced clusters of events in those telescopes (Voyager 1 HET 1 and Voyager 2 HET 2).

Two actions were necessary to deal with this problem. For abundant elements affected by the problem, mainly Fe and Ni, the 3-parameter charge consistency requirement was made lenient enough to include the particles affected by pulse height multiplication. The rate of occurrence in LET for elements lower than Fe was negligible compared to other sources of uncertainty in the abundance determination, and no correction was made for these elements. Based on the observed rates in some HET telescopes for the abundant elements (e.g., Fig. G.2 for Voyager 1 HET 2), the rate of occurrence in these telescopes for elements in the Z = 17 - 25 charge range was significant even though limited statistics make it less apparent and less quantifiable. However, HET data were not used for these elements for the reasons given in Section 3.3.

In addition, the energy loss in the ΔE-detector had to be corrected in an approximate way for affected events, so that the total incident energy, which is required for constructing energy spectra, would be accurate.

For 2-parameter events, there is no second independent determination of Z to permit unambiguous separation of normal and abnormal events. This is not a serious problem for abundant elements, since the only abundant element significantly affected is Fe, which has no other elements of comparable abundance near it on the charge scale with which it could be confused. For rare

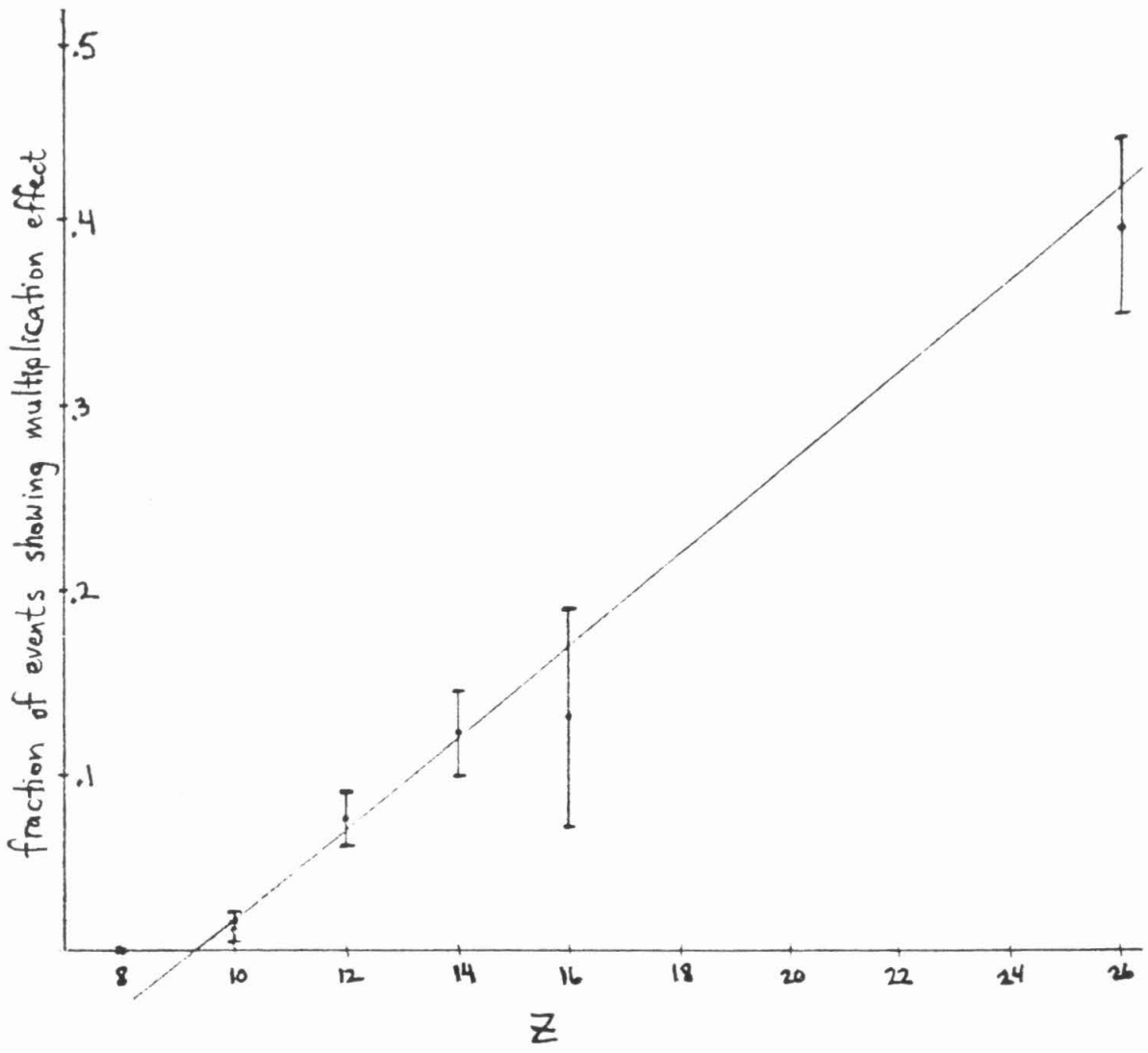

Fig. G.2. Plot of rate of incidence of the pulse height multiplication effect in Voyager 1 HET 2 as a function of Z. The effect is more severe in the HETs than in the LETs.

elements the situation would be more serious, but as noted in Section 3.3, 2-parameter data were not used for rare element abundances due to excessive background contamination from other sources.

G.2. LET Telescope ID Tag Bit Errors at High Counting Rates

For each Block I or Block II LET event, there is a single tag bit which specifies from which LET telescope in that Block the event originated. A near coincidence in the triggering of LETs A and B, as is possible during periods of very high count rates, can result in the bit being set for a LET A event, causing that event to be read out as a LET B event (similarly for C and D). Since the bit is ordinarily set only for LET B events and is otherwise not set, LET A events can be misidentified as LET B events but never the reverse.

The telescope identification bit is used in all subsequent data analysis to determine the appropriate detector thicknesses and gains to use in calculating energy losses in the detectors and, ultimately, the charge of the particle. If the telescope identification is erroneous, incorrect thicknesses and gains are used in the calculations, resulting in incorrect determinations of Z. The magnitude and sign of the discrepancy in Z depends only on the (coincidental) relationship between the thicknesses of the detectors in the paired telescopes, and, to a lesser degree, differences in the energy calibrations of the respective detectors.

On a Z_1 vs. Z_2 plot of 3-parameter Voyager data, this effect has the appearance of small clusters of events displaced slightly from the main clusters along the diagonal for all the more abundant elements. It appears only in plots of the B and D telescopes, since it is events with these identifications which contain some misidentified particles. In the Voyager flight data the effect is noticeable only during flare period 7, for which the peak LET B singles rate is $\sim 5 \times 10^3\ \mathrm{sec}^{-1}$, the highest seen during the Voyager mission through August 1984. Its rate of occurrence is about 3% at this peak rate, an average of about 1% for flare period 7 as a whole, and is the same for all elements for which

statistics permit a measurement. On ΔE vs. E' plots of both 2- and 3-parameter data, these effects have the appearance of "ghost" tracks falling between or partially overlapping the real tracks of nearby elements (Fig. G.3).

Later laboratory work using the backup CRS and pulse generators (Martin 1983) was able to reproduce the effect with greatly improved statistics, and verified the magnitude of the time constant ($\sim 6\mu s$) implied by the flight data while extending coverage to event rates more than an order of magnitude above the highest seen in the flight data.

The impact of this problem on the data analysis is relatively minor. For 3-parameter data, the previously chosen charge-consistency requirement is restrictive enough to easily exclude the misidentified events; the amount of data lost is an insignificant 0.2% of the total, and the remaining data set is as "clean" as that from the other telescopes. The problem is more serious for the 2-parameter data, since there is no second determination of Z to permit separation of the normal and abnormal events; it is an unremovable source of background in the data. For abundant elements this is unimportant, since the error introduced by this background is on the order of 1% or less. But the problem would be serious for rare elements in cases where the "ghost" track of an abundant element overlaps the true location of a rare element, since even 1% of an abundant element could seriously contaminate a much rarer element. However, as noted previously, the 2-parameter LET data are not useful in obtaining rare element abundances on account of other background contributions.

G.3. LET L1 Detector Jupiter Encounter Radiation Damage and Post-Encounter Annealing

As a result of their exposure to intense charged particle fluxes in the inner Jovian magnetosphere during the 1979 Jupiter encounters, the L1 detectors of the LETs experienced radiation damage which can be modeled as a reduction in the "effective thickness" of the detectors. It is thought to be due to the

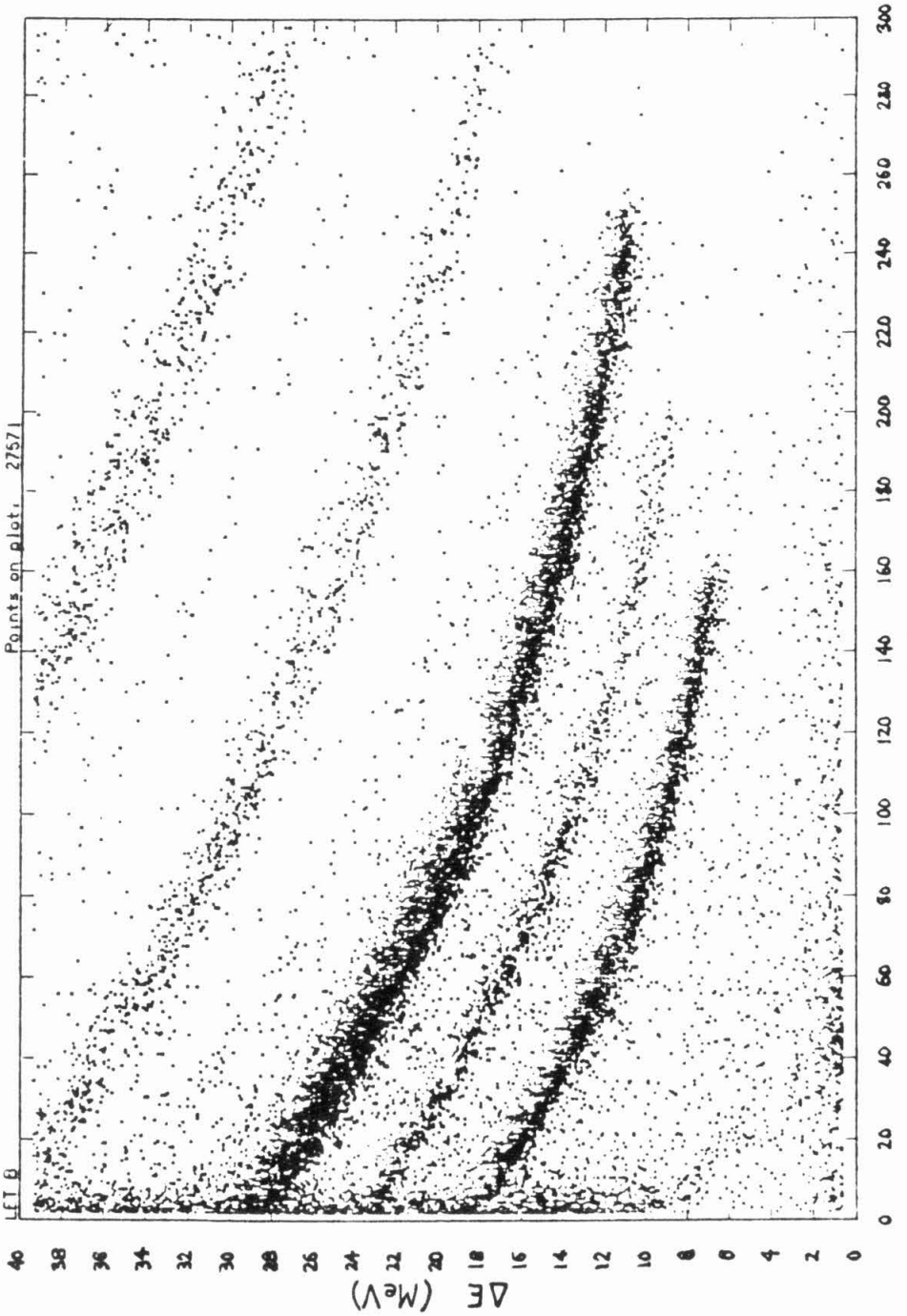

Fig. G.3. ΔE vs. E' plot of three-parameter data from Voyager 1 LET B for flare period 7, showing the "ghost track" in the region of fluorine, caused by LET A oxygen events mistagged as LET B events, and subsequently analyzed as such. The effect occurs at a significant rate only at the highest event rates seen by Voyager to date.

implantation of energetic oxygen and sulfur ions known to be present in the inner Jovian magnetosphere (Gehrels 1982). Although all LETs on both spacecraft were affected to some degree, the Voyager 1 LETs were affected much worse than those on Voyager 2, since the former spacecraft passed closer to Jupiter and experienced a more intense radiation environment. On each spacecraft, LET C was by far the most seriously affected; this telescope was spatially oriented so as to receive the most intense radiation exposure during the Jupiter encounters. (LET B on Voyager 2 experienced unrelated types of radiation damage during the Jovian encounter and has returned no data since the encounter.) The front detectors of the HETs, being much thicker than those of the LETs and protected by a thicker window, showed no detectable effective thickness reduction.

The impact of the radiation damage on the post-Jupiter data is apparent as a shift in the location of the element tracks on a ΔE vs. E' plot of data from flares 16 and 17, the first large post-Jupiter flares, relative to their location in plots of pre-Jupiter flares. Similarly, Z_1 vs. Z_2 plots of flares 16 and 17 show Z-values shifted from their proper values when Z is calculated using the detector thicknesses measured before launch, which served adequately for all pre-Jupiter flares. The change in effective thickness appears to be somewhat dependent on Z, with the magnitude of the reduction increasing with Z for any given detector. Furthermore, with the passage of time the radiation damage seems to gradually undergo a partial reversal. This "annealing" effect is evident in data from the later large flares, 20 and 24, which show less shift in Z than do the flares immediately following Jupiter encounter.

In the analysis of post-Jupiter data, this problem was dealt with by adjusting the L1 detector thicknesses used in the calculation of Z so as to make the calculated charges fall in the proper places on the charge scale. Flares 16 and 17 were used to define the required shift for the more abundant elements; a linear or weakly quadratic function of Z was fit to these to define the Z-dependence for all Z. Data from flare periods 20 and 24 were used in

conjunction with the flare 16/17 data to mathematically characterize the time-dependence of the annealing effect, by fitting to a decaying-exponential function of time. This procedure, repeated for each LET, defined the L1 thickness to be used in analyzing any given post-Jupiter event. The adjustment of the L1 thickness was then incorporated into the iterative cycle for calculating Z. The radiation damage did not have a noticeable effect on the inherent charge resolution of the telescopes, so with the above modifications the post-Jupiter flare data could be treated the same way as the pre-Jupiter data.

Table G.1 lists the adjustment made to the thickness for each L1 detector for carbon and iron at two different times during the post-Jupiter phase. The actual expression for the thickness L(Z,t) of each L1 detector was given by

$$L(Z,t) = L_0 - \Delta L_0(Z) + K \exp(\Delta t / 562.56) \qquad (G.1)$$

where K is a constant, L_0 is the pre-Jupiter thickness, Δt is the time since the Jupiter encounter in days, and $\Delta L_0(Z)$ is the linear or quadratic function of Z that closely fits the required thickness changes for the first post-Jupiter flares.

G.4. Voyager 2 LET C Temporary Gain Shift

During the time period 1978 Apr 3 - June 9, the L1 detector of LET C on Voyager 2 experienced, for unknown reasons, a temporary gain shift (~ 47 % decrease) and an associated excessively high L1 count rate (~ 9×10^3 sec^{-1}). The gain shift and excessive count rate set in abruptly, remained nearly constant until about May 29, and then gradually reverted to their former levels; a very slight decline during the central phase was consistent with the decrease in the intensity of sunlight during the same time period and suggests the possibility of a light leak in the telescope's aluminum window.

The effect on the data was to shift the locations of the element tracks on a ΔE vs. E' plot, and yield shifted charge estimates when nominal gain factors were used in the analysis. The only flares occurring during this time period

Table G.1. Voyager LET L1 detector effective thickness reduction for carbon and iron resulting from Jupiter encounter radiation damage. Flare 17 occurred shortly after the encounter, flare 24 about 2.5 years later. The reduction is smaller for the later flare because of a gradual "annealing" effect following Jupiter encounter. No figures are given for Voyager 2 LET B since this telescope did not function after encounter. Note that the two LET Cs were by far the most severely affected.

S/C LET ID	L1 thickness (μm)	ΔL (Z = 6) (μm)		ΔL (Z = 26) (μm)	
		flare 17	flare 24	flare 17	flare 24
1 A	37.91	-0.89	-0.41	-3.26	-2.78
1 B	30.91	-1.00	-0.58	-2.86	-2.44
1 C	37.07	-5.53	-4.09	-9.75	-8.31
1 D	35.45	-0.62	-0.38	-2.19	-1.95
2 A	34.35	-0.03	+0.08	-0.61	-0.50
2 B	38.55	-----	-----	-----	-----
2 C	35.33	-3.21	-2.10	-6.08	-4.97
2 D	34.76	-0.07	+0.14	-1.12	-0.91

were the three large events of flare period 7. Since the gain was constant at the shifted value during these flares, the data could be analyzed by generating the appropriate gain factors by fitting the oxygen flight data from flare period 7 in the manner described in Appendix A. The resulting values are included in Table A.1.

This anomaly was previously noted (Cook 1981), and the telescope was rejected for analysis because of the problem. However, since the energy calibration used in the analysis is easily adjusted to compensate for the problem, since the charge resolution and background of the telescope do not seem to be affected by the problem and since the three 7 flares include a major fraction of all the SEP data, it was decided to include Voyager 2 LET C in the analysis with the special treatment described above.

G.5. CRS Instrument Configuration Changes

At certain times during the Voyager mission, the configuration of the CRS instruments was changed in ways that influence data analysis. At the beginning of each flight the LETs were configured to require triggering of the L3 detector for pulse height analysis; that is, only 3-parameter events were analyzed. About 12 days after launch the L3 coincidence requirement was removed, permitting both 2- and 3-parameter events to be analyzed. For Voyager 2 this occurred before the first flares were seen, but on Voyager 1 flares 1a and 1b occurred before the configuration was changed, so no 2-parameter events were obtained from these flares. A similar situation occurred on 17 June 1978 when Voyager 1 LET C was switched back to requiring L3 coincidence. Thus for all flares from 8 onward there are no 2-parameter events from this telescope. These situations required changes in the weightings of 2-parameter relative to 3-parameter events for the affected spacecraft and flares. There could still be a residual abundance bias in flares 1a and 1b if the particle composition was energy-dependent and if the two spacecraft saw particles with different spectra, but the possibility of a bias comparable to the statistical uncertainty in the

abundances is very unlikely.

Another important configuration change is the HET gain state. Normally the instrument cycles between high and low gain modes, but after Jupiter encounter HET 1 on Voyager 2 was switched to a high-gain-only mode, so no post-Jupiter SEP heavy ion data were obtained from this telescope. This required changes in the particle weighting factors of HET relative to LET for Voyager 2 for all post-Jupiter flares.

The event weighting factors tabulated in Table 3.8 include the effects of all instrument configuration changes.

G.6. Voyager 1 Block I PHA Problem

On 1982 Feb 8, the Voyager 1 CRS experienced a failure affecting the readout of PHA information from the Block I telescopes (LETs A and B and HET 1). The result of the failure is that in place of PHA2, the instrument reads out whichever of the three PHAs has the largest numerical value. If PHA2 happens to be numerically the largest pulse height, as is true over some energy ranges, the event is read out normally; otherwise some information is lost. The effect of this problem is that some of the 2-parameter events are lost completely, and that some of the 3-parameter events are degraded to 2-parameter events.

The effect of this problem on the data analysis was minimal because it occurred very late in the time span included in the SEP data set, and thus affected only two relatively small flares. The problem was dealt with by simply discarding the data on these flares from the three telescopes affected.

Appendix H
Voyager Spatial Coordinates and Flare Propagation Effects

Table H.1. Differences in peak particle flux between Voyager 1 and 2, and its dependence on Z, for each flare, and the associated differences in spatial location of the two spacecraft at the time of the flare event. Slope and offset are the best-fit values resulting from a least-squares fit to a straight line of the V1/V2 ratios for the different elements. Also shown are the radial (ΔR), longitudinal ($\Delta\varphi$) and latitudinal ($\Delta\vartheta$) separations of the two spacecraft (Voyager 1 minus Voyager 2), and the Voyager 1/Voyager 2 ratio of peak heavy ion count rates seen in two LETs (Table 3.2).

flare #	size	slope pct/chrg unit	V1/V2 offset	date	ΔR (AU)	$\Delta\varphi$ (deg.)	$\Delta\vartheta$ (deg.)	V1/V2 rate ratio
1a	46.0	-0.01 ± 1.23	0.451 ± .058	77.697	-0.007	-4.78	-2.028	1.17
1b	13.6	3.21 ± 2.44	0.497 ± .125	77.704	-0.010	-4.66	-2.169	1.7
1c	34.2	0.63 ± 1.48	1.566 ± .341	77.714	-0.014	-4.49	-2.360	1.8
1d	336.	-1.31 ± 0.48	1.000 ± .057	77.724	-0.017	-4.30	-2.535	2.3
1e	730.	-0.02 ± 0.29	0.926 ± .041	77.736	-0.020	-4.01	-2.737	0.65
3	272.	2.49 ± 0.53	1.031 ± .063	77.898	-0.014	-1.41	-3.669	0.52
4	41.4	-4.84 ± 1.44	0.317 ± .052	78.016	0.017	-0.97	-3.383	0.22
5	1173.	0.13 ± 0.28	0.763 ± .023	78.132	0.052	-1.02	-2.964	0.82
6	7.73	-2.28 ± 5.57	0.575 ± .332	78.190	0.071	-1.12	-2.757	0.83
7a	1237.	-0.12 ± 0.28	0.580 ± .017	78.316	0.114	-1.40	-2.337	1.05
7b	8948.	-0.85 ± 0.12	1.304 ± .017	78.330	0.119	-1.42	-2.286	0.95
7c	6286.	-0.90 ± 0.16	0.834 ± .013	78.336	0.121	-1.44	-2.269	1.3
8	43.8	0.18 ± 2.95	0.723 ± .201	78.490	0.178	-1.85	-1.829	0.48
9	26.9	7.60 ± 2.13	0.607 ± .215	78.538	0.196	-1.98	-1.713	0.62
10	84.6	-3.05 ± 1.28	0.803 ± .104	78.764	0.288	-2.63	-1.189	1.3
13	33.9	2.88 ± 3.09	0.317 ± .093	79.452	0.456	3.55	-0.156	0.48
16	178.	-1.08 ± 1.10	0.322 ± .035	79.656	0.554	6.28	0.097	0.89
17	4286.	-0.89 ± 0.17	0.575 ± .010	79.720	0.599	6.66	0.155	1.09
18	13.4	-2.60 ± 3.48	0.290 ± .104					
19	17.9	-1.68 ± 2.73	1.031 ± .285					
20	657.	-0.32 ± 0.47	1.066 ± .053	81.376	1.548	3.79	6.998	0.53
21	55.6	0.81 ± 1.75	0.535 ± .108					
22	76.2	0.03 ± 1.21	0.495 ± .067	81.826				
24	341.	-1.32 ± 0.94	0.447 ± .041	82.490	3.279	-5.73	16.893	0.76
25				82.992	4.071	-11.42	19.521	0.39

REFERENCES

Anders, E., and Ebihara, M. 1982, "Solar-System Abundances of the Elements," *Geochimica et Cosmochimica Acta* **46,** 2363.

Blackwell, D. E., Booth, A. J., and Petford, A. D. 1984, "Is There an Abundance Anomaly for the 2.2 eV FeI Lines in the Solar Spectrum?," *Astron. Astrophys.* **132,** 236.

Bochsler, P., and Geiss, J. 1976, Grenoble IAU Meeting, Report of Commission 12 (Solar Atmosphere).

Breneman, H. 1982, "Pulse Height 'Multiplication' in Surface Barrier Detectors," Space Radiation Laboratory Internal Report #87, California Institute of Technology.

Breneman, H. 1984, "Anomalies and Other Problems Encountered in Analysis of Voyager LET and HET Data," Space Radiation Laboratory Internal Report #89, California Institute of Technology.

Cameron, A. G. W. 1982, "Elementary and Nuclidic Abundances in the Solar System," in *Essays in Nuclear Astrophysics*, ed. by C. A. Barnes, D. N. Schramm and D. D. Clayton, Cambridge University Press.

Casse, M., and Goret, P. 1978, "Ionization Models of Cosmic Ray Sources," *Ap. J.* **221,** 703.

Cook, W. R., Stone, E. C., Vogt, R. E., Trainor, J. H., and Webber, W. R. 1979, "Elemental Composition of Solar Energetic Particles in 1977 and 1978," *Proc. 16th Int. Cosmic Ray Conf.* (Kyoto), **12,** 265.

Cook, W. R., Stone, E. C., and Vogt, R. E. 1980, "Elemental Composition of Solar Energetic Nuclei," *Ap. J. Lett.* **238,** L97.

Cook, W. R. 1981, "Elemental Composition of Solar Energetic Particles," Ph.D. Thesis, California Institute of Technology.

Cook, W. R., Stone, E. C., and Vogt, R. E. 1984, "Elemental Composition of Solar Energetic Particles," *Ap. J.* **279,** 827.

Cummings, A. C. 1981, private communication.

Garrard, T. L. 1976, "MJS CRS Science Requirements Document," Space Radiation Laboratory Technical Report 76-1, California Institute of Technology.

Gehrels, N. 1982, "Energetic Oxygen and Sulfur Ions in the Jovian Magnetosphere," Ph.D. Thesis, California Institute of Technology.

Gehrels, N., and Cummings, A. C. 1980, "CRS LET Detector Thickness, Area and Geometry Factor Measurements," Space Radiation Laboratory Internal Report #77, California Institute of Technology.

Geiss, J., and Bochsler, P. 1984, "Ion Composition in the Solar Wind in Relation to Solar Abundances," International Conference on Isotopic Ratios in the Solar System, Paris.

Gloeckler, G., Weiss, H., Hovestadt, D., Ipavich, F. M., Klecker, B., Fisk, L. A., Scholer, M., Fan, C. Y., and O'Gallagher, J. J. 1981, "Observations of the Ionization States of Energetic Particles Accelerated in Solar Flares," *Proc. 17th Int. Cosmic Ray Conf.* (Paris), **3,** 136.

Grevesse, N. 1984, "Accurate Atomic Data and Solar Photospheric Spectroscopy," *Physica Scripta* **T8,** 49.

Heckman, H. H., Perkins, B. L., Simon, W. G., Smith, F. M., and Barkas, W. H. 1960, "Ranges and Energy-Loss Processes of Heavy Ions in Emulsion", *Phys. Rev.* **117,** 544.

Hovestadt, D. 1974, "Nuclear Composition of Solar Cosmic Rays", *Proc. Solar Wind III*, ed. by C. T. Russell, University of California, Los Angeles, p. 2.

Israel, M. H., Binns, W. R., Grossman, D. P., Klarmann, J., Margolis, S. H., Stone, E. C., Garrard, T. L., Krombel, K. E., Brewster, N. R., Fickle, R. K., and Waddington, C. J. 1983, "Correlation of Source Abundances of Ultraheavy Cosmic Rays With First Ionization Potential -- Results From HEAO 3," *Proc. 18th Int. Cosmic Ray Conf.* (Bangalore), **2**, 325.

Jacobs, V. L., Davis, J., Kepple, P. C., and Blaha, M. 1977, "The Influence of Autoionization Accompanied by Excitation on Dielectronic Recombination and Ionization Equilibrium," *Ap. J.* **211**, 605.

Jacobs, V. L., Davis, J., Rogerson, J. E., Blaha, M., Cain, J., and Davis, M. 1980, "Dielectronic Recombination Rates, Ionization Equilibrium, and Radiative Emission Rates for Calcium and Nickel Ions in Low-Density High-Temperature Plasmas," *Ap. J.* **239**, 1119.

Janni, J. F. 1966, "Calculations of Energy Loss, Range, Pathlength, Straggling, etc.," Tech. Report AFWL-TR-65-150.

Jordan, C. 1969, "The Ionization Equilibrium of Elements Between Carbon and Nickel," *Mon. Not. R. Astr. Soc.* **142**, 501.

Luhn, A., Klecker, B., Hovestadt, D., Gloeckler, G., Ipavich, F. M., Scholer, M., Fan, C. Y., and Fisk, L. A. 1984, "Ionic Charge States of N, Ne, Mg, Si, and S in Solar Energetic Particle Events," *Adv. Space Res.* **4**, No. 2-3, 161.

Martin, S. 1983, Space Radiation Laboratory Internal Report #91, California Institute of Technology.

Mason, G. M., Gloeckler, G., Hovestadt, D. 1979, "Composition Anomalies in Solar Flares," *Proc. 16th Int. Cosmic Ray Conf.* (Kyoto), **5**, 128.

Mason, G. M., Fisk, L. A., Hovestadt, D., and Gloeckler, G. 1980, "A Survey of ~1 MeV Nucleon^{-1} Solar Flare Particle Abundances, $1 \leq Z \leq 26$, During the 1973-1977 Solar Minimum Period," *Ap. J.* **239**, 1070.

Mason, G. M., Gloeckler, G., and Hovestadt, D. 1983, "Temporal Variations of Nucleonic Abundances in Solar Flare Energetic Particle Events I. Well-

Connected Events," *Ap. J.* **267,** 844.

Mason, G. M., Gloeckler, G., and Hovestadt, D. 1984, "Temporal Variations of Nucleonic Abundances in Solar Flare Energetic Particle Events II. Evidence for Large Scale Shock Acceleration," *Ap. J.* **280,** 902.

McGuire, R. E., von Rosenvinge, T. T., and McDonald, F. B. 1979, "A Survey of Solar Cosmic Ray Composition 1974-1978," *Proc. 16th Int. Cosmic Ray Conf.* (Kyoto), **5,** 61.

Meyer, J.-P., and Reeves, H. 1977, "Realistic Uncertainties on Galactic Abundances and Significance of the Cosmic Ray Source Composition," *Proc. 15th Int. Cosmic Ray Conf.* (Plovdiv), **2,** 137.

Meyer, J. P. 1978, "The Significance of the Carbonaceous Chondrites Abundances," 22nd Liege International Astrophysical Symposium.

Meyer, J.-P. 1979, "Local Galactic Abundances Revisited," *Proc. 16th Int. Cosmic Ray Conf.* (Kyoto), **2,** 115.

Meyer, J.-P. 1981, "A Tentative Ordering of All Available Solar Energetic Particles Abundance Observations I. The Mass Unbiased Baseline," *Proc. 17th Int. Cosmic Ray Conf.* (Paris), **3,** 145.

Meyer, J.-P. 1985, "The Baseline Composition of Solar Energetic Particles," *Ap. J. Suppl.* **57,** 151.

Northcliffe, L. C., and Schilling, R. F. 1970, "Range and Stopping Power Tables For Heavy Ions," Nucl. Data Tables A7, 233.

Povlis, J. 1980, "Voyager I and II Electronic Calibration," Space Radiation Laboratory Technical Report 80-2, California Institute of Technology.

Ross, J. E., and Aller, L. H. 1976, "The Chemical Composition of the Sun," *Science* **191,** 1223.

Shull, J. M., and van Steenberg, M. 1982, "The Ionization Equilibrium of Astrophysically Abundant Elements," *Ap. J. Suppl.* **48,** 95.

Stilwell, D. E., Davis, W. D., Joyce, R. M., McDonald, F. B., Trainor, J. H., Althouse, W. E., Cummings, A. C., Garrard, T. L., Stone, E. C., and Vogt, R. E. 1979, "The Voyager Cosmic Ray Experiment," *IEEE Trans. Nucl. Sci.* **NS-26(1),** 513.

Stone, E. C., Vogt, R. E., McDonald, F. B., Teegarden, B. J., Trainor, J. H., Jokipii, J. R., and Webber, W. R. 1977, "Cosmic Ray Investigation for the Voyager Missions: Energetic Particle Studies in the Outer Heliosphere -- and Beyond," *Sp. Sci. Rev.* **21,** 355.

Veck, N. J., and Parkinson, J. H. 1981, "Solar Abundances From X-Ray Flare Observations," *Mon. Not. R. Astr. Soc.* **197,** 41.

Vernazza, J. E., Avrett, E. H., and Loeser, R. 1981, "Structure of the Solar Chromosphere III. Models of the EUV Brightness Components of the Quiet Sun", *Ap. J. Suppl.* **45,** 635.

Vidor, S. B. 1975, "Observations of Nitrogen and Oxygen Isotopes in the Low Energy Cosmic Rays," Ph.D. Thesis, California Institute of Technology.

von Rosenvinge, T. T., and Reames, D. V. 1979, "ISEE-3 Measurements of Solar Energetic Particle Composition," *Proc. 16th Int. Cosmic Ray Conf.* (Kyoto), **5,** 68.

Webber, W. R. 1975, *Proc. 14th Int. Cosmic Ray Conf.* (Munich), **5,** 1597.

Ziegler, J. F. 1977, "Helium Stopping Powers and Ranges in all Elements," Pergamon Press.